

UCSF

UC San Francisco Electronic Theses and Dissertations

Title

Evaluating Translation as an Antimalarial Target

Permalink

<https://escholarship.org/uc/item/4w1197c1>

Author

Garcia, Valentina Elizabeth

Publication Date

2021

Peer reviewed|Thesis/dissertation

Evaluating Translation as an Antimalarial Target

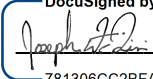
by
Valentina Elizabeth Garcia

DISSERTATION
Submitted in partial satisfaction of the requirements for degree of
DOCTOR OF PHILOSOPHY

in
Biochemistry and Molecular Biology

in the
GRADUATE DIVISION
of the
UNIVERSITY OF CALIFORNIA, SAN FRANCISCO


Approved:

DocuSigned by:

781306CC2BFA4A5... Joseph DeRisi
Chair

DocuSigned by:

Peter Walter

DocuSigned by:
ADAM FROST
ADAM FROST

DocuSigned by:

9BCB4DFEE8384D2... Anita Sil

Committee Members

**Copyright 2021
by
Valentina Garcia**

*To Pablo Garcia and Deborah Zimmerman, for guiding me as both great scientists and
absolutely incredible parents*

Acknowledgements

I would first like to acknowledge Dr. Joe DeRisi for being my PI and advisor throughout my PhD. Thank you for always being a supply of never-ending big picture ideas while still being willing to troubleshoot the smallest of issues. I knew joining the lab would be an adventure from day 1, and it truly has never been boring. No matter how big the distractions, you have always had a thought to share and advice to give, I will always be grateful for the time you have spent working with me towards this Ph.D.

This work would also not be the same without the help of my thesis committee, Dr. Peter Walter, Dr. Anita Sil, and Dr. Adam Frost. You three helped keep me on track and focused while also guiding my research through many twists and turns. Thank you so much for your support of not only my work, but also for me as a scientist and person.

Next, thank you to the others closest to the science presented here, my various co-authors. To Jamin Liu, Dr. Christine Sheriden, Dr. Vida Ahyong, Dr. John Lee, Hector Chaires, Dr. Qi, Li, Dr. Ian Seiple, Dr. James Fraser, Rebekah Dial, Dr. Mark Stenglein, Dr. David Sanchez-Migallon Guzman, Marylee L. Layton, Dr. Laura L. Hoon-Hanks, Dr. Scott M. Boback, Dr. Kevin Keel, Tracy Drazenovich, Dr. Michelle G. Hawkins, and Dr. Joseph DeRisi, this compilation of my work would not look remotely the same without each of you and your hard work. Thank you for being my teachers, my peers, and my support.

I would also like to acknowledge the various members of Team Malaria during my time in the DeRisi lab. To the technicians, Jenai Quan, Hannah Richardson, Rebekah, and now, Matthias Hapte-Selassie, thank you for making sure there was always a large supply of blood and for being willing to adapt what you were doing to what was needed. To two former grad students, Vida and Christine, thank you for your patience in working with and teaching a new

and naïve grad student. I also deeply appreciate the post-docs, Dr. Emily Crawford, Dr. Wesley Wu, and Dr. Madhura Raghavan, for your encouragement and guidance along the way.

Additionally, to Manny De Vera, Jenn Mann, and Brittany Worth, thank you for always making sure the team had what we needed and for being so approachable about any issues or problems in the lab. To the various anonymous blood donors who never complained about needing to eat a burger to make the parasites happy, I consider each of you an extension of the team as this work would be impossible without you.

Many thanks to my bay mates Jamin, Wesley, and Dr. Kristeene Knopp for always laughing with me when something went wrong and cheering when something went right. I have also been incredibly lucky to work alongside so many other graduate students in the DeRisi lab, and each of you has taught me something over the years. To those of you in the lab when COVID struck, Matt Laurie, Jamin, Sara Sunshine, Dr. Hanna Retallack, Sara Vazquez, and Andrew Kung, I could not think of a better group of people to go through the craziest of situations with. Thank you for the desperately needed boba and ice cream trips that always came with a side of support.

To my wonderful classmates, Aditya Anand, Allison Cohen, Athena Lin, Benjamin Barsi-Rhyne, Efren Reyes, Joseph Choe, Justin Salat, Karen Cheng, Karen Ruiz, Karina Perlaza, Kelsey Haas, Kyle Fowler, Nairi Hartooni, Nnejiuwa Ibe, Nick Sanchez, Rachel Greenstein, Sumitra Tatapudy and Xiaowei Yan, you were a wonderful group of people to start this adventure with. Thank you to Allison and Efren for making 1260 the best place to live for over 6 years, to Ben for giving out advice on everything from life to science, and to the Brain Trust, Nairi and Kelsey, for always having my back while doling out words of wisdom.

I feel so fortunate to have an incredible community outside of science as well that helped keep me grounded through the end. To my friends from high school and college, thank you for making me laugh about how silly things can be sometimes. To the Walter family, thank you for cheering me on for all these years and providing a reprieve when it was most needed.

Finally, I want to acknowledge three people who are impossible to thank in writing succinctly or sufficiently. They each contributed in innumerable ways to this thesis, sometimes directly and many times by just encouraging me to finish the marathon. To Austin Walter, Dr. Deborah Zimmerman, and Dr. Pablo Garcia, simply put: thank you for everything.

Contributions

Chapter 2

Includes content previously published in:

Valentina E. Garcia, Jamin Liu, Joseph L. DeRisi. Low-cost touchscreen driven programmable dual syringe pump for life science applications. *HardwareX* Volume 4, (2018):

<https://doi.org/10.1016/j.ohx.2018.e00027>.

Chapter 3

Includes content previously published in:

Sheridan, C.M., Garcia, V.E., Ahyong, V. DeRisi J.L. The *Plasmodium falciparum* cytoplasmic translation apparatus: a promising therapeutic target not yet exploited by clinically approved anti-malarials. *Malar J* 17, 465 (2018): <https://doi.org/10.1186/s12936-018-2616-7>

Chapter 4

Includes contributions by John Lee, Hector Chaires, Qi Li, Ian Seiple, James Fraser and Joseph L. DeRisi

Chapter 5

Includes content currently in preparation that is publicly available in:

Valentina E. Garcia, Rebekah Dial, and Joseph L. DeRisi. Functional characterization of 5' UTR cis-acting sequence elements that modulate translational efficiency in *P. falciparum* and humans. *BioRxiv* (2021): doi: <https://doi.org/10.1101/2021.09.07.459299>

Chapter 6

Includes content previously published in:

Mark D. Stenglein, David Sanchez-Migallon Guzman, Valentina E. Garcia, Marylee L. Layton, Laura L. Hoon-Hanks, Scott M. Boback, M. Kevin Keel, Tracy Drazenovich, Michelle G. Hawkins, and Joseph L. DeRisi. Differential Disease Susceptibilities in Experimentally Reptarenavirus-Infected Boa Constrictors and Ball Pythons. *Journal of Virology*, 91, 15 (2017): <https://doi.org/10.1128/JVI.00451-17>.

Studying translation in the malaria causing eukaryotic parasite *Plasmodium falciparum*

Valentina Elizabeth Garcia

Abstract

As the primary cause of severe malaria, *P. falciparum* is a vexing parasite that has had profound effects on humanity for centuries. To continue to fight towards the global eradication of malaria, novel treatments must be employed. These therapeutics can be developed through two different means. Already existing compounds can be screened for specific activity against the parasite, or drugs can be designed to target unique parasite biology. Both are powerful potential methodologies; however, both also require a deeper understanding of parasite biology. Here, we take both approaches to explore translation as a potential therapeutic pathway. We start in chapter 2 with tool development that aided our ability to scale up our studies. In chapter 3, all commercially available antimalarials were screened for an effect on translation. In chapter 4, synthetic derivatives of Virginiamycin M2 were screened for activity against *P. falciparum* growth and *in vitro* translation. In chapter 5, we reversed our approach by studying the mechanisms of translation initiation in *P. falciparum* and compared the results to human. Finally in bonus chapter 6, we take a sharp turn to zoonotic disease and look at the differential effects of reptarenavirus infection on boa constrictors and ball pythons.

Table of Contents

Chapter 1: An Introduction.....	1
Chapter 1 references.....	9
Chapter 2: Tool Development to Produce <i>In Vitro</i> Translation Lysates.....	13
2.1 Abstract.....	14
2.2 Hardware in context.....	14
2.3 hardware description.....	16
2.4 Design file.....	17
2.5 Build instructions.....	18
2.6 Operation instructions.....	23
2.7 Validation.....	25
Chapter 2 References.....	40
Chapter 3: Identification of Translation Inhibitors by <i>in vitro</i> Translation.....	41
3.1 Abstract.....	42
3.2 Background.....	43
3.3 Methods.....	45
3.4 Results.....	51
3.5 Discussion.....	57
3.6 Conclusions.....	59
Chapter 3 References.....	70
Chapter 4: Streptogramin A antibiotic derivatives inhibit translation through binding to <i>Plasmodium falciparum</i> and mammalian 80S ribosomes	76
4.1 Abstract.....	77

4.2 Introduction.....	77
4.3 Results.....	79
4.4 Conclusions.....	80
4.4 Materials and Methods...	81
Chapter 4 References.....	91
Chapter 5: Comparing the role of cis-acting regulatory sequences in mediating translational efficiency for <i>Plasmodium falciparum</i> and humans.....	93
3.1 Abstract.....	94
3.2 Background.....	95
3.3 Methods.....	97
3.4 Results.....	103
3.5 Discussion.....	112
3.6 Conclusions.....	116
Chapter 5 References.....	132
Chapter 6: BONUS Inclusion body disease infection and pathology in boid snakes.....	138
6.0 Prelude.....	139
6.1 Abstract.....	139
6.2 Importance.....	140
6.3 Introduction.....	140
6.4 Results.....	142
6.5 Discussion.....	147
6.6 Materials and Methods.	150
Chapter 6 References.....	166

List of Figures

Chapter 2

2.1 The assembled PDSP.....	28
2.2 Models of all 3D printed PDSP components.....	29
2.3 Electrical wiring schematic of the PDSP.....	30
2.4 Images of key PDSP assembly steps as described in 2.5.4 Hardware Assembly.....	31
2.5 The PDSP's GUI Interface.....	32
2.6 Characterization of the PDSP for lysate generation.....	33

Chapter 3

3.1 Optimization and quality control parameters of PfIVT extracts.....	61
3.2 Dose-dependent inhibition of S35 incorporation and PfIVT assays by eukaryotic translation inhibitors.....	62
3.3 Dose-dependent inhibition of S35 incorporation and PfIVT assays by negative control compounds.....	63
3.4 Dose-dependent inhibition of S35 incorporation and PfIVT assays by antimalarial compounds.....	64
3.5 Dose-response curves of <i>P. falciparum</i> growth, PfIVT, and RRIVT for mefloquine and controls.....	65

Chapter 4

4.1: 72-hour growth and in vitro translation inhibition curves with Virginiamycin M2, Flopristin, F224, and F1037.....	88
4.2: EC50 comparison between <i>P. falciparum</i> and human cell lines.....	89
4.3: F1037 bound to the PTC in <i>P. falciparum</i> and rabbit ribosomes.....	90

4.4: F1037 bound to the PTC in <i>P. falciparum</i> and <i>e. coli</i>	90
--	----

Chapter 5

5.1 Comparison of features within the 5' UTRs of genes in the bottom 10% (n=209) and top 10% (n=209) of TEs.....	118
5.2 Further comparison of 5' UTR features of genes in the bottom 10% and top 10% of TEs in the late trophozoite stage.....	119
5.3 130 nucleotides of the 5' UTR from a translationally active (PF3D7_1428300) and repressed gene (PF3D7_1411400) were sufficient to drive distinct TE.....	120
5.4 Comparison of uncapped and capped RNAs in both <i>in vitro</i> assays.....	121
5.5 Dissecting the effects of the four uAUGs in R[WT].....	122
5.6 uAUGs from R[WT] exchanged into A[WT] at the same positions.....	123
5.7 Predicted repressive effect of combinations of the uAUGs in R[WT].....	124
5.8 Effect of equally spaced and out of frame, non-terminated uAUGs or uORFs on TE.....	125
5.9 Effect of point mutations in R[Δ 1: Δ 2: Δ 4]*.....	125
5.10 Effect of equally spaced and in-frame, non-terminated uAUGs or uORFs on TE.....	126
5.11 Differential prevalence of non-terminated uAUGs and uORFs.....	127
5.12 Evaluating the effect of GC content on translation.....	128
5.13 Predicted secondary structure when changing CG content.....	129
5.14 Evaluating the effects of the ends of the 5' UTRs on translation.....	130

Chapter 6

6.1 Timeline of experimental reptarenavirus infection of boa constrictors and ball pythons.....	157
6.2 Viral RNA load in reptarenavirus infected boa constrictor tissues by qRT-PCR.....	158
6.3 Viral load by qRT-PCR in the feces, urates, and shed skin of infected boa constrictors.....	159
6.4 Viral RNA load in ball python tissues by qRT-PCR.....	159
6.5 Viral inclusions in boa constrictor tissues identified with anti-NP antibody.....	160
6.6 Viral nucleoprotein in ball python brain tissue identified with anti-NP antibody....	161
6.7 Absence of viral nucleoprotein in non-brain ball python tissues.....	162
6.8 Protein inclusions in boa constrictors visualized with H&E staining.....	163
6.9 Inflammation identified in ball python central nervous system by H&E staining...	164
6.10 Small eosinophilic cytoplasmic inclusions in ball python bile duct.....	165

List of Tables

Chapter 2

Table 2.1 Design files for all 3D printed parts of the PDSP for lysate generation.....	34
Table 2.2 List of all purchased items with number required for the PDSP.....	35
Table 2.3 Minimum and maximum theoretical flow rates for the PDSP.....	39

Chapter 3

Table 3.1 Mechanism of action and species specificity of translation inhibitors.....	69
Table 3.2 Mechanism of action of non-translation inhibitors.....	69
Table 3.3 Half-maximal effective concentrations (nM) determined in <i>P. falciparum</i> growth inhibition assay.....	70

Chapter 4

Table 4.1: EC50s for each compound in the various cell types.....	90
---	----

List of Abbreviations

CNS—Central nervous system

GoGV—Golden Gate virus

IBD—Inclusion body disease

PDSP—Programable dual syringe pump

PfIVT— *Plasmodium falciparum in vitro* translation

RRIVT—Rabbit reticulocyte *in vitro* translation

uAUG—Upstream start site

uORF—Upstream open reading frame

VM2—Virginiamycin M2

Chapter 1: An Introduction

Plasmodium falciparum

Malaria is an ancient disease that has taken many lives throughout history and persists today. During the 19th century, malaria infections led to approximately 2-5% of all deaths [1]. Fortunately, through global efforts, the international disease burden of malaria has greatly decreased. In just the last two decades, incidences dropped from 262 million cases per year in 2002 [2] to 229 million in 2019 [3]. Even more impressively, mortalities have more than halved from 839,000 per year [2] to 409,000 [3]. However, as global eradication is the final goal, more research needs to be done into combating the parasites that make this disease so persevering.

Human malarial infections can be caused by five distinct species of *Plasmodium* (*P. falciparum*, *P. vivax*, *P. malariae*, *P. ovale*, and *P. knowlesi*) [4]. They all share a similar life cycle and are transmitted to humans via related species of anopheline mosquitos. Of these five species, however, *P. falciparum* is by far the most prevalent, causing 96% of cases in the WHO African Region where the highest disease burden remains [5]. Additionally, *P. falciparum* is associated with the most severe disease outcomes and the highest mortality rate, making it the primary focus of most therapeutic research.

Many successful therapies have been developed against *P. falciparum*. However, the parasite has a remarkable ability to develop chemoresistance. With every introduction of a new antimalarial, drug resistance is sure to follow [6]. Combination therapies, where two antimalarials are given together to circumvent resistance, do increase therapeutic efficacy and lengthen the resistance timeline, however, double resistant parasites can, and do, eventually evolve [7]. Surveying for molecular markers of resistance can aid with the delivery of effective

antimalarials to patients [8], but the global fight against malaria still desperately needs novel therapeutics. To identify and develop drugs with unique mechanisms of action, the biology of *P. falciparum* must be understood.

P. falciparum, like all *Plasmodium* species, is an obligate intracellular parasite. Its complex life cycle is often conceptually broken into three distinct stages: the mosquito stage, the liver stage, and the erythrocyte stage. Human infection begins with the bite of a female *Anopheles* mosquito introducing sporozoites into the dermis [9]. Sporozoites migrate to the blood stream where they circulate until adhering to liver endothelial cells and infecting hepatocytes [10]. After a certain checkpoint, hepatocytes start producing merozoites that are released into the blood stream, commencing the erythrocytic asexual life cycle.

The erythrocytic life cycle is further broken into four morphological stages: merozoites, rings, trophozoites, and schizonts. Merozoites invade red blood cells by interacting with receptors on the plasma membrane of erythrocytes. By the end of active invasion, the merozoite is surrounded by a parasitophorous vacuole that is fully encapsulated within the red blood cell [11]. After invasion, the asexual erythrocytic life cycle is ~48 hours and commences with the ring stage. Rings start with only one genomic copy then the parasite begins undergoing multiple rounds of mitosis as it progresses through the trophozoite stage to the schizont stage with approximately 22 genomic copies. At the end of the schizogony, each copy is individually encapsulated within a nuclear envelope and is ready to be released as a merozoite upon rupture of the infected erythrocyte [12].

Many of the essential molecular mechanisms that regulate this complex life cycle remain understudied. This is in part due to the difficulty of working with an obligate pathogen in laboratory settings. Fortunately, the asexual erythrocytic stages of *P. falciparum* can be

maintained in culture using donor human blood and a 5% oxygen environment. Despite the ability to study the symptomatic stage, about 33% of *P. falciparum* genes have unknown functions, including many that are expressed during the erythrocytic stages. Additionally, many of the identified proteins are ascribed functions based on their homology to proteins characterized in other eukaryotes and have yet to be verified independently in *P. falciparum* [13].

Eukaryotic translation

Translation is a fundamental biological pathway required by every form of life. It consists of three distinct processes: initiation, elongation, and termination. Translation initiation determines the mRNA's translation efficiency (TE) by regulating the identification of the translation initiation sites (typically an "AUG" [14-15] and ends with the ribosome fully assembled at the protein coding start site. Elongation then proceeds with the protein synthesis of the encoded protein [16]. Finally, termination is the process of releasing the nascent peptide chain and recycling the translational machinery [17].

Translation elongation is highly conserved, not just across eukaryotes, but across all living organisms. The catalytic activity required for elongation is performed by the ribosome, a large ribonucleoprotein complex. In eukaryotes, an assembled ribosome consists of four ribosomal RNAs (rRNA) and at least 80 different proteins [18]. The rRNAs form two distinct subunits, the 60s and the 40s, that unite to form the 80s ribosome for translation elongation. The 80s contains the three conserved functional sites that make up the catalytic core of the ribosome: the aminoacyl (A), peptidyl (P), and exit (E) sites. Elongation begins once the 80s ribosome is assembled at the protein coding start site with the initiator tRNA bound to methionine positioned within the A-site. Eukaryotic elongation factor 1 (eEF1) then brings the requisite amino acid

bound tRNA. When the new tRNA is accommodated in the A-site of the ribosome, the initial tRNA is moved to the P-site. A peptidyl-transferase reaction occurs, binding the amino acid from the initial tRNA to the amino acid of the tRNA in the A-site. A relocation step promoted by eukaryotic elongation factor 2 (eEF2) then positions the initial tRNA into the E-site while the tRNA bound to the nascent polypeptide chain moves into the P-site. This leaves the A-site vacant for the next tRNA to be brought in by eEF1 allowing elongation to continue [19-20].

Elongation continues until a stop codon (“UAA”, “UAG”, or “UGA”) enters the A-site of the ribosome, thereby activating translation termination and ribosome recycling [21]. Stop codons in the A-site are recognized by eukaryotic recycling factor 1 (eRF1), which complexes with eukaryotic recycling factor 3 (eRF3) to release the nascent polypeptide chain. ATP-binding cassette sub-family E member 1 (ABCE-1) then helps to split the ribosome back into its 40s and 60s subunits [17]. The 40s can then be incorporated into a new translation initiation complex.

While there are many ways eukaryotes can initiate translation, many are often employed under stress conditions. Canonical eukaryotic cap-mediated translation initiation begins with the ternary complex, containing the initiating Met-tRNA, eIF2, and GTP, assembling with the 40s ribosomal subunit, eIF1, eIF1a, eIF3, and eIF5 to form the 43S pre-initiation complex. The assembled complex is recruited to the 5' cap of mRNAs through interactions with the cap binding complex eIF4F to form the 48S initiation complex. The 48S scans the 5' untranslated region (5' UTR) searching for the translation initiation site that marks the start of the protein coding region, typically an “AUG” [22]. Upon recognition of the start site, many initiation factors disassociate, allowing the 60s to join the 40s to form the 80s ribosome. Using human models, recent advances in cryo-electron microscopy and 40S ribosomal footprinting both support a tethered model of initiation where the 48S does not release the cap-binding complex

until the formation of the 80S ribosome, leading to only one scanning complex on each mRNA at a given time [23-24].

The rate of translation initiation can be regulated by both *trans*- and *cis*- acting factors. *Trans*-acting factors are protein factors that bind to the mRNA to regulate translation [25]. For example, iron regulatory proteins bind to the 5' end of ferritin mRNAs to block translation initiation thereby inhibiting protein synthesis [26]. *Cis*-acting elements are sequence elements within the mRNA that regulate translational efficiency.

Famously, the region proximal to the translation start site acts as a *cis*-acting element by interacting with the scanning complex to recognize the start site and facilitating base pairing between the initiator tRNA and the start codon [27]. The surrounding sequence that increases the rate of "AUG" recognition is commonly referred to as the Kozak Sequence. In vertebrates, the Kozak sequence is "CRCCAUG" where R stands for a purine, but this may differ between eukaryotes [28-29]. Another common *cis*-acting regulatory element is the presence of upstream 'AUG's (uAUGs) that precede the protein coding start site. uAUGs can be followed by an in-frame stop site also preceding the protein coding region, which together form an upstream open reading frames (uORFs). In mammalian cells and *Saccharomyces cerevisiae*, uAUGs and uORFs commonly repress translation of the downstream protein through various different mechanisms, including by sequestering ribosomes within the 5' UTR or initiating translation out of frame from the protein coding region [25-27].

Translation in P. falciparum

While many aspects of translation are conserved between eukaryotes, including the three general processes of initiation, elongation, and termination, several *P. falciparum* specific

translation inhibitors have been identified. Many of these inhibitors that affect cytoplasmic translation target tRNA synthetases, including isoleucyl-tRNA synthetase and Lysyl-tRNA synthetase [33-34]. However, M75717, currently in clinical trials as an antimalarial, is a potent inhibitor of *P. falciparum* eEF2 [35]. MMV008270 has also been demonstrated to specifically inhibit *P. falciparum* cytoplasmic translation, but the mechanism by which it do so remains unknown [36]. Together these compounds demonstrate that there are unique facets to *P. falciparum* cytoplasmic translation.

Several unique features of translation are evident within the *P. falciparum* genome. For example, *P. falciparum* contains two genes encoding distinct copies of a small ribosomal RNA. Each copy has its own stage specific expression with gene A being expressed in the asexual life stages [37-38]. Additionally, while other eukaryotes have upwards of 70 repeat copies for their ribosomal genes, *P. falciparum* only maintains 4 to 8 copies. Additionally, the *P. falciparum* genome is uniquely “AT” rich, necessitating adaptations of the translational machinery to avoid frameshifting or stalling on long poly-A stretches within the mRNAs [39].

The transcriptome of *P. falciparum* introduces more unusual aspects of *P. falciparum* with implications for translation. mRNA sequencing coverage predicts that the 5' UTRs of *P. falciparum* vary in size, but that the median length across the stages ranges between 607 nucleotides to 815 nucleotides [40-41]. These long 5' UTRs contain numerous uAUGs and uORFs. For 3569 genes expressed during erythrocytic infection there are 36,086 predicted uORFs with at least two amino acids coded for between the start and stop site. Despite the high prevalence of putative *cis*-acting features, ribosome profiling indicates that transcription and translation are highly correlated, with less than 10% of the genome being under translational

control [41]. These facets of *P. falciparum* biology suggest that translation in the parasite may be more distinct from other eukaryotes than would be expected.

Work presented here

Here, I, along with my numerous colleagues and collaborators, dive into the translational mechanisms of *P. falciparum*. As a non-model eukaryote, *P. falciparum* provides a plethora of obstacles to studying translation. Additionally, as finding specific therapeutics or unique parasite biology is a major motivation, it can be advantageous to directly compare the biology of the parasite with that of its human host. Many of the methodologies used to study human biology must be dramatically altered to adapt them for studying malaria, hindering the kinds of comparisons that can be made. Fortunately, mature erythrocytes have purged their translational machinery, making it possible to isolate the translational machinery of the parasite. For these reasons, throughout this thesis *in vitro* translation is deployed to both evaluate potential therapeutics and to gain a mechanistic understanding of translation in malaria.

We start in chapter two with tool development to standardize the production of *in vitro* translation lysates by building a programmable dual-syringe pump. In chapter 3, we use these *in vitro* translation lysates to directly show that no commercially available antimalarial targets cytoplasmic translation, despite some having indirect effects on protein synthesis. In chapter 4, synthetic derivatives of Virginiamycin M2, a streptogramin A antibiotic, are screened for activity against *P. falciparum* and human cell lines. We find that these compounds inhibit translation in both *P. falciparum* and mammalian *in vitro* translation lysates, likely through binding to the peptidyl-transferase center. We end our *P. falciparum* journey in chapter 5, where we reverse our approach by using *in vitro* translation lysates to compare the mechanisms of translation initiation

in *P. falciparum* and humans to show the effects of *cis*-acting features is conserved between the two distant eukaryotes.

Chapter 1 References

1. Drugs, I. of M. (US) C. on the E. of A., Arrow, K. J., Panosian, C. & Gelband, H. A Brief History of Malaria. Saving Lives, Buying Time: Economics of Malaria Drugs in an Age of Resistance (*National Academies Press* (US), 2004).
2. Cibulskis, R. E. et al. Malaria: Global progress 2000 – 2015 and future challenges. *Infect Dis Poverty* **5**, 61 (2016).
3. World Malaria Report 2020. <https://www.who.int/teams/global-malaria-programme/reports/world-malaria-report-2020>.
4. Sato, S. Plasmodium—a brief introduction to the parasites causing human malaria and their basic biology. *Journal of Physiological Anthropology* **40**, 1 (2021).
5. World malaria report 2020. <https://www.who.int/publications-detail-redirect/9789240015791>.
6. Hyde, J. E. Drug-resistant malaria. *Trends in Parasitology* **21**, 494–498 (2005).
7. Ehrlich, H. Y., Bei, A. K., Weinberger, D. M., Warren, J. L. & Parikh, S. Mapping partner drug resistance to guide antimalarial combination therapy policies in sub-Saharan Africa. *PNAS* **118**, (2021).
8. Lin, J. T., Juliano, J. J. & Wongsrichanalai, C. Drug-Resistant Malaria: The Era of ACT. *Curr Infect. Dis. Rep.* **12**, 165–173 (2010).
9. Maier, A. G., Matuschewski, K., Zhang, M. & Rug, M. *Plasmodium falciparum*. *Trends in Parasitology* **35**, 481–482 (2019).
10. Douglas, R. G., Amino, R., Sinnis, P. & Frischknecht, F. Active migration and passive transport of malaria parasites. *Trends Parasitol* **31**, 357–362 (2015).
11. Cowman, A. F., Healer, J., Marapana, D. & Marsh, K. Malaria: Biology and Disease. *Cell* **167**, 610–624 (2016).

12. Gerald, N., Mahajan, B. & Kumar, S. Mitosis in the Human Malaria Parasite *Plasmodium falciparum*. *Eukaryotic Cell* **10**, 474–482 (2011).
13. Böhme, U., Otto, T. D., Sanders, M., Newbold, C. I. & Berriman, M. Progression of the canonical reference malaria parasite genome from 2002–2019. *Wellcome Open Res* **4**, 58 (2019).
14. Sonenberg, N. & Hinnebusch, A. G. Regulation of Translation Initiation in Eukaryotes: Mechanisms and Biological Targets. *Cell* **136**, 731–745 (2009).
15. Aylett, C. H. S. & Ban, N. Eukaryotic aspects of translation initiation brought into focus. *Philos. Trans. R. Soc. Lond. B. Biol. Sci.* **372**, (2017).
16. Dever, T. E., Dinman, J. D. & Green, R. Translation Elongation and Recoding in Eukaryotes. *Cold Spring Harb. Perspect. Biol.* **10**, a032649 (2018).
17. Hellen, C. U. T. Translation Termination and Ribosome Recycling in Eukaryotes. *Cold Spring Harb. Perspect. Biol.* **10**, a032656 (2018).
18. Yusupova, G. & Yusupov, M. Crystal structure of eukaryotic ribosome and its complexes with inhibitors. *Philosophical Transactions of the Royal Society B: Biological Sciences* **372**, 20160184 (2017).
19. Browne, G. J. & Proud, C. G. Regulation of peptide-chain elongation in mammalian cells. *Eur. J. Biochem.* **269**, 5360–5368 (2002).
20. Frank, J., Gao, H., Sengupta, J., Gao, N. & Taylor, D. J. The process of mRNA–tRNA translocation. *PNAS* **104**, 19671–19678 (2007).
21. Scolnick, E. M. & Caskey, C. T. Peptide Chain Termination, V. the Role of Release Factors in Mrna Terminator Codon Recognition. *PNAS* **64**, 1235–1241 (1969).

22. Aitken, C. E. & Lorsch, J. R. A mechanistic overview of translation initiation in eukaryotes. *Nature Structural & Molecular Biology* **19**, 568–576 (2012).
23. Bohlen, J., Fenzl, K., Kramer, G., Bukau, B. & Teleman, A. A. Selective 40S Footprinting Reveals Cap-Tethered Ribosome Scanning in Human Cells. *Molecular Cell* **79**, 561-574.e5 (2020).
24. Querido, J. B. et al. Structure of a human 48S translational initiation complex. *Science* **369**, 1220–1227 (2020).
25. Muckenthaler, M., Gray, N. K. & Hentze, M. W. IRP-1 binding to ferritin mRNA prevents the recruitment of the small ribosomal subunit by the cap-binding complex eIF4F. *Mol. Cell* **2**, 383–388 (1998).
26. Jackson, R. J., Hellen, C. U. T. & Pestova, T. V. The mechanism of eukaryotic translation initiation and principles of its regulation. *Nat. Rev. Mol. Cell Biol.* **11**, 113–127 (2010).
27. Simonetti, A., Guca, E., Bochler, A., Kuhn, L. & Hashem, Y. Structural Insights into the Mammalian Late-Stage Initiation Complexes. *Cell Reports* **31**, 107497 (2020).
28. Kozak, M. Point mutations define a sequence flanking the AUG initiator codon that modulates translation by eukaryotic ribosomes. *Cell* **44**, 283–292 (1986).
29. Kozak, M. The scanning model for translation: an update. *Journal of Cell Biology* **108**, 229–241 (1989).
30. Calvo, S. E., Pagliarini, D. J. & Mootha, V. K. Upstream open reading frames cause widespread reduction of protein expression and are polymorphic among humans. *PNAS* **106**, 7507–7512 (2009).
31. Morris, D. R. & Geballe, A. P. Upstream open reading frames as regulators of mRNA translation. *Mol. Cell Biol.* **20**, 8635–8642 (2000).

32. Hinnebusch, A. G. Translational regulation of *gcn4* and the general amino acid control of yeast. *Annu. Rev. Microbiol.* **59**, 407–450 (2005).
33. Novoa, E. M. et al. Analogs of natural aminoacyl-tRNA synthetase inhibitors clear malaria *in vivo*. *PNAS* **111**, E5508–E5517 (2014).
34. Hoepfner, D. et al. Selective and Specific Inhibition of the *Plasmodium falciparum* Lysyl-tRNA Synthetase by the Fungal Secondary Metabolite Cladosporin. *Cell Host Microbe* **11**, 654–663 (2012).
35. Baragaña, B. et al. A novel multiple-stage antimalarial agent that inhibits protein synthesis. *Nature* **522**, 315–320 (2015).
36. Ahyong, V. et al. Identification of *Plasmodium falciparum* specific translation inhibitors from the MMV Malaria Box using a high throughput *in vitro* translation screen. *Malaria Journal* **15**, 173 (2016).
37. Waters, A. P., Syin, C. & McCutchan, T. F. Developmental regulation of stage-specific ribosome populations in Plasmodium. *Nature* **342**, 438–440 (1989).
38. Li, J. et al. Regulation and trafficking of three distinct 18 S ribosomal RNAs during development of the malaria parasite. *Journal of Molecular Biology* **269**, 203–213 (1997).
39. Pavlovic Djuranovic, S. et al. *Plasmodium falciparum* translational machinery condones polyadenosine repeats. *eLife* **9**, e57799 (2020).
40. Chappell, L. et al. Refining the transcriptome of the human malaria parasite *Plasmodium falciparum* using amplification-free RNA-seq. *BMC Genomics* **21**, (2020).
41. Caro, F., Ahyong, V., Betegon, M. & DeRisi, J. L. Genome-wide regulatory dynamics of translation in the *Plasmodium falciparum* asexual blood stages. *eLife* **3**, e04106 (2014).

Chapter 2:

Tool Development to Produce *In Vitro* Translation Lysates

This chapter is a reprint of:

Valentina E. Garcia*, Jamin Liu*, Joseph L. DeRisi. Low-cost touchscreen driven programmable dual syringe pump for life science applications. *HardwareX* Volume 4, (2018), e00027:

<https://doi.org/10.1016/j.ohx.2018.e00027>.

*These authors contributed equally to this work

Non-figure supplemental files can be found with the original work

2.1 Abstract:

Syringe pumps are powerful tools able to automate routine laboratory practices that otherwise consume large amounts of manual labor time. Commercially available syringe pumps are expensive, difficult to customize, and often preset for a narrow range of operations. Here, we show how to build a programmable dual syringe pump (PDSP) that overcomes these limitations. The PDSP is driven by a Raspberry Pi paired with a stepper motor controller to allow maximal customization via Python scripting. The entire setup can be controlled by a touchscreen for use without a keyboard or mouse. Furthermore, the PDSP is structured around 3D printed parts, enabling users to change any component for their specific application. We demonstrate one application of the PDSP by using it to generate whole cell lysates using a cell homogenizer in an automated fashion.

2.2 Hardware in context

Syringe pumps have a wide variety of uses across fields from engineering to biology. Their primary purpose is to continuously dispense precise volumes over a set amount of time. They save time by running unsupervised and provide more consistency than human hands. A dual syringe pump allows for two syringes to have coordinated actions, broadening the potential applications. In particular, dual syringe pumps have the power to automate a number of routine and repetitive protocols in the life sciences.

Our lab initially conceived of building a dual syringe pump that could be used to make *Plasmodium falciparum* whole cell extracts used for *in vitro* translation. Previously, we generated lysates by passing purified infected red blood cells through an Isobiotek cell homogenizer using a ball bearing with 4um clearance. Frozen pellets of purified parasites were

thawed, loaded into one 3mL syringe, and passed through the homogenizer into a second 3mL syringe. The lysate was then passed back into the first syringe. This back and forth cycle was repeated up to 20 times per parasite pellet [1]. This process takes between 20-30 mins per parasite pellet and the resistance in the device makes it physically taxing on the wrists and thumbs. In the lab, lysate generation was often a rate-limiting step when making *in vitro* translation extracts due to the manual and tedious nature of the process. It also entailed unacceptable amounts of user-dependent variation between lysate preparations. In the worst cases, syringes would break or the plunger would deform as pressure was applied unevenly. A customizable PDSP addresses all of these issues not only for our uses, but also for other applications of the Isobiotech Cell homogenizer such as *C. elegans* lysis [2] and mammalian cell culture homogenization [3].

We reasoned that this process could be easily replaced with a programmable dual syringe pump. However, commercially available dual syringe pumps have a number of limitations, including cost and flexibility. As of this writing, commercially available dual syringe pumps cost upwards of \$1500 [4] and coordinated programmable motion tends to be limited. Additionally, the physical configuration of commercial products makes alternative mounting options difficult. Previously described lab-built syringe pumps include single syringe pumps [5] or pumps that operate as part of a larger device, such as an auto-sampler [6]. To our knowledge, there are no current solutions that feature a customizable graphical user interface (GUI) touchscreen, which greatly simplify use by eliminating the need for a keyboard and/or mouse. Thus, we designed, built, and tested a PDSP that can be easily used in the lab using a touch-screen but that can also be customized for any use. This PDSP drives two independent pumps operating under a single

microcontroller which makes it not only amenable to synchronized pumping patterns, but also makes it extensible (up to 16 pumps) for multiplexed liquid handling operations.

2.3 Hardware description

Our custom PDSP is constructed on an extruded aluminum frame that can be mounted horizontally or vertically. For our specific application, we chose a vertical mount to allow the cell homogenizer to be immersed in ice (Figure 2.1A and 2.1B). The PDSP utilizes two NEMA-14 stepper motors (StepperOnline) that create precise volume changes even at high-torque. The motors are driven by a Pi-Plate MOTORplate controller (Pi-Plates, Inc.) mated to a Raspberry Pi (v3 Model B). Integrated limit switches provide for simple and accurate “homing” procedures. To make the PDSP easy to use for routine laboratory stand-alone use, the PDSP is operated via an attached touchscreen (Landzo), without a keyboard or mouse.

While this PDSP is specialized to lysate generation, alternative applications may have different requirements. We designed this device so that it could be adapted to many different environments, such as a biohazard hood, and for many different tasks, such as microfluidic experiments [5]. To allow for maximum customization, we made the PDSP modular with 3D printed parts that can be interchanged to accommodate different volume syringes. By simply changing the dimensions of the printed parts the syringes can be set to any distance apart. The cell homogenizer holder can be interchanged with any other user-designed holder. Our custom Python/Tkinter interface can be easily configured to drive the stepper motors at different speeds allowing for a range of flow rates or even gradients of flow rates. The Pi-Plate MOTORplates can be stacked, allowing a single Pi and interface to simultaneously control up to 8 PDSPs (16 syringes) for high volume production environments.

2.4 Design files

Table 2.1 contains links to the STL design files for all 3D printed parts described here:

- The **Motor Base** (Figure 2.2A) secures the two stepper motors and holds the Aluminum Heat Sink Plate against the T-profile rails.
- The **Toe Hold** (Figure 2.2B) positions the linear motion shafts against the T-profile rails.
- The **Syringe Stabilizer** (Figure 2.2C) holds the syringe body in place by securing both the barrel and the barrel flange parallel to the movement direction of the plunger.
- The left and right **Plunger Movers** (Figure 2.2D) hold the plunger flange of the syringes and move them along the linear motion shaft as the T8 threaded rods turn according to the stepper motors to change the volume.
- The **Pi Base** (Figure 2.2E) and **Cover** (Figure 2.2F) secure the Raspberry Pi along the T-profile rails and insulates it from short-circuiting against nearby conductive material. It also protects the Raspberry Pi from dust and accidental splashes from the ice bucket.
- The **Screen Mount Top** and **Bottom** (Figure 2.2G) hold the touch screen at eye-level when the PDSP is constructed vertically. Situated in front of the motors, it keeps the touchscreen a safe distance from the generated heat.
- The **Cell Homogenizer Holder** (Figure 2.2H) positions the cell homogenizer in alignment with luer lock syringes such that no additional tubing is necessary. It also allows the cell homogenizer to be in contact with ice at all times.
- The **Right-Angle Brackets** are used to position the syringe pump vertically on a breadboard. If desired, they can be 3D printed rather than purchased.
- The **Aluminum Heat Sink Plate** is placed between the stepper motors on the Motor Base and the T-profile rails to rapidly disperse heat generated from the stepper.

2.5 Build Instructions

The essential PDSP components are 3D printed. The remaining hardware can be acquired online from common hardware suppliers, such as McMaster-Carr. All electronic parts can be acquired from common electronics suppliers, such as Adafruit or Microcenter (see Bill of Materials).

The additional tools required for assembly include:

- M2.5 Tap
- M3 Tap
- Metric Hex Key Set
- Imperial Hex Key Set
- Philips Screwdriver
- Wire Stripper
- Soldering iron
- Hack-saw or chop-saw
- Drill Press

2.5.1 Preparation of electronic components

It is useful to prepare the electronic components prior to assembly. First, solder wires to the GND pin and the N pin on the leaf switches as outlined in Figure 2.3. Wrap the exposed solder and pin with heat shrink to protect the connection. To keep the electronic wiring neat, braid the four wires of each stepper motor and twist together the two wires of each leaf switches. Next, attach one heat sink onto the rear of each stepper motor by applying an appropriately sized piece of thermal tape to the rear end-cap and firmly pressing the heat sink to the tape. To prepare

the motor power supply, cut and strip the wires of the 2.1mm female/male barrel jack extension cable to separate the power and ground wires.

Finally, attach the Raspberry Pi onto the Pi base (Figure 2.2E) using four M2.5x5mm screws. Next, attach the PiPlates Motor Plate to the Raspberry Pi header pins by carefully applying even pressure on the plate while pushing the two components together to prevent bending any pins. Once attached, secure the PiPlates Motor Plate onto the Pi base using another four M2.5 x 5mm screws.

2.5.2 Hardware Preparation

3D print each of the necessary parts from the provided design files, including four right-angle brackets if not using ThorLab's precision cut components. We recommend printing with ABS material with a low-density fill. Cut the two T8 lead screws to 25cm each and the two linear motion shafts to 21.5cm each. Saw the aluminum plate to the appropriate dimensions according the Aluminum Heat Sink Plate STL file (Supplementary File 1 available with the original publication). Using a drill press, drill two through holes as specified into the aluminum plate for later assembly onto the T-profile rails. Tap M2.5 and M3 holes into the 3D printed parts as indicated in their respective STL files.

2.5.3 Hardware Assembly

The complete assembly of the PDSP as described below can be seen as a time-lapse in Supplementary file 2 available with the original publication.

1. Attach the compact end-feed fastener with M5 x 5mm screws to each through hole of the Motor Base (Figure 2.2A), Toe Hold (Figure 2.2B), Syringe Stabilizer (Figure 2.2C), Pi Base (Figure 2.2E), and Cell Homogenizer Holder (Figure 2.2H). Attach the compact

end-fasteners of two M5 x 8mm through the previously drilled holes aluminum Heat Sink Plate (Figure 2.4A).

2. Attach each of the two pillow block bearings to the Extract Maker Holder (Figure 2.4B) using M3 x 20mm socket head screws.
3. Insert one copper nut and one linear ball bearing into each of the Plunger Movers (Figure 2.2D). Attach the copper nut using four M2.5 x 5mm socket head screws per nut and secure the linear ball bearing into its designated slot with silicone if necessary (Figure 2.4C).
4. Thread the one T8 lead screws into the copper nut and slide one linear motion shaft through the linear ball bearing on each of the two Plunger Movers (Figure 2.4C).
5. Making sure each part is oriented correctly, slide the four metal bars through the Syringe Stabilizer, and secure into the Cell Homogenizer Holder. The arms on each of the plunger mover should be on the outside of the linear structure and each pointed towards the Syringe Stabilizer (Figure 2.4B and 2.4D).
6. On the other end, slide the four metal bars towards the Toe Hold making sure the linear motion shaft is secured by the Cell Homogenizer Holder on one end and by the Toe Hold on the other end (Figure 2.4D).
7. Slide the Toe Hold, the Syringe Holder, and the Cell Homogenizer Holder together onto the T-profile rails by correctly slotting the compact end-feeder into the rails. Do not tighten the M5 screws yet (Figure 2.4D).
8. Attach and secure the stepper motors onto the motor base using four M3 x 5mm per motor (Figure 2.4E).

9. Slide the motor base with attached motors onto the T-profile rails on the side closest to the Toe Hold. Do not yet tighten the M5 screws.
10. Attach the couplers between the T8 threaded rods and the stepper motors by carefully sliding all the moving parts along the T-profile rails towards each other. After making sure that the T8 threaded rods and the motors are completely aligned, secure the couplers by tightening the attached screws (Figure 2.4F).
11. Slide the Aluminum Heat Sink Plate onto the T-profile rails beneath the stepper motors on the Motor Base.
12. If desired, ensure there is sufficient space between the Cell Homogenizer Holder and the end of the T-profile rails to place an ice bucket. Finally, secure all the parts to the T-profile rails by tightening all ten of the M5 screws.
13. Attach the Screen Mount-Bottom (Figure 2.2I) onto the Motor Base using four M2.5 x 20mm screws. The correct orientation should allow the touchscreen to rest on the base without bending the ribbon cable. Then, sandwich the touchscreen between the Screen Mounts using four more M2.5 x 20mm screws (Figure 2.4G).
14. Attach the leaf switches associated with each stepper motor to the Syringe Stabilizer on their respective sides using M2 x 12mm screws (Figure 2.4H).
15. To stand the PDSP vertically, insert one M5 x 8mm screw into the highest through hole on each of the four Right-Angle Brackets. Attach the compact end-feeder into each of these screws and slide them into the bottom of the T-profile rails, closest to the cell homogenizer holder. Do this for the four Right-Angle Brackets for a total of one each on the left and right, and two in the rear (Figure 2.3I).

16. Stand the PDSP up over the breadboard and secure the Right-Angle Brackets onto the base of choice using the ¼" x ¾" long socket screws.
17. Attach the Pi Base on the rear of the PSDP such that it is flush against the top of the T-profile rails (Figure 2.4I)
18. Thread the wires neatly using the through holes on the Pi Base before connecting each to the Raspberry Pi according to the Electronic Wiring Schematics (Figure 2.3).
19. Slide on and secure the Pi Cover (Figure 2.2H) to the rear of the Pi Base using M2.5 x 10mm screws (Figure 2.4I).
20. Check that all the screws on the PDSP are appropriately tightened prior to use.

5.4 Software setup

To install our software and GUI, we have provided the Raspberry Pi image on our lab website (<http://derisilab.ucsf.edu/>). Download the image onto a MicroSD card. We suggest using the free software Etcher to create bootable SD cards⁷. Once installed, unmount the MicroSD and insert it into the Raspberry Pi. Plug in the Raspberry Pi power cord to a conventional outlet to turn it on. To power the stepper motors, connect a conventional 7.5V power supply to the barrel jack extension cable attached to the PiPlate Motor Plate.

Alternatively, install the latest release of Raspbian for the Raspberry Pi, the MOTORplate drivers (via the PIP Python repository: `sudo pip install pi-plates`), and the source code for the PDSP (Supplementary File 3 available with the original publication) and interface manually. The resolution of the Pi can be set to fit any screen by altering the `/boot/config.txt` file. For the touchscreen used here, add the following lines to the end of the `config.txt` file:

```
max_usb_current=1  
  
hdmi_group=2
```

```
hdmi_mode=1
```

```
hdmi_mode=87
```

```
hdmi_cvt 800 480 60 6 0 0 0
```

2.6 Operation Instructions

We have designed a GUI optimized for safe and streamlined operation of the PDSP as an automated cell homogenizer (Figure 2.5). The software was written with internal limitations to protect both the sample being lysed and the PDSP components. For the push-pull pumping motion, we strongly encourage users to consider employing our intuitive GUI to operate the PDSP. The complete operation instructions of the PDSP as an automated cell homogenizer is described below and can be seen as a video clip in Supplementary File 2 (available with the original publication).

2.6.1 Operation Instructions for the provided GUI

1. Turn on the Raspberry Pi by plugging it in. Once the Desktop is loaded, the terminal application will launch and open the provided GUI in full-screen automatically (Figure 2.5).
2. Once the GUI has launched, press the “*HOME*” button to bring both Plunger Movers to their starting position against the Syringe Stabilizer. Pay attention to the popup alerts and ensure that the PDSP is empty before homing.
3. Load a minimum of 1mL of sample into the cell homogenizer as usual. Make sure the sample is in only one syringe before loading it onto the PDSP.
4. Using the left and right arrow keys under “Volume Control” set the volume of sample in the loaded syringe. Once again, follow the popup alert instructions and ensure the cell homogenizer and syringes have not yet be placed onto the PDSP.

5. Place a filled ice bucket underneath the Cell Homogenizer Holder and insert the cell homogenizer onto the device. Ensure that each syringe is held appropriately by both the Syringe Stabilizer and the left or right Plunger Movers.
6. Using the left and right arrow keys under “Cycle Control,” set the desired number of push-pull cycles. If the cycle number is not explicitly set, the software will default to 20 cycles.
7. Press “*START*.” The number of elapsed cycles along with two timers, a countdown timer based on the estimated duration and a time elapsed counter, should appear.
8. When in doubt, there is an emergency “*STOP*” button that will immediately stop and reset all motors. To reinitialize, remove the cell homogenizer and syringes from the PDSP. Then, return to step 2 outlined here.

2.6.2 Customization Suggestions for Operation

While we use the PDSP to automate *P. falciparum* lysis using an Isobiotech Cell Homogenizer, the PDSP is adaptable to other tasks. As previously described, the PDSP is programmed on and executed from a Raspberry Pi running the Raspbian operating system. Our software to control the PDSP is written in Python using commands from the PiPlates MOTORPlate Users Guide documentation [8]. Our object oriented GUI is also designed in Python using Tkinter.

To customize the PDSP for a variety of other applications, users can reference both the script that we have written as well the extensive documentation provided by PiPlate. The PiPlate MOTORplate is highly customizable, offering a wide variety of options for stepper movement in terms of stepper size, speed, and acceleration or deceleration. Furthermore, the PiPlates MOTOR library is highly compatible with the GPIO control library, allowing flexibility in the control of

the stepper motors. While python scripts can be executed from the Raspberry Pi command line using a keyboard, users can also create a specialized GUI for their own purposes.

The PDSP presented here is already compatible with a number of different pumping systems. These include, but are not limited to, continuous infusion systems, dual injection systems, and inverse linear constant flow systems. While this PDSP is relatively simple, we can add complexity by attaching up to eight PiPlate MOTORplates powered by one Raspberry Pi, allowing for control of up to sixteen stepper motors simultaneously.

2.7 Validation and Characterization

2.7.1. Characterization of the PDSP as a syringe pump

To characterize the PDSP, we tested the minimum and maximum flow rates provided by the stepper motors on a 3 mL syringe. By timing the flow of liquid, we were able to measure the consistency and the dynamic range of flow rates for the PDSP (Figure 2.6A). We compared these values with the theoretical minimum and maximum flow rates that were calculated as described below:

Let the syringe cross-sectional area have units of mm^2 and be defined as:

$$A = \pi \times ((\text{syringe diameter})/2)^2$$

Let the linear distance conversion factor (C) have units of mm/degree and be defined as:

$$C = (\text{Thread distance})/(360^\circ)$$

For a T8 threaded rail:

$$C = (8 \text{ mm})/(360^\circ) = (1 \text{ mm})/(45^\circ)$$

Thus, we can calculate the theoretical flow rate as follows:

$$\text{Flow Rate (uL/(sec))} =$$

$$(A(\text{mm})^2) \times \text{step size } (^\circ/\text{step}) \times \text{step rate } (\text{step}/\text{sec}) / (C(\text{mm}/^\circ))$$

The measured flow rates were consistent with the theoretical flow rates calculated using the manufactured syringe diameters and the stepper motor step sizes. This gives us confidence in the PDSP as an appropriate alternative to commercial syringe pumps. Here we provide the dynamic range of the PDSP in terms of the theoretical minimum and maximum flow rates of various compatible syringe sizes (Table 2.3).

2.7.2 Validation of the PDSP as a cell homogenizer

To demonstrate the ability of the PDSP to replace manual cell lysis we compared the two methods directly. In brief, *Plasmodium falciparum* parasites were harvested as previously published¹ and split into two pools, one for manual lysis and one for lysis using the PDSP. We either passed the lysate back-and-forth through the Isobiotec cell homogenizer for 20 cycles by hand or the PDSP controlled by the GUI interface passed the lysate through. Lysates were then collected and centrifuged at 13,000xg for 10 mins at 4C. The supernatant was aliquoted and flash frozen in liquid nitrogen.

One aliquot was taken for each lysis method and used in an *in vitro* translation reaction as previously published with a few modifications [1]. Each 10uL reaction consisted of 7uL of lysate, 10 μ M amino acid mixture, 20 mM HEPES/KOH pH 8.0, 75 mM KOAc, a range of 1-5mM Mg(OAc)₂, 2 mM DTT, 0.5 mM ATP, 0.1 mM GTP, 20 mM creatine phosphate, 0.2 μ g/ μ l creatine kinase, and 0.5 pmoles of Nanoluciferase reporter RNA. Reactions were done in triplicate, incubated at 37C for 45 mins, and stopped with the addition of 10 uM cycloheximide. The Nanoluciferase reporter RNA consists of the 130 base pairs directly 5' of PFE_1248300 followed by the Nanoluciferase coding sequence [9] in the 3' UTR of HRP. All RNA was generated off of plasmid digested with PVUII and APAL1 using T7 transcription (Figure 6B).

After transcription, the DNA template was digested with Turbo DNase (Thermo Fisher) and the RNA was purified using RNA Clean and Concentrate-25 kit (Zymo). Nanoluciferase reactions were performed using Promega's Nano-Glo Luciferase Assay System. In brief, 10 uL of 1:50 Nanoluciferase substrate:Nanoluciferase buffer was added to each reaction and incubated at room temperature for a minimum of 5 minutes before reading with a 6 second integration on a Promega GloMax-Multi microplate reader.

Our results showed that lysates generated by hand and by the PDSP performed similarly, indicating the PDSP can be used to replace manual lysis for generating *in vitro* translation extracts (Figure 2.6C).

2.7.3 Conclusion/Device Overview

We have constructed a programmable syringe pump that can be used for biological life science applications. Not only is the PDSP more affordable than commercially available options, but it is also modular and programmable, allowing the user to customize the device for specific tasks or experiments. Here, we have demonstrated that the PDSP can be used to automate and standardize the time-consuming task of *P. falciparum* lysis. Overall, the PDSP can be used as an affordable and customizable alternative to traditional syringe pumps to automate any number of routine laboratory practices.

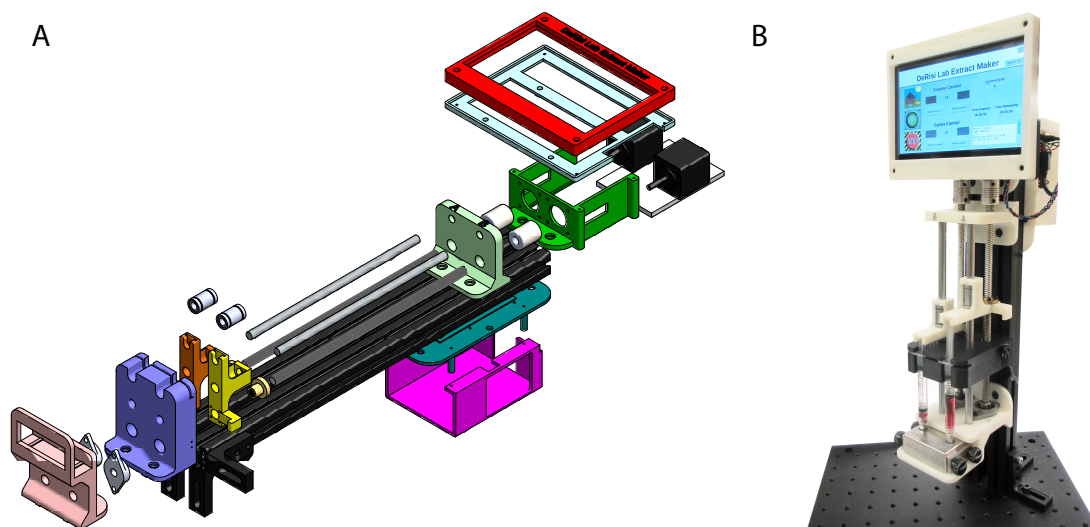


Figure 2.1: The assembled PDSP

a) A 3D rendering of the PDSP with all components visible. b) A photograph of the completed PDSP standing vertically.

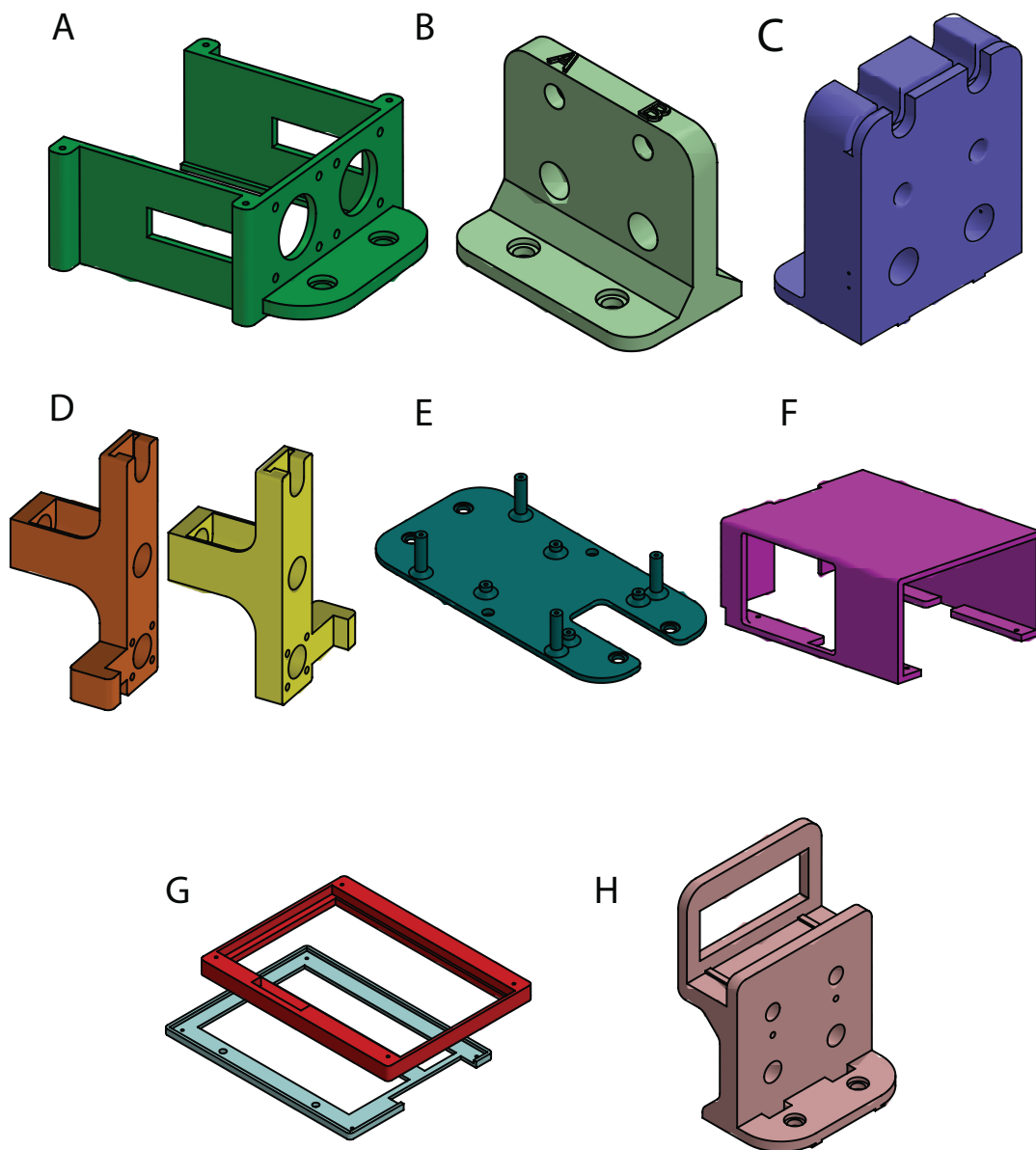


Figure 2.2: Models of all 3D printed PDSP components

a) Motor Base, b) Toe Hold, c) Syringe Stabilizer, d) Left and right Plunger Movers, e) Pi Base, f) Pi Cover, g) Top and bottom Screen Mounts, and h) Cell Homogenizer Holder

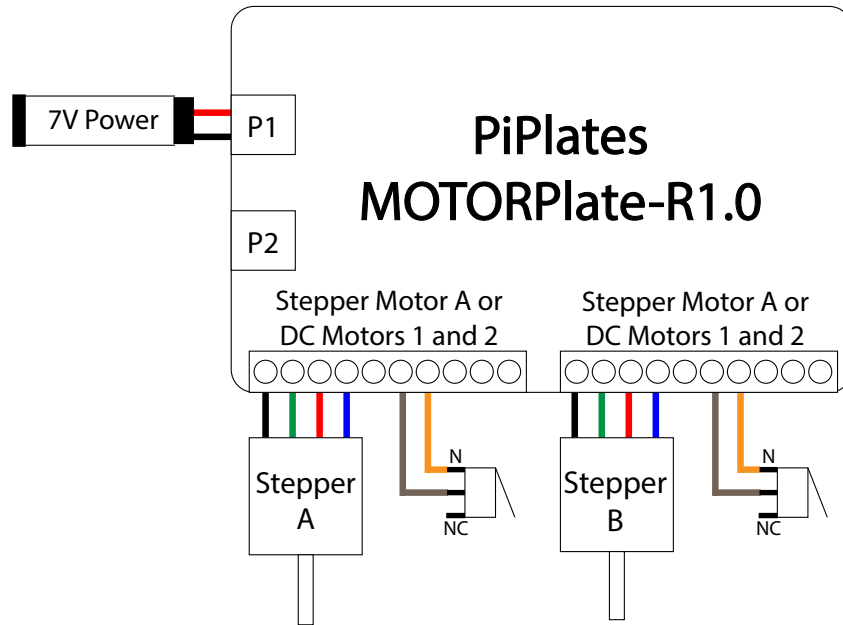


Figure 2.3: Electrical wiring schematic of the PDSP

A diagram indicating where the wires conned to the PiPlates MOTORPlate-R1.0

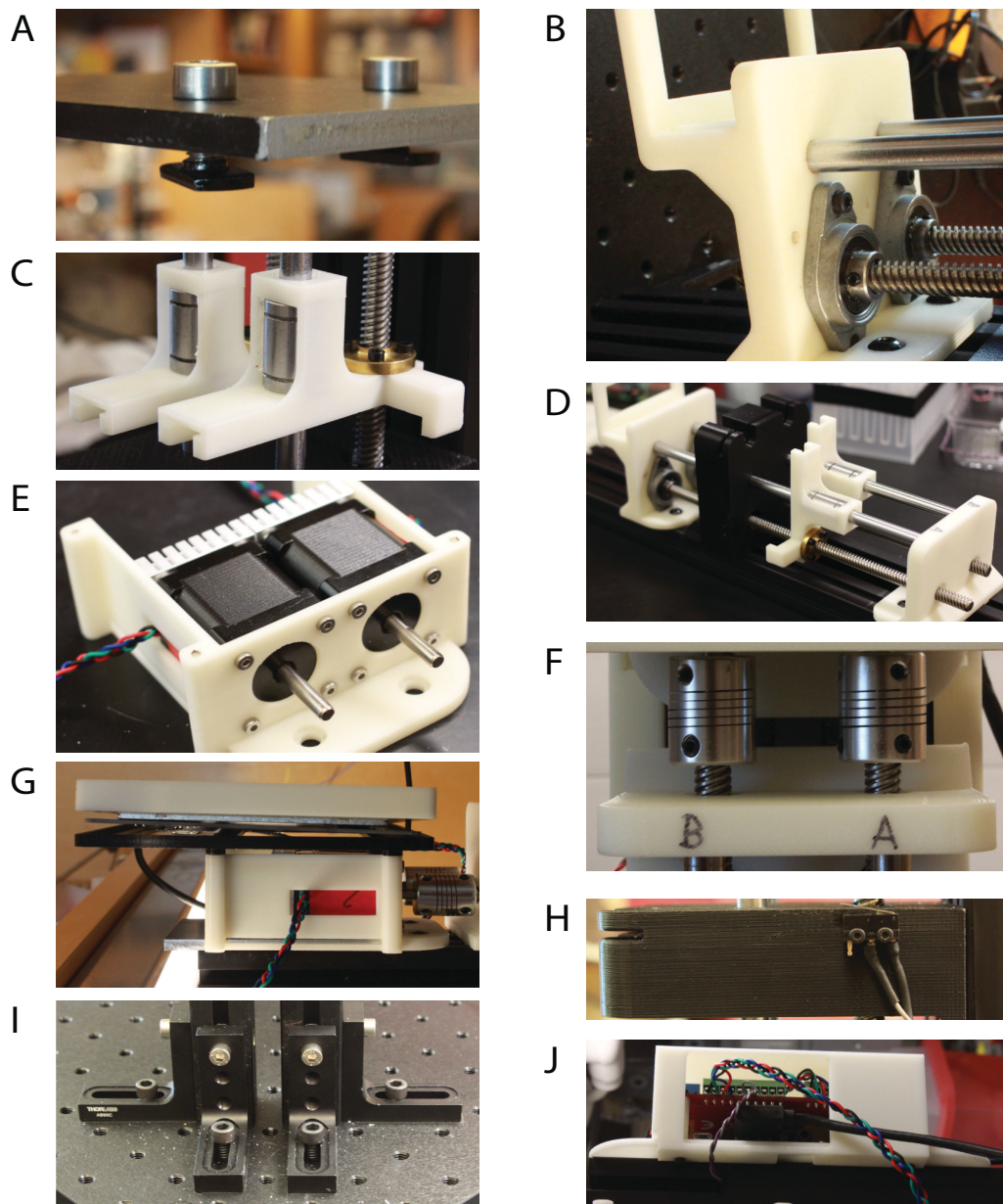


Figure 2.4: Images of key PDSP assembly steps as described in 5.4 Hardware Assembly

a) Example of the compact end-feed fastener assembly. b) The pillow block bearings, the threaded rods, and the smooth rods attached to the Extract Maker Holder. c) The syringe movers on the smooth and threaded rods. d) The copper nut and linear motion shaft assembled with the Syringe Movers on the smooth and threaded rods. e) The two stepper motors assembled with the Motor Base. f) The couplers attached to each motor and the threaded rods. g) The Screen Mount Top and Bottom sandwiching the touchscreen and assembled on the Motor Base. h) The limit switches attached to the Syringe Stabilizer component. i) The Right-Angle Brackets positioned on the aluminum breadboard to stand the PDSP vertically. j) The Raspberry Pi and PiPlates Motor Plate attached to the Pi base.

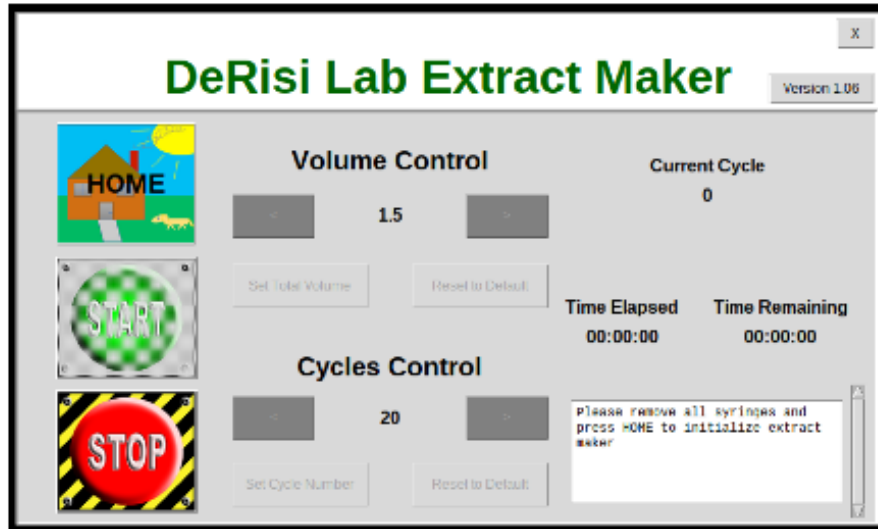


Figure 2.5: The PDSP's GUI interface

GUI interface designed in Python using Tkinter for use of the PDSP with the cell homogenizer

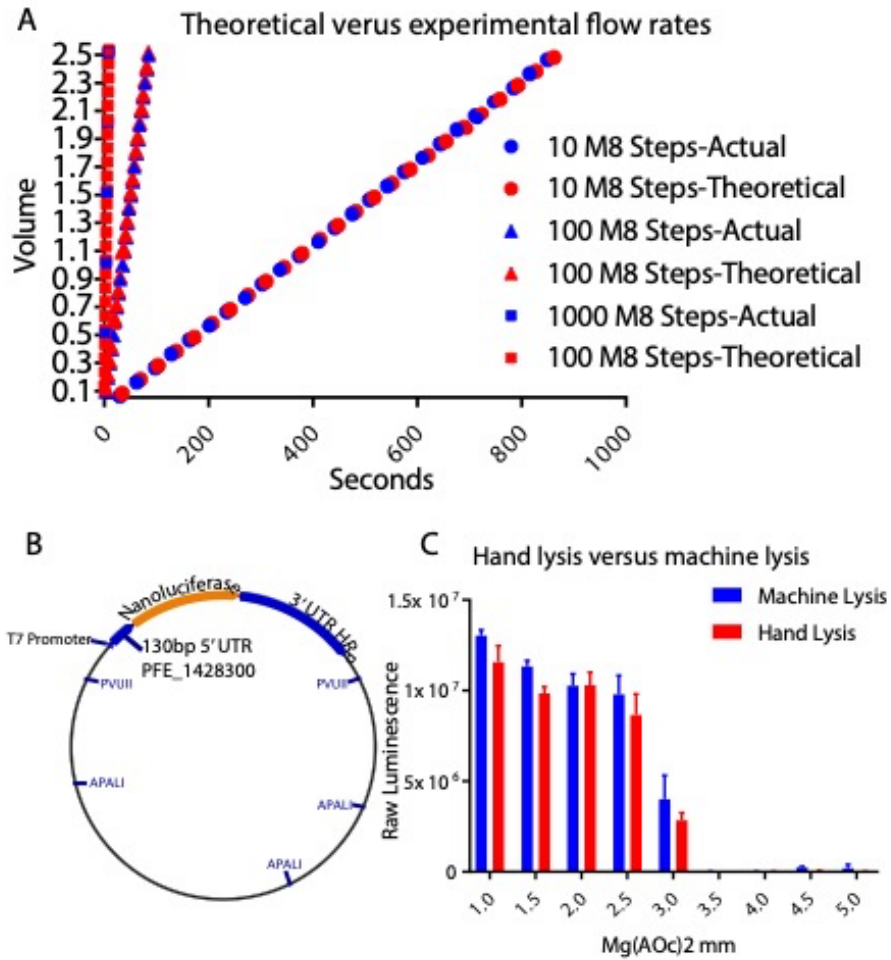


Figure 2.6: Characterization of the PDSP for lysate generation

a) Dynamic Range of Flow Rate of PDSP with 3mL Syringes. b) Plasmid construct for validation of translational activity in the lysates. c) Translational activity, measured by total luciferase signal, of the lysates generated by hand or the PDSP.

Table 2.1: Design files for all 3D printed parts

Design file name	File type	Open source license	Location of the file
Motor Base (Figure 2.2A)	STL	CC-BY-SA 4.0	https://3dprint.nih.gov/discover/3dpx-008783
Toe hold (Figure 2.2B)	STL	CC-BY-SA 4.0	https://3dprint.nih.gov/discover/3dpx-008783
Syringe Stabilizer (Figure 2.2C)	STL	CC-BY-SA 4.0	https://3dprint.nih.gov/discover/3dpx-008783
Plunger Mover-Left (Figure 2.2D)	STL	CC-BY-SA 4.0	https://3dprint.nih.gov/discover/3dpx-008783
Plunger Mover-Right (Figure 2.2D)	STL	CC-BY-SA 4.0	https://3dprint.nih.gov/discover/3dpx-008783
Pi Base (Figure 2.2E)	STL	CC-BY-SA 4.0	https://3dprint.nih.gov/discover/3dpx-008783
Pi cover (Figure 2.2G)	STL	CC-BY-SA 4.0	https://3dprint.nih.gov/discover/3dpx-008783
Screen Mount-Bottom (Figure 2.2G)	STL	CC-BY-SA 4.0	https://3dprint.nih.gov/discover/3dpx-008783
Screen Mount-Top (Figure 2.2G)	STL	CC-BY-SA 4.0	https://3dprint.nih.gov/discover/3dpx-008783
Cell Homogenizer Holder (Figure 2.2H)	STL	CC-BY-SA 4.0	https://3dprint.nih.gov/discover/3dpx-008783
Right-Angle Bracket	STL	CC-BY-SA 4.0	https://3dprint.nih.gov/discover/3dpx-008783
Aluminum Heat Sink Plate	STL	CC-BY-SA 4.0	Supplementary attachment

Table 2.2: List of all purchased items with number required and cost

Designator	Component	#	Cost per unit (USD)	Total cost (USD)	Source of materials	Material type
<u>Hardware</u>						
M2 x 0.4 mm Thread x 12 mm Long Socket Head Screw	91290A019	4	\$0.12	\$0.47	McMaster-Carr	Steel
M2.5 x 0.45 mm Thread x 20 mm Long Socket Head Screw	91290A108	8	\$0.28	\$2.24	McMaster-Carr	Steel
M2.5 x 0.45 mm Thread x 10 mm Long Socket Head Screw	91290A103	16	\$0.15	\$2.45	McMaster-Carr	Steel
M2.5 x 0.45 mm Thread x 5 mm Philips Flat Head Screw	92010A014	4	\$0.03	\$0.13	McMaster-Carr	Steel
M3 x 0.5 mm Thread x 5 mm Long Socket Head Screw	91290A110	8	\$0.08	\$0.66	McMaster-Carr	Steel
M3 x 0.5 mm Thread x 20 mm Long Socket Head Screw	91290A123	2	\$0.10	\$0.20	McMaster-Carr	Steel
M5 x 0.8 mm Thread x 8 mm Long Socket Head Screw	91290A222	12	\$0.09	\$1.08	McMaster-Carr	Steel

Designator	Component	#	Cost per unit (USD)	Total cost (USD)	Source of materials	Material type
M5 x 0.8 mm Thread x 15 mm Long Socket Head Screw	91290A231	6	\$0.15	\$0.88	McMaster-Carr	Steel
1/4"-20 Thread x 3/4" Long Socket Head Screw	5709A18	4	\$0.15	\$0.60	McMaster-Carr	Steel
Compact End-Feed Fastener, M5, for 20mm T-Slotted Framing	5537T161	18	\$0.50	\$8.96	McMaster-Carr	Steel
1.00" X 1.00" Smooth Surface T-Slotted Profile Aluminum	1010-S-Black-FB	2	\$7.20	\$14.40	80/20 Inc.	Aluminum
Sheet - 71x90x5mm	1247	1	\$21.42	\$21.42	OnlineMetals	Aluminum
T8 Lead Screw + Copper Nut + Coupler + Pillow Block Bearings Lead Screw Set (300mm)	KINGPRINT-KIT	2	\$12.52	\$25.04	Amazon	Steel
Linear Motion 8 mm Shaft x 330 mm Length	kit11868	2	\$15.18	\$30.36	Amazon	Steel
Linear Bearing Ball Bushing	OS16211	2	\$1.21	\$2.43	Amazon	Steel

Electronics

Designator	Component	#	Cost per unit (USD)	Total cost (USD)	Source of materials	Material type
Raspberry Pi 3 - Model B - ARMv8 with 1G RAM	3055	1	\$35.00	\$35.00	Adafruit	Other
5V 2.4A Switching Power Supply with 20AWG MicroUSB Cable	1995	1	\$7.50	\$7.50	Adafruit	Other
16GB microSDHC Class 10 Flash Memory Card	415141	1	\$7.99	\$7.99	Microcenter	Other
7" Touch Screen for Raspberry Pi	B01ID5BQTC	1	\$42.88	\$42.88	Amazon	Other
Right HDMI Male to Left HDMI Male Cable	B06XT2JS1G	1	\$7.99	\$7.99	Amazon	Other
MOTORplate 2.1mm female/male barrel jack extension cable	MOTORR1 327	1 1	\$39.99 \$2.95	\$39.99 \$2.95	Pi Plates Adafruit	Other Other
7.5 Volt 2.4 Amp Power Adapter	B006QYXFRO	1	\$21.99	\$21.99	Amazon	Other
Nema 14 Bipolar 1.8deg 23Ncm 0.5A 7.5V 35x35x42mm	14HS17-0504S	2	\$14.27	\$28.54	StepperOnline	Other

Designator	Component	#	Cost per unit (USD)	Total cost (USD)	Source of materials	Material type
Omron Snap Action Switch	COM-00098	2	\$1.95	\$3.90	Sparkfun	Other
Heatsink 35mm x 35mm x 10mm	B00MJVXB9K	2	\$1.39	\$2.77	Amazon	Aluminum
Heat Sink Thermal Tape 80mm x 80mm	1468	1	\$4.50	\$4.50	Adafruit	Other
Wire Assortment	38687	1	\$9.99	\$9.99	Microcenter	Other
Heat Shrink Tubing Assortment	544023	1	\$2.99	\$2.99	Microcenter	Other
Solder	860585	1	\$16.99	\$16.99	Microcenter	Other
<u>Optional</u>						
Aluminum Breadboard 12" x 12" x 1/2", 1/4"-20 Taps	MB12	1	\$151.00	\$151.00	Thorlabs	Aluminum
Slim Right-Angle Bracket with Counterbored Slot & 1/4"-20 Tapped Holes	AB90C	4	\$26.25	\$105.00	Thorlabs	Aluminum

Table 2.3: Minimum and Maximum Theoretical Flow Rates by the PDSP Based On Syringe Size.

Syringe Size	Diameter (mm)	Minimum Flow Rate (uL/s)	10 Steps/s (uL/s)	100 Steps/s (uL/s)	Maximum Flow rate (mL/S)
			M8 Step size		
1mL	4.78	0.1	0.9	9.0	0.090
3mL	8.66	0.3	2.9	29.5	0.295
5mL	12.06	0.6	5.7	57.1	0.571
10mL	14.5	0.8	8.3	82.6	0.826
20mL	19.13	1.4	14.4	143.7	1.437
30mL	21.7	1.8	18.5	184.9	1.849
50/60mL	26.7	2.8	28.0	280.0	2.800
			Full Step Size		
1 mL	4.78	0.7	7.2	71.8	0.718
3 mL	8.66	2.4	23.6	235.6	2.356
5 mL	12.06	4.6	45.7	456.9	4.569
10 mL	14.5	6.6	66.1	660.5	6.605
20 mL	19.13	11.5	115.0	1149.7	11.497
30 mL	21.7	14.8	147.9	1479.3	14.793
50/60 mL	26.7	22.4	224.0	2239.6	22.396

Chapter 2 References:

1. Ahyong, V. *et al.* Identification of *Plasmodium falciparum* specific translation inhibitors from the MMV Malaria Box using a high throughput *in vitro* translation screen. *Malar. J.* **15**, 173 (2016).
2. Bhaskaran, S. *et al.* Breaking *Caenorhabditis elegans* the easy way using the Balch homogenizer: An old tool for a new application. *Anal. Biochem.* **413**, 123–132 (2011).
3. Sarnataro, D. *et al.* PrP(C) association with lipid rafts in the early secretory pathway stabilizes its cellular conformation. *Mol. Biol. Cell* **15**, 4031–4042 (2004).
4. SyringePump.com - Push-Pull Continuous Infusion, Dual Pump System. Available at: <https://www.syringepump.com/special.php>. (Accessed: 14th March 2018)
5. Lake, J. R., Heyde, K. C. & Ruder, W. C. Low-cost feedback-controlled syringe pressure pumps for microfluidics applications. *PLOS ONE* **12**, e0175089 (2017).
6. Wijnen, B., Hunt, E. J., Anzalone, G. C. & Pearce, J. M. Open-Source Syringe Pump Library. *PLOS ONE* **9**, e107216 (2014).
7. Installing operating system images - Raspberry Pi Documentation. Available at: <https://www.raspberrypi.org/documentation/installation/installing-images/>. (Accessed: 14th March 2018)
8. Code. Pi-Plates (2015).
9. Hall, M. P. *et al.* Engineered Luciferase Reporter from a Deep Sea Shrimp Utilizing a Novel Imidazopyrazinone Substrate. *ACS Chem. Biol.* **7**, 1848–1857 (2012).

Chapter 3:

Identification of Translation Inhibitors by *in vitro* Translation

This chapter is a reprint of:

Sheridan, C.M., Garcia, V.E., Ahyong, V. DeRisi J.L. The *Plasmodium falciparum* cytoplasmic translation apparatus: a promising therapeutic target not yet exploited by clinically approved anti-malarials. *Malar J* 17, 465 (2018): <https://doi.org/10.1186/s12936-018-2616-7>

Author contributions:

CMS, VA, VEG, and JLD conceived and designed the study, drafted, and revised the paper and its figures. CMS, VEG, and VA performed and analyzed parasite growth experiments. CMS and VEG performed and analyzed S35 incorporation assays. CMS and VA performed and analyzed *in vitro* translation assays. CMS performed and analyzed magnesium assays. All authors read and approved the final manuscript.

Additional/supplemental files that are not figures can be found with the original work

3.1 Abstract

The continued spectra of resistance to existing anti-malarials necessitates the pursuit of novel targets and mechanisms of action for drug development. One class of promising targets consists of the 80S ribosome and its associated components comprising the parasite translational apparatus. Development of translation-targeting therapeutics requires a greater understanding of protein synthesis and its regulation in the malaria parasite. Research in this area has been limited by the lack of appropriate experimental methods, particularly a direct measure of parasite translation. An *in vitro* method directly measuring translation in whole-cell extracts from the malaria parasite *Plasmodium falciparum*, the PfIVT assay, and a historically-utilized indirect measure of translation, S35-radiolabel incorporation, were compared utilizing a large panel of known translation inhibitors as well as anti-malarial drugs. Here, an extensive pharmacologic assessment of the PfIVT assay is presented, using a wide range of known inhibitors demonstrating its utility for studying activity of both ribosomal and non-ribosomal elements directly involved in translation. Further, the superiority of this assay over a historically utilized indirect measure of translation, S35-radiolabel incorporation, is demonstrated. Additionally, the PfIVT assay is utilized to investigate a panel of clinically approved anti-malarial drugs, many with unknown or unclear mechanisms of action, and show that none inhibit translation, reaffirming *Plasmodium* translation to be a viable alternative drug target. Within this set, mefloquine is unambiguously found to lack translation inhibition activity, despite having been recently mischaracterized as a ribosomal inhibitor. This work exploits a direct and reproducible assay for measuring *P. falciparum* translation, demonstrating its value in the continued study of protein synthesis in malaria and its inhibition as a drug target.

3.2 Background

Despite ongoing efforts in its treatment and prevention, malaria remains a severe global health burden, with nearly half the world's population at risk, and incidence of the disease actually increasing in the most recent years for which data are available [1]. Though malaria-related mortality has continued to decrease, the rise in incidence is particularly concerning in light of reduced investment worldwide in combatting malaria, combined with climate change and geopolitical instability that may contribute to a resurgence of the disease [1]. One compounding factor in the battle to eliminate malaria is the persistent emergence of drug resistance in the malaria parasite *Plasmodium falciparum* [1]. As combination therapies are the main defense against resistance, an important focus in therapeutic development is the identification of compounds with unique targets and novel mechanisms of action that are unlikely to be precluded by existing resistance mutations. Medicines for Malaria Venture (MMV) has recently demonstrated the potential of efforts directed at novel targets; two drugs currently showing great promise in clinical trials, SJ733 and cipargamin, inhibit the *P. falciparum* cation ATPase PfATP4, constituting a new class of drug [2-3].

One promising avenue for development of a novel target class is the inhibition of the *P. falciparum* ribosome, as well as other components of the translational machinery responsible for protein synthesis. Translation inhibitors have exhibited great clinical success as potent antibiotics, and in fact, several, including doxycycline and azithromycin, have found additional application as anti-malarials, as they target ribosomes within the malaria parasite's mitochondria and apicoplast, leading to loss of function of these organelles [4-6]. Interestingly, the *P. falciparum* cytoplasmic ribosome appears to occupy an evolutionary middle ground between prokaryotic and eukaryotic, differentiating it sufficiently from human ribosomes to yield a useful

therapeutic window [5]. Indeed, M5717 (previously DDD107498), a potent and highly selective inhibitor of the 80S ribosome interacting protein *P. falciparum* eukaryotic elongation factor 2 (Pfef2), is currently in first-in-human study, validating the potential of the *P. falciparum* translational apparatus as an effective target for anti-malarial drugs of this class [7].

To facilitate the identification of translation inhibitors, a *P. falciparum* whole-cell extract-based *in vitro* translation assay (PfIVT) was developed, and the technique successfully applied to detect small molecule inhibitors in the MMV Malaria Box [8]. More recently, it has been suggested that the widely used drug mefloquine may inhibit the 80S ribosome of *P. falciparum* [9]. In addition, many currently approved anti-malarial compounds lack a definitive mechanism of action, raising the possibility that some of these clinical therapies act through inhibition of translation. The aim of this study was to clarify which compounds truly exhibit inhibitory activity against the *P. falciparum* 80S ribosome and the associated translational apparatus. To do so, a panel of anti-malarial drugs (both clinical and pre-clinical) was compared with well-characterized inhibitors of translation and other defined control compounds in the PfIVT assay, as well as in the S35-radioabel incorporation assay, a historically utilized indirect measure of translation. Importantly, this demonstrated that none of the current clinical therapeutics inhibit translation, including mefloquine. Regardless, testing of tool compounds shows that the PfIVT assay is capable of identifying not only translation inhibitors that directly interact with the ribosome, but also inhibitors of other non-ribosomal components of the translational machinery, demonstrating the broad utility of the assay for identifying novel malaria therapeutics that target *P. falciparum* translation.

3.3 Methods

3.3.1 Drug stocks

In vivo growth and *in vitro* translation measurements were performed using the same drug dilutions. The anti-malarial drugs chloroquine, dihydroartemisinin, lumefantrine, monodesethyl amodiaquine, piperaquine, primaquine, and quinine were a generous gift from Dr. Phil Rosenthal of UCSF. SJ733 was generously provided by Dr. Kip Guy of St. Jude Children's Research Hospital. All other compounds were purchased from the indicated vendors: DDD107498 (Apexbio #A8711-5), mefloquine hydrochloride (Sigma-Aldrich #M2319), emetine (Sigma-Aldrich #E2375), cycloheximide (Fisher #AC35742-0010), MMV008270 (Vitas-M Laboratory #STK591252), actinomycin D (Sigma-Aldrich #A1410), tubercidin (Sigma-Aldrich #T0642), thapsigargin (Sigma-Aldrich #SML1845), ionomycin (Sigma-Aldrich #407951), thiostrepton (Sigma-Aldrich #598226), bruceantin (Toronto Research Chemicals #B689310), verrucarin A (Sigma-Aldrich #V4877), anisomycin (Sigma-Aldrich #A5862), homoharringtonine (Sigma-Aldrich #SML1091), lactimidomycin (EMD Millipore #506291), nagilactone C (BOC Sciences #24338-53-2), suramin sodium salt (Sigma-Aldrich #S2671), puromycin (Thermo Fisher #A1113803), halofuginone (Sigma-Aldrich #32481).

3.3.2 *Plasmodium falciparum* strain and culturing

Plasmodium falciparum W2 (MRA-157) was obtained from MR4. Parasites were grown in human erythrocytes (2% haematocrit) in RPMIc (RPMI 1640 media supplemented with 0.25% Albumax II (GIBCO Life Technologies), 2 g/L sodium bicarbonate, 0.1 mM hypoxanthine, 25 mM HEPES (pH 7.4), and 50 µg/L gentamicin), at 37 °C, 5% O₂, and 5% CO₂. Cells were synchronized with 5% sorbitol treatment for two generations to achieve high synchronicity.

3.3.3 Growth inhibition assays

2 μ L of serial drug dilutions in 100% DMSO were dispensed in triplicate to 96-well plates utilizing the LabCyte ECHO acoustic liquid handler. 198 μ L of *P. falciparum* W2 cultures were added. Growth was initiated with ring-stage parasites at 0.8% parasitaemia and 0.5% haematocrit. Plates were incubated at 37 °C, 5% O₂, and 5% CO₂ for 72 h. Growth was terminated by fixation with 1% formaldehyde, and parasitized cells were stained with 50 nM YOYO-1 (Invitrogen). Parasitaemia was determined by flow cytometry on the BD LSRII, analysed using FlowJo software version 10, and EC₅₀ curves were plotted by GraphPad Prism. Two biological replicates were performed for each drug.

3.3.4 Generation and quality control of extracts for *Plasmodium falciparum* in vitro translation assay

For PfIVT harvests, 1 L of synchronized parasite culture in 2–4% haematocrit was grown in two 500 mL HYPERFlask M vessels (Corning), and media was changed every 8–12 h, with the final media change at 4–8 h prior to harvest. Parasites were harvested in the late trophozoite stage at 15–20% parasitaemia by centrifugation for 5 min at 1500 \times g at room temperature, followed by removal of media and addition of ice-cold 0.025–0.05% final saponin in Buffer A (20 mM HEPES pH 8.0, 2 mM Mg(OAc)₂, 120 mM KOAc). Due to variations between and within lots, saponin stocks were prepared in large volumes, aliquoted, and stored at –20 °C. Percentage utilized for each batch of aliquots was determined empirically through pairwise testing of concentrations (1 for each HYPERFlask) and assessed via resulting activity of PfIVT extracts. Saponin-lysed pellets were centrifuged at 4 °C and 10,000 \times g for 10 min and washed twice with ice-cold Buffer A. Supernatant was carefully removed, and washed pellets were resuspended in an equal volume of Buffer B2 [20 mM HEPES pH8.0, 100 mM KOAc, 0.75 mM

Mg(OAc)₂, 2 mM DTT, 20% glycerol, 1X EDTA-free protease inhibitor cocktail (Roche)], flash frozen, and stored in – 80 °C freezer until the sample was ready to homogenize.

Frozen pellets were thawed on ice and added to a 3-mL Luer lock syringe, which was then secured onto a pre-chilled cell homogenizer containing a 4µm-clearance ball bearing (Isobiotec, Germany) that was pre-washed with ice-cold Buffer B2. Homogenate was passed between two syringes 20 times on ice, either by hand or by use of a custom robot built to accommodate the cell homogenizer [10]. Lysate was immediately centrifuged at 4 °C and 16,000×g for 10 min, and the supernatant (the resulting PfIVT extract) was transferred to a fresh tube, with a small (100 µL) aliquot set aside for activity testing. Extracts and test aliquots were flash-frozen and stored at – 80 °C. Test aliquots from multiple harvests were thawed on ice and tested in batches in the PfIVT assay (see below) across a small range of magnesium concentrations with a 2-h incubation time, using a firefly luciferase reporter. Extracts that surpass the activity threshold of 104 relative luciferase units (RLU) were then thawed on ice and combined to generate large volume pools. Extract pools were flash-frozen in 200 µL aliquots and stored at – 80 °C. Extract pools were tested across a range of magnesium concentrations via PfIVT assay to determine the optimum magnesium concentration. Once magnesium concentration has been determined, pools are then tested in the PfIVT assay in 15 min incubation time points up to 150 min to determine the kinetics of the extract pool, and thus the appropriate incubation time for the pool (~ 75–80% of maximum signal, within the linear range of the extract's kinetic curve). Kinetics must be separately assessed for each reporter used (i.e. if a nanoluciferase reporter is used instead of firefly luciferase).

3.3.5 Magnesium concentration assays

Baseline magnesium levels of the PfIVT extracts were measured using a magnesium-dependent enzyme-based colorimetric assay kit (Sigma-Aldrich #MAK026). Two biological replicates of a dilution series of each extract were tested in duplicate with each of two separate kits, following the protocol provided with the kit. In brief, 10 μ L of each PfIVT extract (neat, or diluted 1:4 or 1:10 with ddH₂O) added to 10 μ L ddH₂O, along with a standard curve, was combined with 50 μ L of master reaction mix (35 μ L magnesium assay buffer, 10 μ L developer, 5 μ L magnesium enzyme mix), and incubated for 10 min with shaking at 37 °C. 450 nm absorbance was read immediately after the initial incubation, and every 5 min thereafter on a Tecan plate reader until the highest A₄₅₀ approached (but did not exceed) 1.5 \times the initial reading. Values were fitted to, and interpolated from, the standard curve using Prism GraphPad.

Plasmodium falciparum in vitro translation assay

Plasmodium falciparum in vitro translation (PfIVT) reactions were carried out in skirted v-bottom 96-well PCR plates (BioRad) and sealed with adhesive aluminum foil plate seals (Beckman Coulter, Indianapolis, IN, USA). 200 nL of drug in 100% DMSO was dispensed in duplicate to appropriate wells of the plate utilizing a Labcyte ECHO acoustic liquid handler. 19.8 μ L of PfIVT reaction mix (per 20 μ L: 14 μ L extract, 1 μ g T7-transcribed firefly luciferase mRNA, 10 μ M amino acid mixture, 20 mM HEPES/KOH pH 8.0, 75 mM KOAc, 2 mM DTT, 0.5 mM ATP, 0.1 mM GTP, 20 mM creatine phosphate, 0.2 μ g/ μ L creatine kinase, and the appropriate amount of Mg(OAc)₂ as determined for the particular pool of extract) was then dispensed to each well using Rainin E4 12-channel electronic pipettes (Rainin Instruments, Oakland, CA, USA). Reactions were incubated at 37 °C for the appropriate amount of time as determined for the particular pool of extract. After incubation, the reactions were placed on ice,

then quenched through transfer to a 96-well LUMITRAC 200 flat-bottom white assay plate (Greiner Bio-One, Monroe, NC, USA) containing 2 μ L of 50 μ M cycloheximide (dispensed using the Labcyte ECHO), then immediately centrifuged to combine the PflVT reaction with the cycloheximide for a final concentration of 5 μ M cycloheximide. Reactions were assayed using the Promega GloMax-Multi + microplate reader with a three-second delay and three-second integration after addition of 200 μ L luciferin reagent dispensed at a speed of 200 μ L/second (firefly luciferin reagent: 20 mM Tricine, 2.67 mM MgSO₄ \times 7H₂O, 0.1 mM EDTA, 33.3 mM DTT, 530 μ M ATP, 270 μ M Acetyl CoEnzyme A, 1 mM D-Luciferin, 265 μ M Magnesium Carbonate Hydroxide, pH 8.15). Three biological replicates were performed in duplicate for each drug. IC₅₀ curves were plotted by GraphPad Prism.

Rabbit reticulocyte *in vitro* translation assay

Rabbit reticulocyte *in vitro* translation assays were performed as described in Ahyong et al. [8] with the exception that the final [DMSO] for MMV008270 was 2.5% and all other final [DMSO] = 0.55% IC₅₀ curves were plotted by GraphPad Prism.

3.3.6 S35 incorporation assay

3.3.6.1 Parasite purification

Synchronized parasites were cultured in 2% haematocrit at 10–15% parasitaemia, and MACS purified at the late trophozoite stage to remove uninfected erythrocytes using standard protocols. In brief, at least two LD MACS Separation columns (Miltenyi Biotec) per 50 mL of culture were washed with 1.25 mL of pre-warmed RPMIc. Next, cultures were added to the columns 5 mL at a time and allowed to gravity filter at 37 °C. Finally, the columns were rinsed with 2.5 mL of pre-warmed RPMIc, removed from the magnetic stand, and eluted with 2 mL of pre-warmed RPMIc.

3.3.6.2 Drug treatment and S35 labelling

1 μL of drug in 100% DMSO was dispensed to each well of a 96-well round-bottom culture plate utilizing the Labcyte ECHO acoustic liquid handler. 2×10^7 MACS-purified parasites in 199 μL of RPMIc were then added to each well. Parasites were incubated with drug for 2 h at 37 °C, 5% CO₂, 5% O₂. Next, samples were transferred from 96-well plates to 1.5 mL screw-cap microfuge tubes. 35 μCi of EasyTag™ Express S35 Protein Labeling Mix (Perkin Elmer) diluted to 10 μL with RPMIc was added to each tube. Reactions were incubated at 37 °C with mild shaking for 2 h.

3.3.6.3 Washing and lysis

After incubation, cells were pelleted and 160 μL of supernatant was removed. Parasites were then washed with 200 μL of ice-cold PBS containing 50 μM cycloheximide four times. After the final wash, all supernatant was removed and samples were resuspended in 15 μL of 2X SDS buffer (100 mM Tris–Cl pH 6.8, 4% SDS, 20% glycerol, 0.1 M DTT). Samples were boiled at 98 °C for 5 min and stored at –20 °C.

3.3.6.4 Scintillation counting

Samples were thawed at room temperature, boiled for 5 min at 98 °C, and spun at max speed in a tabletop microcentrifuge for 10 min. 10 μL of supernatant per sample was placed on a 0.45 μm nitrocellulose membrane (HAWP02400 from Millipore). Each membrane was washed 4 times with 15 mL of TBS-T then placed in a 20 mL HDPE scintillation vial (Fisher Scientific) with 8 mL of Ecoscint A (National Diagnostics). S35 counts were measured for 1 min using a Beckmann coulter, LS 6500 Multi-purpose Scintillation Counter. Three biological replicates were performed for each drug.

3.3.6.5 Mefloquine solubility assay

PfIVT extracts were incubated with a dilution series of mefloquine or DMSO control for 90 min. All PfIVT conditions were the same as above, except without addition of cycloheximide to stop translation. Reactions were centrifuged at $16,100\times g$ for 10 min at room temperature; resulting supernatant was then filtered and added to cultures for the *P. falciparum* growth inhibition assays as described above.

3.4 Results

3.4.1 Extract optimization for the Plasmodium falciparum in vitro translation assay

To ensure reproducible consistency and robustness of the *P. falciparum in vitro* translation (PfIVT) assay, extensive validation of parasite extracts was performed. A detailed, step-by-step protocol is presented in the Additional files 1, 2, 3, 4 and 5. Only those extracts surpassing a rigorous activity threshold were utilized for the PfIVT assay, and extracts from individual harvests meeting this criterion were combined to generate large pools for use across many assays. Ribosome activity is especially sensitive to divalent cations, in particular magnesium concentration [11]. Therefore, the magnesium concentration of each PfIVT extract was measured, followed by determination of the optimal amount of magnesium required by each extract in order to achieve maximal activity. Post-harvest magnesium concentrations were typically less than 2 mM, whereas the maximum translational activity corresponded to a final PfIVT reaction concentration of approximately 4 mM magnesium (Figure 3.1a and 3.1b). Upon determining optimal magnesium conditions for each pool of extract, kinetic curves were generated with 15-min increments to establish the ideal incubation time for the assay (Figure 3.1c). This was necessary, since assay kinetics varied between extracts. Note that separate kinetic curves must also be established for the particular reporter utilized (in this case, firefly luciferase).

To maintain maximal sensitivity to inhibitors and linearity of the assay, PfIVT experiments were conducted at the time point corresponding to 75–80% of the saturation signal (Figure 3.1c).

3.4.2 Probing different stages of translation in a Plasmodium falciparum cellular extract system using tool compounds

The process of translation may be binned into three main stages: initiation, elongation, and termination [12, 13]. In eukaryotes, this process is carried out by the 80S ribosome, comprised of a small (40S) and large (60S) subunit [12-13]. To further validate the PfIVT assay and investigate its capacity to interrogate the entirety of the normal activity of the 80S ribosome (and thus identify drugs inhibiting all steps of the process of translation), an extensive panel of previously characterized translational inhibitors was tested, both in the PfIVT assay, as well as in the historically utilized S35-radiolabelled amino acid incorporation assay. In contrast to the PfIVT assay, which directly measures activity of the 80S ribosome and the associated translational apparatus, S35 incorporation is an indirect measure of translation, and, as such, is affected by upstream and parallel pathways not directly involved in ribosomal activity. For instance, the S35 incorporation assay is impacted by changes in cell viability, stress or other responses that alter proteostasis, and even changes to cellular import mechanisms or integrity of the parasite membrane, as the assay requires exogenous addition of radiolabelled amino acid. Despite the resulting ambiguity and often misleading nature of results generated, S35 incorporation has remained a commonly used assay for studying parasite translation in the absence of a better alternative [9].

Commercially available compounds that directly interact with the eukaryotic ribosome to inhibit translation initiation and/or elongation via a variety of mechanisms and binding sites, as well as several inhibitors of translation known to act upon non-ribosomal components of the

translational machinery were tested (Tables 3.1 and 3.2). The eukaryote-specific inhibitors bruceantin and verrucarin A inhibit translation initiation by blocking initial peptide-bond formation through binding of mutually exclusive sites (with bruceantin binding the A-site and verrucarin binding between the P- and A-sites) [13-17]. Suramin, also a specific inhibitor of the eukaryotic ribosome, inhibits both initiation and elongation through binding of multiple sites on the 40S, 60S and 80S ribosomes [18]. The eukaryote-specific elongation inhibitors tested are also distinct in their activities: cycloheximide and lactimidomycin overlap in their binding of the ribosome A-site, but differences in size and side-chains yield unique effects; anisomycin also overlaps cycloheximide's binding site, but the two drugs bind the ribosome in distinct rotational conformations at different steps of elongation; homoharringtonine binds the A-site, but specifically inhibits re-initiating ribosomes; and nagilactone C inhibits both eEF-1 α -dependent aminoacyl-tRNA loading and peptidyl transferase activity [13, 14, 19-21]. Halofuginone, also a specific inhibitor of eukaryote translation, does not interact with the ribosome, but instead inhibits glutamyl-prolyl-tRNA synthetase [22]. Puromycin was the sole pan-inhibitor tested, and acts as a tRNA mimetic that is incorporated into the nascent polypeptide chain, leading to its premature termination [23-24]. Negative controls were thiostrepton, a specific inhibitor of prokaryotic translation initiation and elongation; actinomycin D, an inhibitor of RNA polymerase II; tubercidin, an adenosine mimetic; and thapsigargin, a sarco/endoplasmic reticulum ATPase (SERCA) inhibitor [25-34].

After determining the EC₅₀ of each drug for the *P. falciparum* W2 strain in a 72-h parasite growth assay, the drugs were characterized in both the S35 incorporation and PfIVT assays (Table 3) (Figs. 2 and 3). Drugs were tested in the S35 and PfIVT assays at 0.1-, 1-, 10-, and 100-fold their determined growth assay EC₅₀ in W2 parasites, except in cases where the

highest concentration was constrained by solubility or available stock solution. The translation initiation inhibitors bruceantin and verrucarin A were both potent (nanomolar) inhibitors of S35 incorporation and PfIVT (Figure 3.2). All translation elongation inhibitors (anisomycin, cycloheximide, homoharringtonine, lactimidomycin, and nagilactone C) also strongly inhibited both S35 incorporation and PfIVT (Figure 3.2). Cycloheximide was additionally tested at 1000-fold its EC50, as it did not inhibit S35 incorporation at the lower concentrations tested, but did at this higher concentration, in line with inhibitory concentrations in recent reports, which also show that significantly higher concentrations of cycloheximide are required for complete, measurable inhibition of translation than for rapid and total parasite killing *in vivo* (Additional file 6) [8-9, 35]. Suramin, which has been shown to inhibit both translation initiation and elongation, robustly inhibited PfIVT, but not S35 incorporation, likely due to poor cell permeability and the short timeframe of the S35 assay (2-h drug pre-incubation followed by 2-h radiolabel incorporation) (Figure 3.2). The tRNA mimetic puromycin, which induces premature termination of nascent polypeptides, inhibited both S35 incorporation and PfIVT with similar efficacy (Figure 3.2). Elucidating an even greater range of utility for the PfIVT assay, it was shown to be capable of identifying inhibitors of non-ribosomal components of translation. The glutamyl-prolyl-tRNA synthetase inhibitor halofuginone inhibits both S35 incorporation and the PfIVT assay (Figure 3.2). In sum, these data demonstrate the ability of the PfIVT assay to interrogate both direct ribosomal activity, as well as extra-ribosomal components of the translational machinery.

3.4.3 The Plasmodium falciparum in vitro translation assay measures activity of cytoplasmic ribosomes

Importantly, all of the eukaryotic ribosome-specific inhibitors, which therefore should inhibit only *P. falciparum* cytoplasmic and not apicoplast or mitochondrial ribosomes, displayed inhibition in the PfIVT assay, with several achieving complete or near complete blocking of translation (suramin, anisomycin, lactimidomycin, nagilactone C) (Figure 3.2). In addition, the prokaryotic ribosome-specific inhibitor thiostrepton did not inhibit the PfIVT assay at any concentration tested, despite inhibiting the S35 assay at concentrations above its determined EC50 (Figure 3.3). Thiostrepton is known to have multiple targets apart from ribosomes in eukaryotes and has been shown to induce an ER stress response with a phenotype similar to thapsigargin, which likely accounts for its activity in the S35 assay [36-38].

3.4.4 The S35 incorporation assay is not a reliable indicator of direct translation inhibition

Although it is well documented in other model systems (i.e. yeast) that the S35-radiolabelled amino acid incorporation assay is an indirect measure of translation and can, as such, generate many misleading artifacts, this has not yet been characterized carefully with respect to Plasmodium spp. [39-40]. Despite this, several studies in Plasmodium have relied on this indirect measure as a primary readout of translation [9, 41]. To address this and further determine the specificity of the PfIVT assay relative to the S35 uptake assay, a panel of small molecules that are known to inhibit cellular processes other than translation were tested (Tables 3.2 and 3.3). Not surprisingly, actinomycin D, an inhibitor of transcription targeting RNA Polymerase II, and the SERCA inhibitor thapsigargin both exhibited strong inhibition in the S35 incorporation assay, but had no effect in the PfIVT assay (Figure 3.3). Tubercidin, an adenosine mimetic, had a modest inhibitory effect on S35 incorporation, but, again, negligible effect in the

PfIVT assay (Figure 3.3). These data confirm that the PfIVT assay directly measures translation, and highlight the lack of translation specificity of the S35 incorporation assay.

3.4.5 Analysis of clinically-approved anti-malarials reveals that none, including mefloquine, inhibit the 80S ribosome

Next, a panel of clinically approved anti-malarial drugs with undefined or disputed mechanisms of action was tested, to determine whether any might act through direct inhibition of translation, subjecting these drugs to the same battery of assays described above (*P. falciparum* growth, PfIVT, and S-35 incorporation) (Table 3.3). Chloroquine and piperazine were mild inhibitors of the S35 incorporation assay at the highest drug concentrations tested (Figure 3.4). Quinine, lumefantrine, primaquine, monodesethyl amodiaquine (the active metabolite of amodiaquine), and dihydroartemisinin were moderate-to-strong inhibitors of the S35 incorporation assay (Figure 3.4). SJ733, an inhibitor of the sodium transporter PfATP4, and a clinical candidate currently in Phase I trials, exhibited strong inhibition in the S35 incorporation assay (Figure 3.4). Notably, none of these anti-malarial drugs inhibited the PfIVT assay. However, primaquine cannot be ruled out with complete certainty as an inhibitor of translation, as its active metabolite may not be produced in an *in vitro* setting, and it does show moderate activity in the S35 incorporation assay [42]. Also included were several drugs (clinical and pre-clinical) that have recently been reported to inhibit translation (Table 3.3) [7-9]. MMV008270 was a moderate inhibitor of the S35 incorporation assay, while mefloquine and DDD107498 robustly inhibited S35 incorporation (Figure 3.4). Strikingly, while DDD107498 and MMV008270 inhibited the PfIVT assay, mefloquine failed to do so (Figure 3.4). Interestingly, MMV008270 was an exceptionally effective inhibitor of translation in the PfIVT assay at all concentrations tested (Figure 3.4). These data reveal that mefloquine has recently been

mischaracterized as a ribosome inhibitor through use of the S35 incorporation assay, when it does not, in fact, directly inhibit translation [9].

To further validate the PfIVT data regarding mefloquine, the PfIVT assay was repeated, alongside a commercially available rabbit reticulocyte *in vitro* translation assay (RRIVT), with a full titration of drug to determine half maximal effective values for both mefloquine and DDD107498 (Figure 3.5). As expected, the positive control cycloheximide was a robust inhibitor of both translation systems (PfIVT IC₅₀: 31.91 nM, RRIVT IC₅₀: 37.8 nM), while DDD107498 was a potent inhibitor of *P. falciparum*, but not rabbit reticulocyte translation, confirming the reported high *P. falciparum* selectivity of DDD107498 (PfIVT IC₅₀: 60.5 nM) (Figure 3.5). In contrast, mefloquine failed to inhibit in either the PfIVT or RRIVT assay, even at concentrations as high as 20 μM (Figure 3.5). The reported binding site of mefloquine to the 80S ribosome is on the highly conserved ribosomal protein uL13; if this were indeed the active binding site of the drug, mefloquine should inhibit the RRIVT assay [43]. To rule out the possibility that mefloquine solubility may be a confounding factor in the IVT assays, completed PfIVT reactions with a dilution series of mefloquine or DMSO control were centrifuged at high speed, sterile-filtered, and the resulting supernatant was used as the input for an *in vivo* growth assay. EC₅₀ values were comparable between the IVT reaction supernatant containing mefloquine (12.31 nM) and mefloquine alone (4.17 nM), thus demonstrating that mefloquine is soluble in the PfIVT assay (Additional file 7). These data make clear that mefloquine does not act through inhibition of the *P. falciparum* ribosome, nor through other direct inhibition of the translational machinery.

3.5 Discussion

This work presents an extensive dissection and validation of the whole-cell extract-derived PfIVT assay, the only reported direct measure of *P. falciparum* translation to date. Through

probing the assay with numerous small molecule inhibitors of translation, exhibiting a diversity of binding sites and mechanisms of action, as well as a variety of well-characterized tool compounds inhibiting non-translational pathways, it is demonstrated that the PfIVT assay specifically measures *P. falciparum* cytoplasmic ribosome activity. *In vitro* translation extracts are inherently difficult to make, and even more so for an intraerythrocytic parasite. However, when subjected to stringent quality control and careful optimization, the PfIVT assay reliably and specifically identifies inhibitors of translation initiation and elongation, as well as inhibitors of non-ribosomal proteins necessary for translation, such as tRNA synthetase.

The PfIVT assay is particularly valuable to the study of *P. falciparum* translation as a direct measure of translation, as opposed to the indirect measures to which the field has historically been constrained, such as incorporation of radiolabelled amino acids *in vivo*. Importantly, these data show the PfIVT assay is significantly more specific, and in some cases more sensitive, than S35-radiolabel incorporation in identifying small molecule inhibitors of translation. Indeed, the PfIVT assay specifically identified all eukaryotic translation inhibitors tested, while S35-radiolabel incorporation was prone to false-positives. This work shows that none of the clinically approved anti-malarials tested are inhibitors of translation, emphasizing the potential for translation as a useful therapeutic target, as there is unlikely to be pre-existing mechanism-specific resistance to any identified candidates resulting from use of these drugs. It is notable that mefloquine, in contrast to other previously reported translation inhibitors, did not exhibit any inhibitory activity. Mefloquine was likely mischaracterized as an 80S ribosome inhibitor through a combination of non-specific inhibition of S35 incorporation, as well as artifacts arising from cryo-EM structures obtained under the non-physiologic condition of 10 mM magnesium—well above the ~ 4 mM magnesium found herein to be optimal for translation,

as well as the physiologic magnesium concentrations noted in other eukaryotes and *E. coli* (Figure 3.1) [9, 44-46].

While the PfIVT assay exhibits clear benefits over existing methodologies for the study of *P. falciparum* translation, it is acknowledged that the technique has several limitations. As is the case with *in vitro* translation systems in other organisms, the current assay is likely biased toward the study of non-cap-dependent initiation and elongation. Uncapped mRNA were utilized in this study to focus specifically on activity of the 80S ribosome itself, rather than the cap-recognition apparatus. It is possible that utilization of capped mRNA in future studies would facilitate interrogation of cap-dependent translation initiation. Likewise, there are few characterized pharmacologic inhibitors of eukaryotic translation termination, none of which are currently commercially available; thus, the PfIVT system, as described, may not be sensitive to all specific inhibitors of translation termination. Additionally, some translation inhibitors, such as homoharringtonine, demonstrated greater potency in the S35 incorporation and growth inhibition assays than in PfIVT. Such variation between the two assays may suggest off-target effects of these drugs, or differences between whole living cells and cellular extracts.

3.6 Conclusions

Determining the true molecular targets of anti-malarials is critical to improved therapeutic development. Exploiting differences between *P. falciparum* and mammalian ribosomes remains a promising avenue, as evidenced by the potent and discriminating drug DDD107498. Here, it is shown that orthogonal biochemical assays may be used to test hypotheses generated by structural data and cell-based assessments. This investigation of mefloquine reaffirms that direct functional measurements of drug activity are critical to identifying the genuine molecular targets of drugs. Importantly, this work demonstrates that the

PfIVT assay is a uniquely direct measure of *P. falciparum* translation that can be used to facilitate a better understanding of the specifics of *P. falciparum* protein synthesis, with potentially great consequences for anti-malarial therapeutic development.

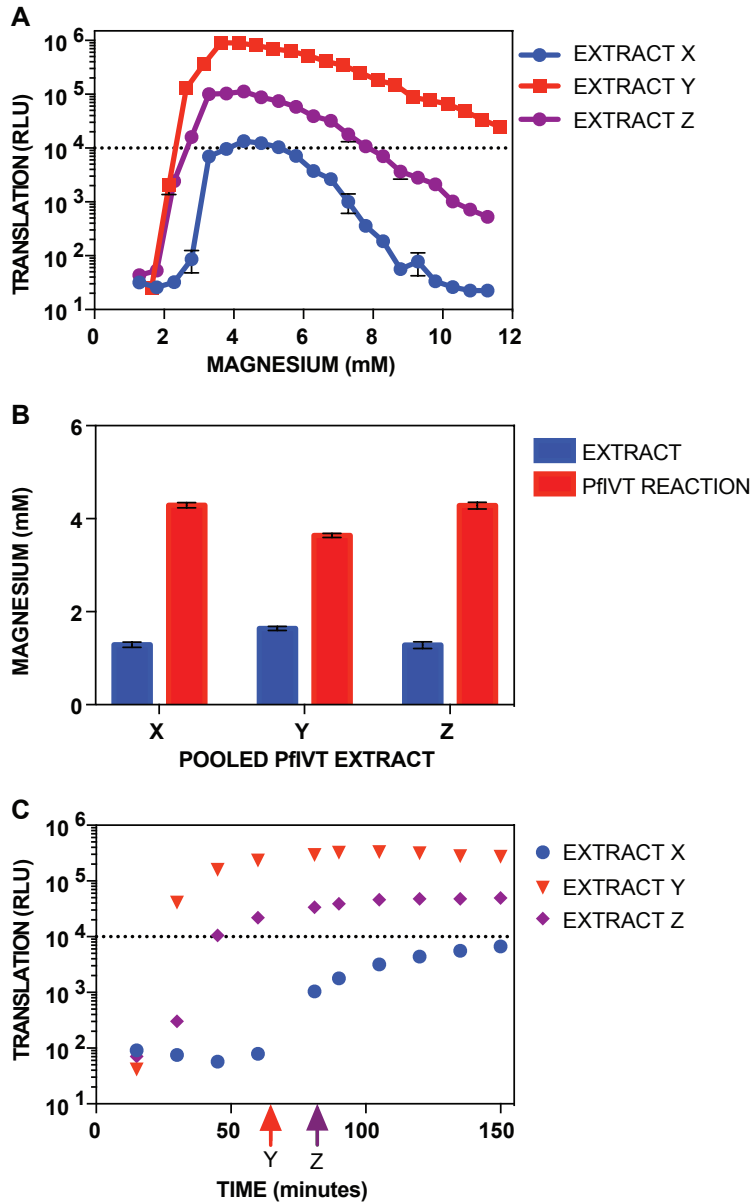


Figure 3.1 Optimization and quality control parameters of PfIVT extracts

a) Translational activity of 3 representative extracts (X, Y, and Z) over a range of reaction magnesium concentrations. b) Measured basal extract magnesium concentration (blue bars) and optimum translation reaction magnesium concentration (red bars) for each of 3 representative PfIVT extracts (X, Y, and Z). c) Kinetic curves for translational activity of each of 3 representative PfIVT extracts (X, Y, and Z) at the optimum reaction magnesium concentration shown in part B. Arrows indicate the timepoint to use for inhibition assays in the extracts meeting the activity threshold, indicating ~75% of saturation signal. The dashed line at 104 relative luciferase units (RLU) represents the cutoff for acceptable translational activity for the assay. Extract X does not consistently meet the 104 RLU activity threshold and would not be used for PfIVT assays

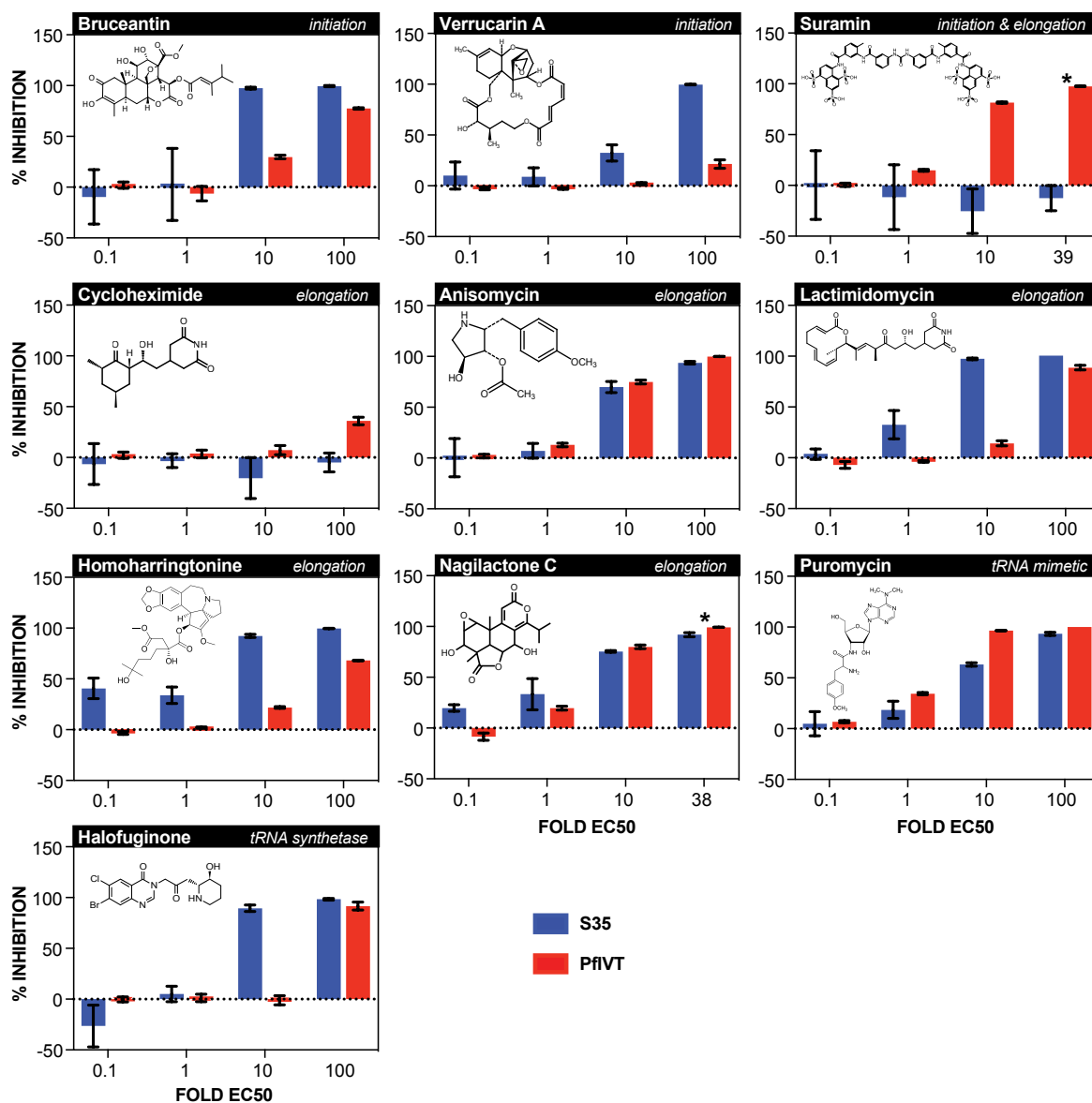


Figure 3.2 Dose-dependent inhibition of S35 incorporation and PflVT assays by eukaryotic translation inhibitors

Dose-dependent inhibition, calculated as % inhibition, of S35 incorporation (blue bars) and PflVT assays (red bars). Name of compound, mechanism of action, and molecular structure are displayed at top of each graph. Compounds were tested at 0.1-, 1-, 10-, and 100-fold the EC50 calculated in *in vivo* growth inhibition assay, except where upper concentration was limited by solubility, indicated by *

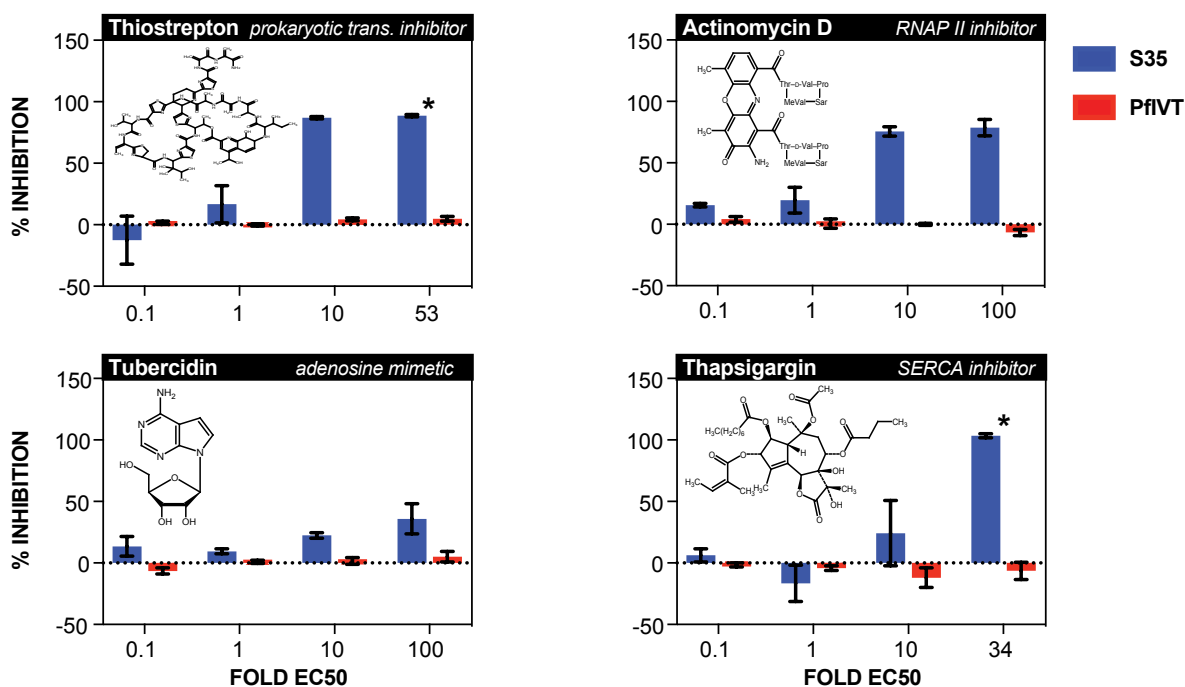


Figure 3.3 Dose-dependent inhibition of S35 incorporation and PfIVT assays by negative control compounds

Dose-dependent inhibition, calculated as % inhibition, of S35 incorporation (blue bars) and PfIVT assays (red bars) by negative control compounds: prokaryotic translation inhibitor and inhibitors of other (non-translation) cellular processes. Name of compound, mechanism of action, and molecular structure are displayed at top of each graph. Compounds were tested at 0.1-, 1-, 10-, and 100-fold the calculated EC50 calculated in *in vivo* growth inhibition assay, except where upper concentration was limited by solubility, indicated by *

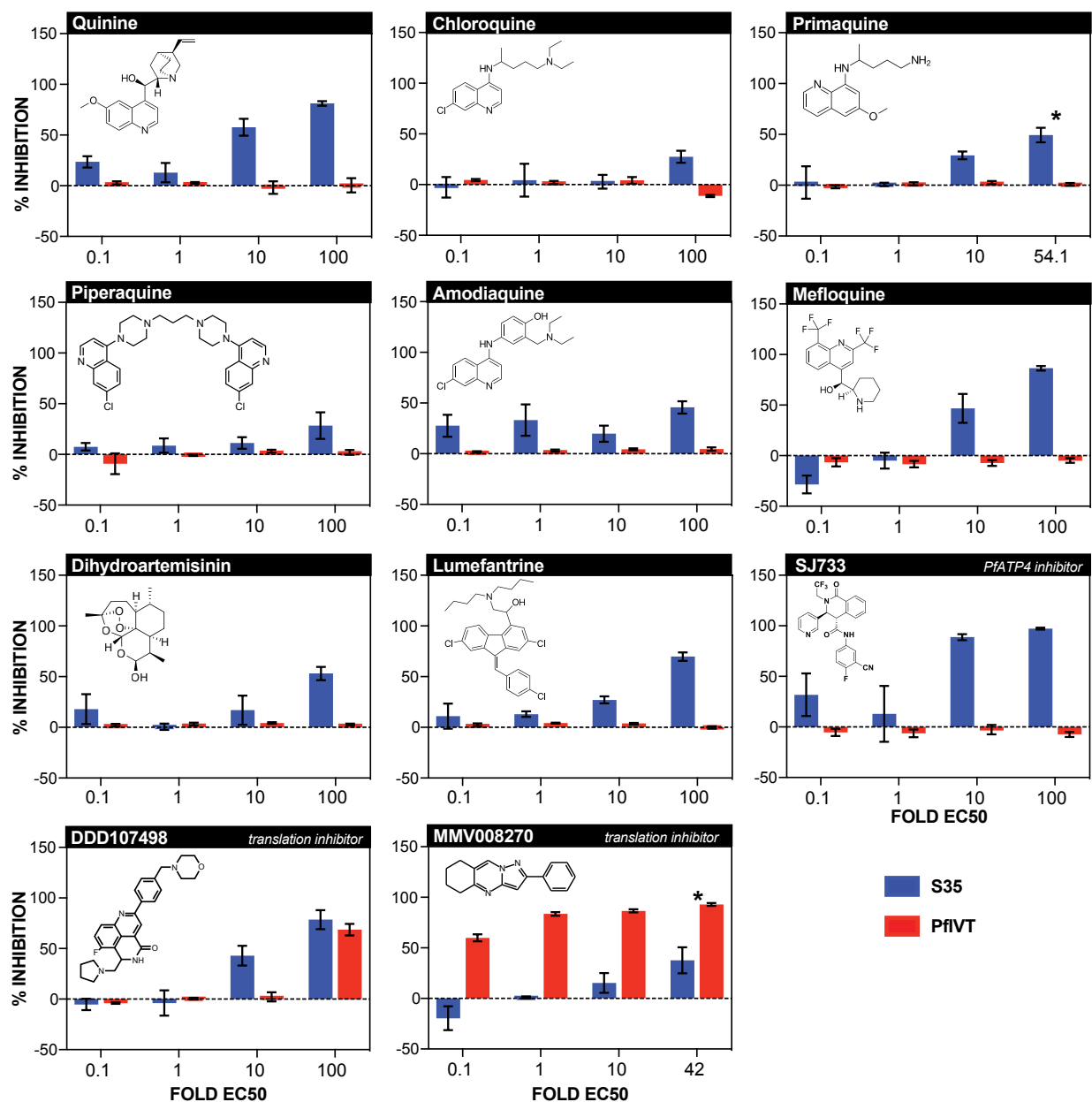


Figure 3.4 Dose-dependent inhibition of S35 incorporation and PfIVT assays by antimalarial compounds

Dose-dependent inhibition, calculated as % inhibition, of S35 incorporation (blue bars) and PfIVT assays (red bars) by pre-clinical and clinically-approved antimalarial compounds. Name of compound, mechanism of action (where definitively known), and molecular structure are displayed at top of each graph. Compounds were tested at 0.1-, 1-, 10-, and 100-fold the calculated EC₅₀ calculated in *in vivo* growth inhibition assay, except where upper concentration was limited by solubility, indicated by *

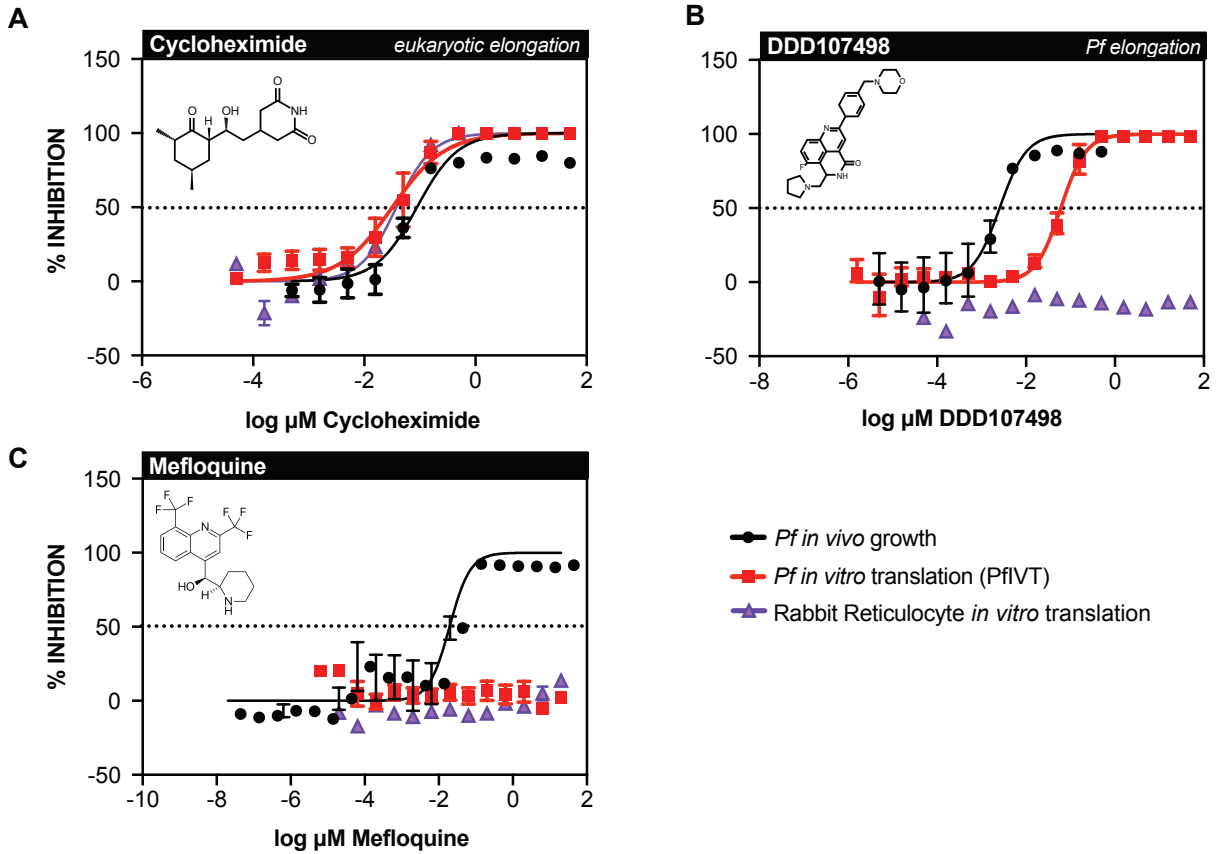
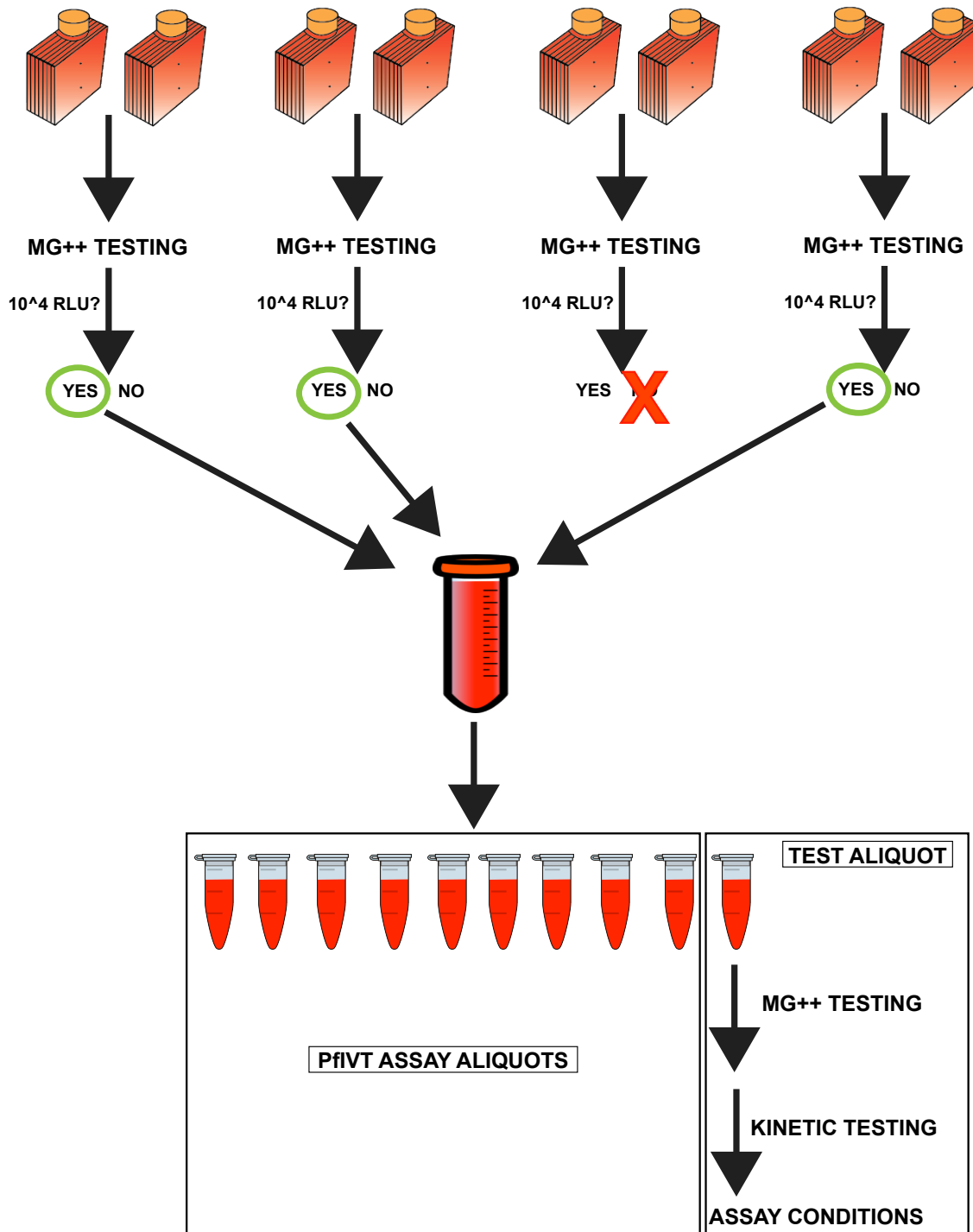
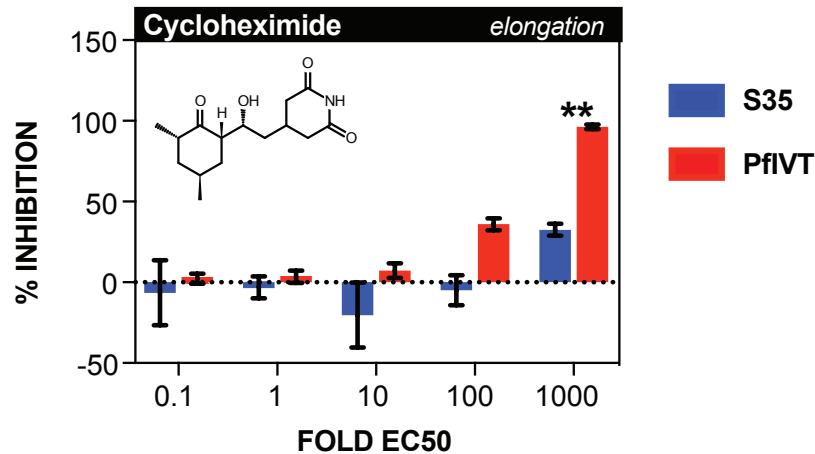


Figure 3.5 Dose-response curves of *Pf* growth, PflVT, and RRIVT for mefloquine and controls

Dose-response curves comparing inhibition, calculated as % inhibition, of *P. falciparum* growth assay (black), *P. falciparum* *in vitro* translation assay (red), and commercially available rabbit reticulocyte *in vitro* translation assay (purple) for a cycloheximide, b DDD107498 (M5717), and mefloquine. Name of compound, mechanism of action (where definitively known), and molecular structure are displayed at top of each graph

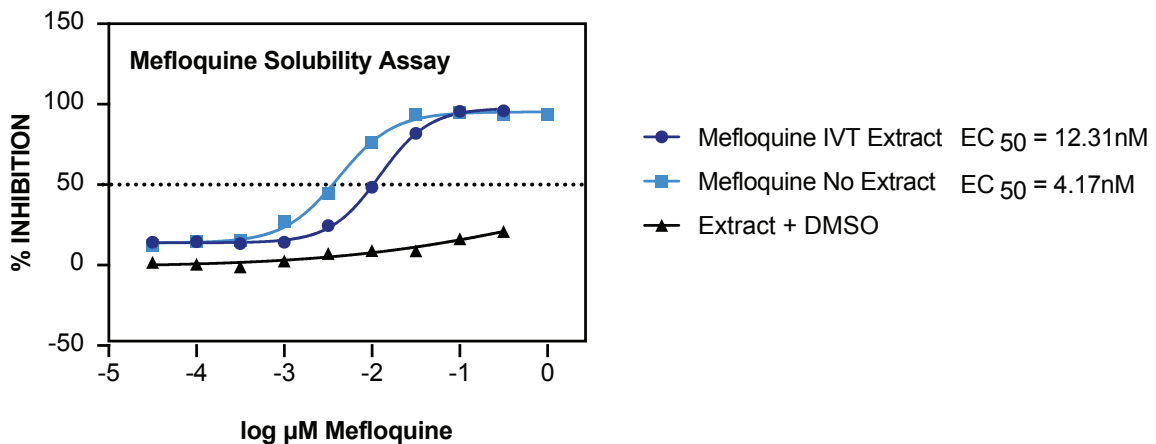


Additional file 3.4 Flowchart for PfIVT extract quality control and pooling Individual harvests are first tested at different magnesium concentrations; those that achieve 10^4 RLU activity threshold are pooled. Pooled extract is aliquoted, and a test aliquot is utilized to first determine ideal magnesium concentration, then ideal incubation time. Remaining aliquots are utilized for PfIVT assays at the determined magnesium & kinetic conditions.



Additional file 3.6 Dose-dependent inhibition of S35 incorporation and PfIVT assays by cycloheximide

Dose-dependent inhibition of S35 incorporation (blue bars) and PfIVT assays (red bars) by the translation inhibitor cycloheximide, tested up to 1000-fold (**) the EC₅₀ calculated in *P. falciparum* growth inhibition assay.



Additional file 3.7 Mefloquine solubility assay

Dose-dependent inhibition of *P. falciparum* *in vivo* growth by mefloquine in PfIVT extract post-PfIVT reaction (Mefloquine IVT Extract), mefloquine alone (Mefloquine No Extract), or DMSO control in PfIVT extract post-PfIVT reaction (Extract + DMSO).

Table 3.1. Mechanism of action and species specificity of translation inhibitors.

COMPOUND	SPECIFICITY	MECHANISM OF ACTION	REFERENCE
bruceantin	eukaryotic (<i>Pf</i> cytoplasmic ribosomes)	inhibits initiation	[16,17]
verrucarin A	eukaryotic (<i>Pf</i> cytoplasmic ribosomes)	inhibits initiation, binds between P- & A- sites	[12–14]
suramin	eukaryotic (<i>Pf</i> cytoplasmic ribosomes)	inhibits initiation & elongation, multiple binding sites	[16]
anisomycin	eukaryotic (<i>Pf</i> cytoplasmic ribosomes)	inhibits elongation, binds A-site	[12,17]
cycloheximide	eukaryotic (<i>Pf</i> cytoplasmic ribosomes)	inhibits elongation, binds E-site	[12]
homoharringtonine	eukaryotic (<i>Pf</i> cytoplasmic ribosomes)	inhibits elongation on re-initiating ribosomes, binds A-site	[12,18]
lactimidomycin	eukaryotic (<i>Pf</i> cytoplasmic ribosomes)	inhibits elongation, binds E-site	[12]
nagilactone C	eukaryotic (<i>Pf</i> cytoplasmic ribosomes)	inhibits elongation, binds A-site	[12,19]
puromycin	pan-inhibitor	tRNA mimetic	[21,22]
halofuginone	eukaryotic	inhibits glutamyl-prolyl-tRNA synthetase	[20]
thiostrepton	prokaryotic (<i>Pf</i> mitochondrial & apicoplast ribosomes)	inhibits initiation & elongation	[23–29]

Table 3.2. Mechanism of action of non-translation inhibitors.

COMPOUND	MECHANISM OF ACTION	REFERENCE
actinomycin D	RNA polymerase II inhibitor	[30]
tubercidin	adenosine mimetic	[31]
thapsigargin	SERCA inhibitor	[32–34]

Table 3.3. Half-maximal effective concentrations (nM) determined in *P. falciparum* growth inhibition assay

TEST COMPOUNDS	72H GROWTH INHIBITION EC50 (nM)	ANTIMALARIALS	72H GROWTH INHIBITION EC50 (nM)
bruceantin	4.2	MMV008270	2400
verrucarin A	0.6	SJ733	60
suramin	1819	M5717 (DDD107498)	1
anisomycin	39	quinine	370
cycloheximide	0.6	chloroquine	333
homoharringtonine	6.8	mefloquine	25
lactimidomycin	22	piperaquine	26
nagilactone C	1310	primaquine	1849
puromycin	52	monodesethyl amodiaquine ^a	61
halofuginone	2	lumefantrine	4
thiostrepton	942	dihydroartemisinin	3
actinomycin D	10		
tubercidin	168		
thapsigargin	2900		

^a Active metabolite of amodiaquine

Chapter 3 References

1. World malaria report 2017. (2017).
2. White, N. J. *et al.* Spiroindolone KAE609 for Falciparum and Vivax Malaria. *N. Engl. J. Med.* **371**, 403–410 (2014).
3. Jiménez-Díaz, M. B. *et al.* (+)-SJ733, a clinical candidate for malaria that acts through ATP4 to induce rapid host-mediated clearance of Plasmodium. *Proc. Natl. Acad. Sci. U. S. A.* **111**, E5455–E5462 (2014).
4. Rosenthal, P. J. Azithromycin for Malaria? *Am. J. Trop. Med. Hyg.* **95**, 2–4 (2016).
5. Budimulja, A. S., Syafruddin, Tapchaisri, P., Wilairat, P. & Marzuki, S. The sensitivity of Plasmodium protein synthesis to prokaryotic ribosomal inhibitors. *Mol. Biochem. Parasitol.* **84**, 137–141 (1997).
6. Dahl, E. L. *et al.* Tetracyclines Specifically Target the Apicoplast of the Malaria Parasite *Plasmodium falciparum*. *Antimicrob. Agents Chemother.* **50**, 3124–3131 (2006).
7. Baragaña, B. *et al.* A novel multiple-stage antimalarial agent that inhibits protein synthesis. *Nature* **522**, 315–320 (2015).
8. Ahyong, V. *et al.* Identification of *Plasmodium falciparum* specific translation inhibitors from the MMV Malaria Box using a high throughput *in vitro* translation screen. *Malar. J.* **15**, (2016).
9. Wong, W. *et al.* The antimalarial Mefloquine targets the *Plasmodium falciparum* 80S ribosome to inhibit protein synthesis. *Nat. Microbiol.* **2**, 17031 (2017).
10. Garcia, V. E., Liu, J. & DeRisi, J. Low-Cost Touchscreen Driven Programmable Dual Syringe Pump for Life Science Applications. *HardwareX* **4**, e00027 (2018).

11. Bashan, A. & Yonath, A. The linkage between ribosomal crystallography, metal ions, heteropolytungstates and functional flexibility. *J. Mol. Struct.* **890**, 289–294 (2008).
12. Jackson, R. J., Hellen, C. U. T. & Pestova, T. V. The mechanism of eukaryotic translation initiation and principles of its regulation. *Nat. Rev. Mol. Cell Biol.* **11**, 113–127 (2010).
13. Loubresse, N. G. *et al.* Structural basis for the inhibition of the eukaryotic ribosome. *Nature* **513**, 517–522 (2014).
14. Cannon, M., Jimenez, A. & Vazquez, D. Competition between trichodermin and several other sesquiterpene antibiotics for binding to their receptor site(s) on eukaryotic ribosomes. *Biochem. J.* **160**, 137–145 (1976).
15. Carrasco, L., Fernandez-Puentes, C. & Vazquez, D. Antibiotics and compounds affecting translation by eukaryotic ribosomes. Specific enhancement of aminoacyl-tRNA binding by methylxanthines. *Mol. Cell. Biochem.* **10**, 97–122 (1976).
16. Liao, L. L., Kupchan, S. M. & Horwitz, S. B. Mode of action of the antitumor compound bruceantin, an inhibitor of protein synthesis. *Mol. Pharmacol.* **12**, 167–176 (1976).
17. Gürel, G., Blaha, G., Moore, P. B. & Steitz, T. A. U2504 determines the species specificity of the A-site cleft antibiotics: the structures of tiamulin, homoharringtonine, and bruceantin bound to the ribosome. *J. Mol. Biol.* **389**, 146–156 (2009).
18. Brigotti, M., Alfieri, R. R., Petronini, P. G. & Carnicelli, D. Inhibition by suramin of protein synthesis *in vitro*. Ribosomes as the target of the drug. *Biochimie* **88**, 497–503 (2006).
19. Lareau, L. F., Hite, D. H., Hogan, G. J. & Brown, P. O. Distinct stages of the translation elongation cycle revealed by sequencing ribosome-protected mRNA fragments. *eLife* **3**, (2014).

20. Fresno, M., Jiménez, A. & Vázquez, D. Inhibition of translation in eukaryotic systems by harringtonine. *Eur. J. Biochem.* **72**, 323–330 (1977).
21. Chan, J., Khan, S. N., Harvey, I., Merrick, W. & Pelletier, J. Eukaryotic protein synthesis inhibitors identified by comparison of cytotoxicity profiles. *RNA* **10**, 528–543 (2004).
22. Keller, T. L. *et al.* Halofuginone and other febrifugine derivatives inhibit prolyl-tRNA synthetase. *Nat. Chem. Biol.* **8**, 311–317 (2012).
23. Azzam, M. E. & Algranati, I. D. Mechanism of Puromycin Action: Fate of Ribosomes after Release of Nascent Protein Chains from Polysomes. *Proc. Natl. Acad. Sci. U. S. A.* **70**, 3866–3869 (1973).
24. Pestka, S. Inhibitors of Ribosome Functions. *Annu. Rev. Microbiol.* **25**, 487–562 (1971).
25. Brandi, L. *et al.* The translation initiation functions of IF2: targets for thiostrepton inhibition. *J. Mol. Biol.* **335**, 881–894 (2004).
26. Cameron, D. M., Thompson, J., March, P. E. & Dahlberg, A. E. Initiation factor IF2, thiostrepton and micrococin prevent the binding of elongation factor G to the *Escherichia coli* ribosome. *J. Mol. Biol.* **319**, 27–35 (2002).
27. Pestka, S. Thiostrepton: a ribosomal inhibitor of translocation. *Biochem. Biophys. Res. Commun.* **40**, 667–674 (1970).
28. Rogers, M. J., Cundliffe, E. & McCutchan, T. F. The Antibiotic Micrococin Is a Potent Inhibitor of Growth and Protein Synthesis in the Malaria Parasite. *Antimicrob. Agents Chemother.* **42**, 715–716 (1998).
29. Uchiumi, T., Wada, A. & Kominami, R. A Base Substitution within the GTPase-associated Domain of Mammalian 28 S Ribosomal RNA Causes High Thiostrepton Accessibility. *J. Biol. Chem.* **270**, 29889–29893 (1995).

30. Vazquez, D. The Mechanisms of Selectivity and Action of Protein Synthesis Inhibitors in Medicinal Chemistry–III (ed. Pratesi, P.) 355–370 (Butterworth-Heinemann, 1973).
31. Walter, J. D., Hunter, M., Cobb, M., Traeger, G. & Spiegel, P. C. Thiostrepton inhibits stable 70S ribosome binding and ribosome-dependent GTPase activation of elongation factor G and elongation factor 4. *Nucleic Acids Res.* **40**, 360–370 (2012).
32. Sobell, H. M. Actinomycin and DNA transcription. *Proc. Natl. Acad. Sci. U. S. A.* **82**, 5328–5331 (1985).
33. Acs, G., Reich, E. & Mori, M. Biological and Biochemical Properties of the Analogue Antibiotic Tubercidin. *Proc. Natl. Acad. Sci. U. S. A.* **52**, 493–501 (1964).
34. Andersen, T. B., López, C. Q., Manczak, T., Martinez, K. & Simonsen, H. T. Thapsigargin--from Thapsia L. to mipsagargin. *Mol. Basel Switz.* **20**, 6113–6127 (2015).
35. Plouffe, D. *et al.* In silico activity profiling reveals the mechanism of action of antimalarials discovered in a high-throughput screen. *Proc. Natl. Acad. Sci. U. S. A.* **105**, 9059–9064 (2008).
36. Kwok, J. M.-M. *et al.* Thiostrepton selectively targets breast cancer cells through inhibition of forkhead box M1 expression. *Mol. Cancer Ther.* **7**, 2022–2032 (2008).
37. Sandu, C., Ngounou Wetie, A. G., Darie, C. C. & Steller, H. Thiostrepton, a natural compound that triggers heat shock response and apoptosis in human cancer cells: a proteomics investigation. *Adv. Exp. Med. Biol.* **806**, 443–451 (2014).
38. Lai, C.-Y. *et al.* Identification of Thiostrepton as a Novel Inhibitor for Psoriasis-like Inflammation Induced by TLR7-9. *J. Immunol.* **195**, 3912–3921 (2015).

39. Lytton, J., Westlin, M. & Hanley, M. R. Thapsigargin inhibits the sarcoplasmic or endoplasmic reticulum Ca-ATPase family of calcium pumps. *J. Biol. Chem.* **266**, 17067–17071 (1991).
40. Wong, W. L., Brostrom, M. A., Kuznetsov, G., Gmitter-Yellen, D. & Brostrom, C. O. Inhibition of protein synthesis and early protein processing by thapsigargin in cultured cells. *Biochem. J.* **289**, 71–79 (1993).
41. Hussain, T., Yogavel, M. & Sharma, A. Inhibition of Protein Synthesis and Malaria Parasite Development by Drug Targeting of Methionyl-tRNA Synthetases. *Antimicrob. Agents Chemother.* AAC.02220-13 (2015).
42. Pybus, B. S. et al. The metabolism of primaquine to its active metabolite is dependent on CYP 2D6. *Malar. J.* **12**, 212 (2013).
43. Yusupova, G. & Yusupov, M. Crystal structure of eukaryotic ribosome and its complexes with inhibitors. *Philos. Trans. R. Soc. Lond. B. Biol. Sci.* **372**, (2017).
44. Romani, A. M. P. Cellular Magnesium Homeostasis. *Arch. Biochem. Biophys.* **512**, 1–23 (2011).
45. Romani, A. & Scarpa, A. Regulation of cell magnesium. *Arch. Biochem. Biophys.* **298**, 1–12 (1992).
46. Nierhaus, K. H. Mg²⁺, K⁺, and the Ribosome. *J. Bacteriol.* **196**, 3817–3819 (2014).

Chapter 4

Streptogramin A antibiotic derivatives inhibit translation through binding to *Plasmodium falciparum* and mammalian 80S ribosomes

The work presented in this chapter includes contributions from:

John Lee, Hector Chaires, Qi Li, Ian Seiple, James Fraser and Joseph L. DeRisi

4.1 Abstract

Plasmodium falciparum is the primary cause of severe malaria world wide. Widespread drug resistance to all approved antimalarials has created the need for novel therapeutics with unique mechanisms of action. Many antibiotics are effective against *P. falciparum* by inhibiting translation in the apicoplast. However, none are known to target cytoplasmic ribosomes. Recently, a method of synthesizing Streptogramin A antibiotic derivatives was developed that allows for generation of numerous compounds with potential activity against *P. falciparum*. *In vitro* growth assays using *P. falciparum* and human cell lines were done to assess the effectiveness and specificity of Virginiamycin M2, Flopristin, F224, and F1037. Next, *P. falciparum* and rabbit reticulocyte *in vitro* translation were used to determine if these compounds target cytoplasmic translation. Finally, cryo electron microscopy was used to identify where F1037 was bound within both *P. falciparum* and mammalian ribosomes. Here we show that streptogramin A antibiotics are effective at inhibiting *P. falciparum* asexual growth and inhibit translation *in vitro*. Additionally, we found that these compounds have similar effectiveness against many multiple mammalian cell lines and inhibit rabbit reticulocyte *in vitro* translation. To understand this overlapping activity, we located the binding site of F1037 to the peptidyl-transferase center of both *P. falciparum* and rabbit ribosomes. Virginiamycin M2 derivatives bind to both *P. falciparum* and mammalian ribosomes and the peptidyl-transferase center thereby inhibiting translation and causing cell death.

4.2 Introduction

Malaria remains a devastating disease worldwide. In 2019, there were approximately 229 million instances of disease leading to 409,000 deaths. Five eukaryotic species are known to cause human malaria, *Plasmodium falciparum*, *Plasmodium vivax*, *Plasmodium ovale*,

Plasmodium knowlesi, and *Plasmodium malariae*. However, *P. falciparum* causes the vast majority of cases and is associated with the most severe outcomes [1].

There are a number of therapeutics and prophylactics against *P. falciparum*, such as quinine and chloroquine. Unfortunately, there are chemoresistance mechanisms to all clinically approved antimalarials and widespread resistance to many [2]. The current frontline drugs, Artemisinin-based Combination Therapies (ACT), consist of an artemisinin derived compound combined with a secondary therapeutic. In 2009, the first signs of ACT resistance arose in Cambodia with subsequent spreading throughout Southeast Asia in the years following [3-5]. Additionally, artemisinin resistance has arisen independently in South America, making ACT therapies increasingly less effective around the world [6]. To continue the ongoing fight against malaria, there is a drastic need for novel therapeutics with unique mechanisms of action.

Two families of antibiotics have been widely studied and used as antimalarials, tetracyclines and macrolides [7]. In bacteria, tetracyclines inhibit translation through binding the A-site on the 30S ribosomal subunit [8-9]. Similarly, macrolides inhibit bacterial translation by binding near the ribosomal exit channel [10]. Both classes of compounds inhibit *P. falciparum* growth by targeting translation in the apicoplast, an essential plastid organelle that contains its own translational machinery [11]. This mechanism of action is effective after two life cycles, leading to a delayed death effect that can be measured at 96 hours post therapeutic application [12]. There are currently no approved therapeutics that specifically and effectively target *P. falciparum* cytoplasmic ribosomes as opposed to apicoplast ribosomes [7, 13].

Streptogramins are another class of antibiotics known to inhibit bacterial translation that have also been shown to induce a delayed death effect in *P. falciparum* [14], suggesting they similarly target the apicoplast. Streptogramins consist of two groups, groups A and B. A and B compounds

have distinct, but proximal, binding sites within the bacterial ribosome. Group A streptogramins bind to the peptidyl transferase center, while group B streptogramins bind near the exit tunnel. The two compound types act synergistically to inhibit translation [15].

A modular method of synthesizing unique group A streptogramins was developed to generate a large array of virginiamycin M2 (VM2) derivatives with the potential to act as antimalarials [16]. Here we determined the efficiency of VM2 and a couple of its derivatives at inhibiting *P. falciparum* growth. We found that unlike other antibiotics, these compounds acted within 72 hours, suggesting a cytoplasmic target. We also demonstrate similar effectiveness against common human cell lines then show that these compounds are able to inhibit both *P. falciparum* and mammalian cytoplasmic translation. Additionally, we determined the structures of the 80S *P. falciparum* and rabbit ribosomes bound to one of the VM2 derivatives, F1037, and show the conservation of compound binding in these two distant eukaryotic species.

4.3 Results

Growth inhibition assays with VM2, Flopristin, F224, and F1037 were performed to determine their efficacy against *P. falciparum* in culture. Unlike similar antibiotics that target the apicoplast, all four drugs were active against *P. falciparum* within 72 hours. To determine the half-maximal efficacy concentration (EC₅₀) within 72 hours, 17 different final concentrations of each compound ranging between 5nM to 500uM were used in a 72-hour growth inhibition assay (Figure 4.1a-d). The resulting EC₅₀s were 1.2uM for VM2, 1.4uM for Flopristin, 637nM for F224, and 783nM for F1037.

To screen for organism specificity, a 72-hour cytotoxicity screen was performed with each drug at the same final concentrations as above on five human cell lines: K562s (a myelogenous leukemia cell line), HFF1s (a fibroblast cell line), HepG2s (a hepatoma cell line),

HeLas(an epithelial cell line), and Hek-293Ts (an embryonic kidney cell line). Surprisingly, except for VM2 itself, the spread in EC50s for the human cell lines overlapped with the determined EC50s for *P. falciparum* (Figure 4.2, Table 4.1).

Although all four compounds were active against both *P. falciparum* and human cell lines, it remained possible that they had distinct mechanisms of action. Given that these compounds inhibit translation in *E. coli*, their efficacy against *P. falciparum* and mammalian translation was evaluated using *in vitro* translation lysates. Drug concentrations ranging from 25nM to 1mM were screened. All four compounds inhibited translation in both assays with rabbit reticulocyte lysates being more sensitive to inhibition across the board (Figure 4.1e-h).

To determine if VM2 derivatives bound to ribosomes in both systems, cryo-electron microscopy was performed on purified *P. falciparum* and rabbit ribosomes saturated with F1037. In both structures, F1037 was found within the peptidyl transferase center (PTC), as it localizes in *E. coli*. A comparison of the three structures bound to F1037 reveals the remarkable conservation of the PTC despite the long evolutionary distances between the three organisms (Figure 4.3 and Figure 4.4).

4.4 Conclusions

Virginiamycin M2, and its derivatives, all inhibit *P. falciparum* growth. However, they show cytotoxicity to human cell lines at overlapping concentrations. In both cases, they likely act by inhibiting translation through binding to the PTC of the ribosome, as they act in *E. coli*. Further screening of compounds could be aided by design to specific differences between these ribosomes, but the PTC is potentially too highly conserved to target with antimalarials.

4.5 Materials and Methods

4.5.1 Cell culture strains and maintenance

The Plasmodium falciparum W2 strain was grown at 37°C, 5% O₂, and 5% CO₂. They were maintained in human erythrocytes (2% hematocrite) in RPMIc (RPMI 1640 media supplemented with 0.25% Albumax II (GIBCO Life Technologies), 2 g/L sodium bicarbonate, 0.1 mM hypoxanthine, 25 mM HEPES (pH 7.4), and 50 µg/L gentamicin). Cultures are synchronized with 5% sorbitol at least 4 days before the first harvest.

Hek293T, HeLa, and HepG2 cells were grown at 37°C in DMEM supplemented with 10% FBS, 1X Penicillin-Streptomycin-Glutamine (Thermo Fisher Scientific 10378016), and 10mM HEPES (pH 7.2-7.5).

HFF1 cells were grown at 37°C in DMEM supplemented with 15% FBS, 1X Penicillin-Streptomycin-Glutamine (Thermo Fisher Scientific 10378016), and 10mM HEPES (pH 7.2-7.5).

K562 cells were grown at 37°C in RPMI supplemented with 10% FBS, 1X Penicillin-Streptomycin-Glutamine (Thermo Fisher Scientific 10378016), and 10mM HEPES (pH 7.2-7.5).

4.5.2 Mammalian cell 720hour growth assay

For adherent cell lines (HEK293T, HeLa, Hep2G, and HFF1s), 1250 cells were seeded into 96-well plates in 50uL of appropriate media. 24 hours later 0.5uL of drug in DMSO was added using the Labcyte Echo 525. Next, 50uL of appropriate media was added for a final volume of 100uL at 0.5% DMSO. Plates were incubated at 37°C for 72 hours.

For suspension cells, K562s, 2500 cells in 100uL of media were added to 0.5uL of drug in DMSO previously dispensed with the Labcyte Echo 525 into 96-well plates. Plates were incubated at 37°C for 72 hours.

For all mammalian cell lines, after 72 hours on drug, 100uL of Cell Titer-Glo 2.0 (Promega G9241) was added to each well. Luminescence was measured every 2 hours on a Promega Glomax plate reader. The data at 10 hours past addition was used to determine cytotoxicity.

Cytotoxicity assays were performed in triplicate on two separate occasions with overlapping concentrations between 500nM and 125uM.

4.5.3 Rabbit In Vitro Translation

Mammalian in vitro translation assays were performed using Promega's Nuclease-free Rabbit Reticulocyte Lysate (L4960). The reporter RNA consisted of the *P. falciparum* 5' untranslated region of EBA-175 followed by firefly luciferase and ending with the 3' untranslated region of *P. falciparum* HRP gene 13. 0.2uL of drug in DMSO was dispensed into white 96-well plates. 20uL of the in vitro translation mix was added consisting of: 14ul of lysate, 0.2uL of amino acid mixture without methionine, 0.2uL of amino acid mixture without cysteine, 1uL Invitrogen SUPERase-IN RNase Inhibitor, 1ug of T7-transcribed firefly luciferase mRNA, and water to 20uL. Reactions were incubated at 37°C for an amount of time that produced 50% of the maximum possible signal as determined by a lysate time course performed in the absence of drug and DMSO.

4.5.4 Plasmodium 72-hour growth assay

100uL of synchronized *P. falciparum* cultures were added to 0.5uL of drug in DMSO previously dispensed into 96-well plates with the Labcyte Echo 525. The plates were then incubated at 37°C, 5% O₂, and 5% CO₂ for 72 hours. Next, the cultures were fixed with 1% paraformaldehyde and stained with 250nM YO-YO1 (Invitrogen). Parasites were counted on the BD-LSRII (for original compounds) or the Attune NxT Flow Cytometer (exit reaching

compounds). Parasitemia was calculated using FlowJo software version 10 by gating on empty red blood cells and plotted in GraphPad Prism.

72-hour growth assays were performed in triplicate on two separate occasions with overlapping for concentrations between 500nM and 125uM.

4.5.5 Plasmodium In Vitro Translation

P. falciparum cultures were maintained and lysates were prepared as previously detailed [17]. In brief:

Lysate generation Synchronized *Plasmodium falciparum* W2 cultures were grown in 500mL HYPERFlasks (Corning 10031) at 2-4% hematocrit. Cultures were harvested when they reached 15-20% parasitemia and the parasites were late trophozoites or early schizonts. Cultures were harvested by spinning down at 1500xg for 5 minutes at room temperature. The red blood cells were then lysed using ice cold 0.05% final saponin in Buffer A (20 mM HEPES pH 8.0, 2 mM Mg(OAc)₂, 120 mM KOAc). The concentration of saponin for each preparation was determined through testing as described previously¹⁷. Lysed pellets were spun at 10000 xg for 10 mins at 4°C. Pellets were then washed 2 times by removing the supernatant and resuspending with 50mL buffer A then spun at 10000 xg for 10 mins at 4°C. After two washes the pellets were resuspended in an equal volume of Buffer B2 (20 mM HEPES pH8.0, 100 mM KOAc, 0.75 mM Mg(OAC)₂, 2 mM DTT, 20% glycerol, 1X EDTA-free protease inhibitor cocktail (Roche)), flash frozen in liquid nitrogen, and stored at -80°C until lysis.

Frozen pellets were thawed on ice and loaded into a 3mL Luer lock syringe. Lysates were then passed 20 times through a cell homogenizer with a 4um-clearance ball bearing (Isobiotec, Germany) using a programmable dual syringe pump 18 Lysed pellets were spun at 16,000xg for 10mins at 4°C. The supernatant was transferred and flash frozen in liquid nitrogen. A small

100uL aliquot was made to test lysate for activity (at least 104 RLU when tested with the firefly reporter RNA used in the other experiments). Active lysates from multiple harvests were pooled together, optimized for Mg(OAc)₂ concentration, and finally used in a time course to determine when 50% of the maximum signal is produced as previously described.

In vitro translation reactions 20uL reactions were performed with 14 μL lysate, 1 μg T7-transcribed firefly luciferase mRNA, 10 μM amino acid mixture, 20 mM HEPES/KOH pH 8.0, 75 mM KOAc, 2 mM DTT, 0.5 mM ATP, 0.1 mM GTP, 20 mM creatine phosphate, 0.2 μg/μL creatine kinase, and the appropriate amount of Mg(OAc)₂ as determined for the particular pool of extract. Reactions were incubated at 37°C for the amount of time determined by a lysate time course that produces 50% of the maximum possible signal with the firefly luciferase mRNA.

4.5.6 Ribosome Purification

4.5.6.1 Sucrose cushion

Two sucrose cushions were prepared for each organism at a time. 100uL of *P. falciparum* in vitro translation lysate or Promega's Nuclease-free Rabbit Reticulocyte Lysate (L4960) was layered on top of 1 mL 25% sucrose solution with 140mM KoAc, 15mM MgCl₂, 20mM Tris HCl pH 7.4, and 0.5mM DTT in a Beckman Culture 3.2mL tube (Fisher Scientific NC9452231). Sucrose cushions were spun at 70,000rpm for 4 hours at 4°C in a Beckman Optima TLX ultracentrifuge using the TLA110 rotor. Post-spin, the supernatant was removed and both pellets were resuspended and combined in 800uL of storage buffer (200mM Tris-HCL pH7.5, 600mM NH₄Cl, 60mM MgCl₂, and 5mM EDTA).

4.5.6.2 Sucrose Gradient

Four sucrose gradients were prepared for 800uL of resuspended pellet. 6-7mLs of 10% sucrose was placed carefully on top of 6-7mLs of 50% sucrose in a 14x89mm Open-Top Polyclear Centrifuge Tube (Seton 7030). A 7-47% sucrose gradient was made using a Biocomp Instruments Gradient/Fractionator combo. 200uL of resuspended pellet from the sucrose cushion was loaded on top of each gradient and spun in a Beckman ultracentrifuge SW41 bucket at 35,000rpm at 4°C for 3 hours.

4.5.6.3 Fractionation/ Ribosome Concentration

Fractioning was performed using a Biocomp Instrument Gradient/ Fractionator combo. Fractions containing 80S ribosomes were pooled together, buffer exchanged, and concentrated using a 15mL 100Kda Amicon Ultra Centrifugal Filter. The pooled fractions were brought to 15mLs with storage buffer (200mM Tris-HCL pH7.5, 600mM NH₄Cl, 60mM MgCl₂, and 5mM EDTA) and spun for 20 minutes 3,202xg at 4°C. This was repeated 3 times with the final spin being 30 minutes. After the final spin, ribosomes were stored at 4°C overnight before making cryo-grids.

4.5.7 Sample Vitrification and Screening

100 nM ribosomes were incubated in the presence of 60 μM F1037 for one hour in an ice bath. 3 uL of sample was deposited onto a freshly glow discharged (15 mA for 30 s, EMS-100 Glow Discharge System, Electron Microscopy Sciences) 300 mesh Quantifoil Copper grid with 1.2/1.3 spacing and 2 nm thick amorphous carbon on top (C2-C14nCu30-01, Quantifoil Micro Tools GmbH). Vitrification was achieved using a Vitrobot Mk IV (ThermoFisher Scientific) with a 30 second incubation at 10 °C and 95% humidity, then blotting with a blot force of 3 and Whatman #1 blotting papers, and finally plunge freezing into liquid ethane. To ensure adequate

ice thickness, four grids were frozen for each sample with varied blot times (7, 9, 11, 13 seconds). Samples were screened for ice quality and particle distribution using an FEI Talos Arctica (200 kV acceleration voltage, ThermoFisher Scientific) located at UCSF.

4.4.7 Cryo-EM data collection

Optimal grids were imaged using FEI Titan Krios electron microscopes (ThermoFisher Scientific, 300 kV acceleration voltage) using beam tilt-image shift collection approaches with coma compensation. *P. falciparum* ribosomes were imaged in super-resolution counting mode by ThermoFisher Scientific in the Netherlands on a Krios equipped with a Falcon IV Direct Electron Detector (DED) using EPU (ThermoFisher Scientific). Rabbit ribosomes were imaged in super-resolution counting mode at UCSF on a Krios equipped with a K3 (Gatan) DED, a Gatan Imaging Filter (Gatan, 20 eV slit) using SerialEM (v3.6).

4.5.8 Cryo-EM image and data processing

Super-resolution dose-fractionated micrographs were corrected for beam-induced motion, binned by a factor of 2, and dose-weighted using MotionCor2. All other processing was carried out using the dose-weighted micrographs in the cisTEM (1.0.0-beta) software suite. In brief, CTF parameters were determined using CTFFIND4 and the micrographs were curated to remove crystalline ice and poor CTF fits. Particles were picked using a gaussian blob template appropriate to the size of the ribosomes in each dataset. Particle counts are reported in table XX. 2D classification was performed on the particle stacks to further remove ice, but all other classes were carried forward to a two-class Auto refinement. Iterative rounds of refinement yielded a high-quality ribosome volume and a class containing primarily high-frequency noise and poorly aligned particles. Particles associated with the ribosome volume were carried forward into a single-class auto refinement followed by manual refinement approaches including per-particle

CTF refinement. Unsharpened maps were used in model refinement and representation in figures.

4.5.9 Cryo-EM model building

Primary model refinement was carried out using the PHENIX software suite (1.19). 5UMD was used as the starting point for the *Plasmodium falciparum* ribosomes while 6SGC was the starting point for the Rabbit ribosomes. Chimera, ChimeraX, ISOLDE, and coot were used for visualization and to improve the model.

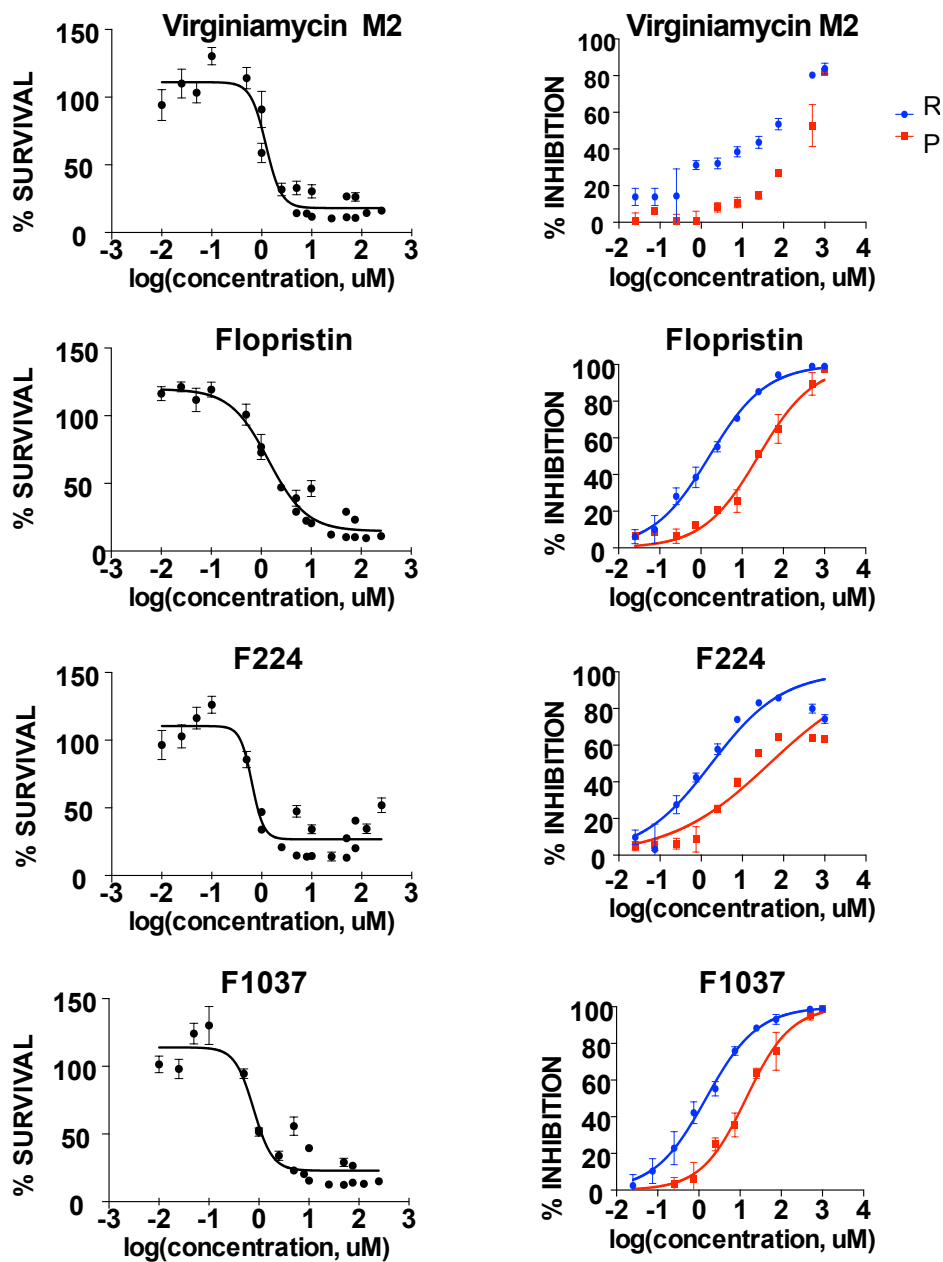


Figure 4.1: 72-hour growth and *in vitro* translation inhibition curves with Virginiamycin M2, Flopristin, F224, and F1037

To the left is the EC₅₀ curves in *P. falciparum* in a 72-hour growth assay. To the right is the inhibition curves in both *P. falciparum* and rabbit reticulocyte *in vitro* translation. Graphed for both are the means and SEMs.

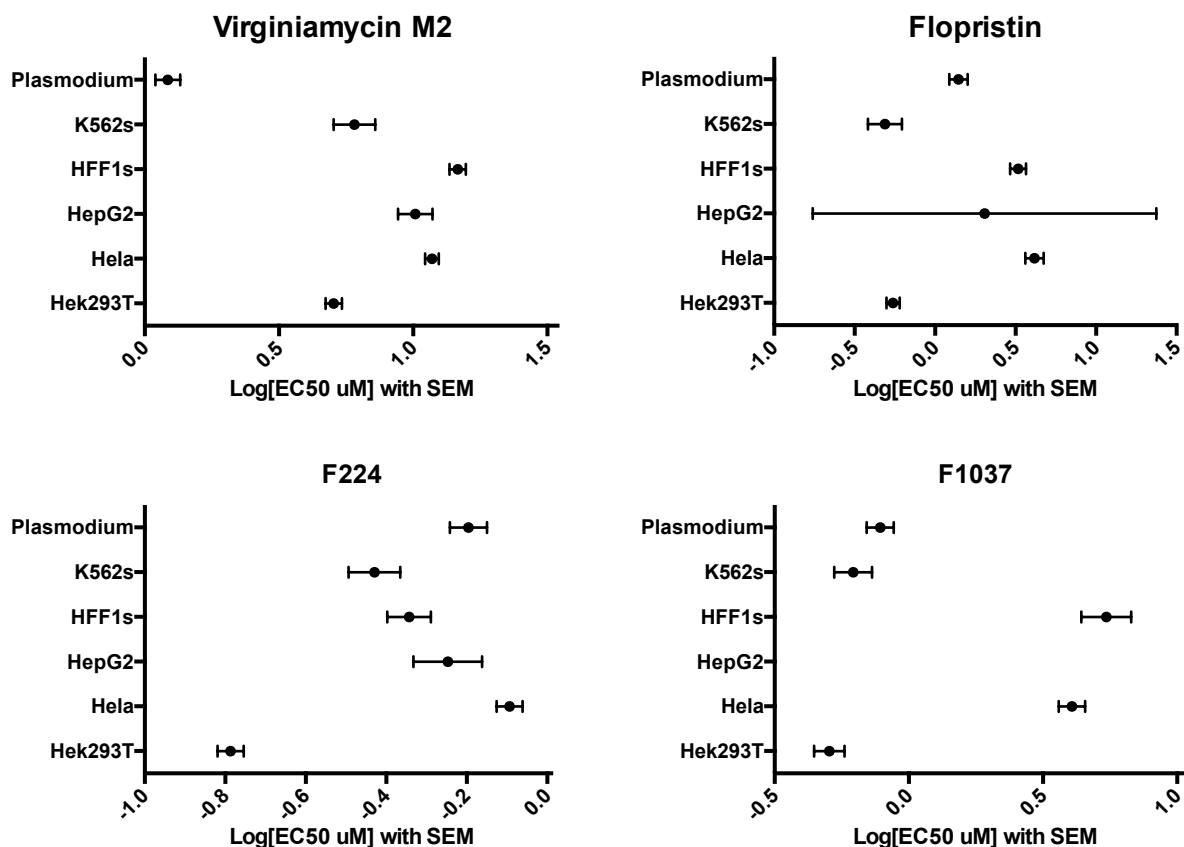


Figure 4.2: EC50 comparison between *P. falciparum* and human cell lines
 Error bars represent the SEM and the data point is the mean of the EC50s determined by the growth assay replicates.

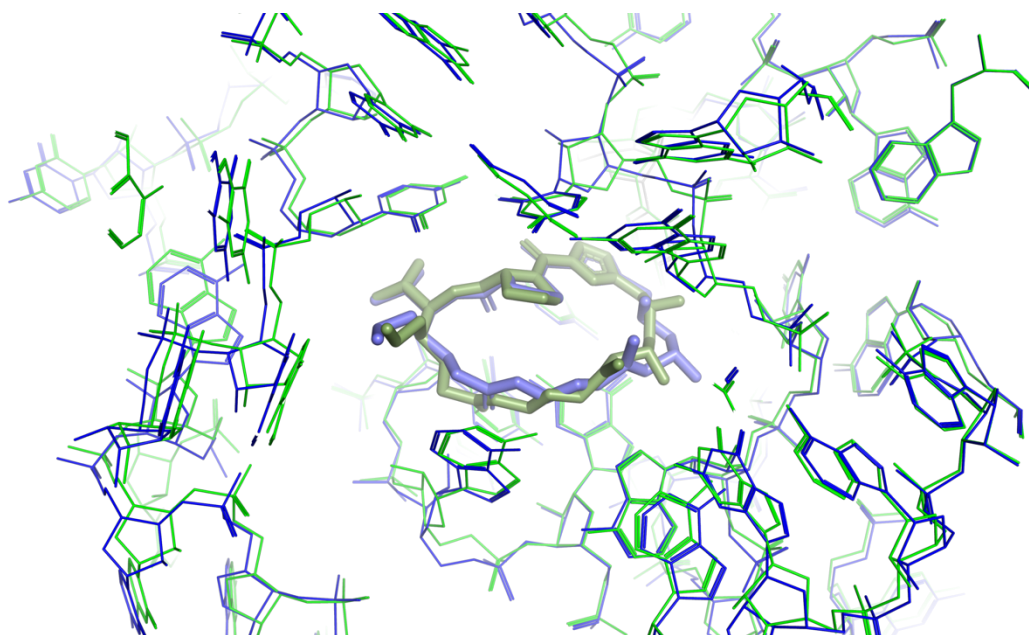


Figure 4.3: F1037 bound to the PTC in *P. falciparum* and rabbit ribosomes
 Cryo-electron microscopy structures of the PTC bound to F1037. *P. falciparum* ribosome and compound are in green. Rabbit ribosome and compound are blue.

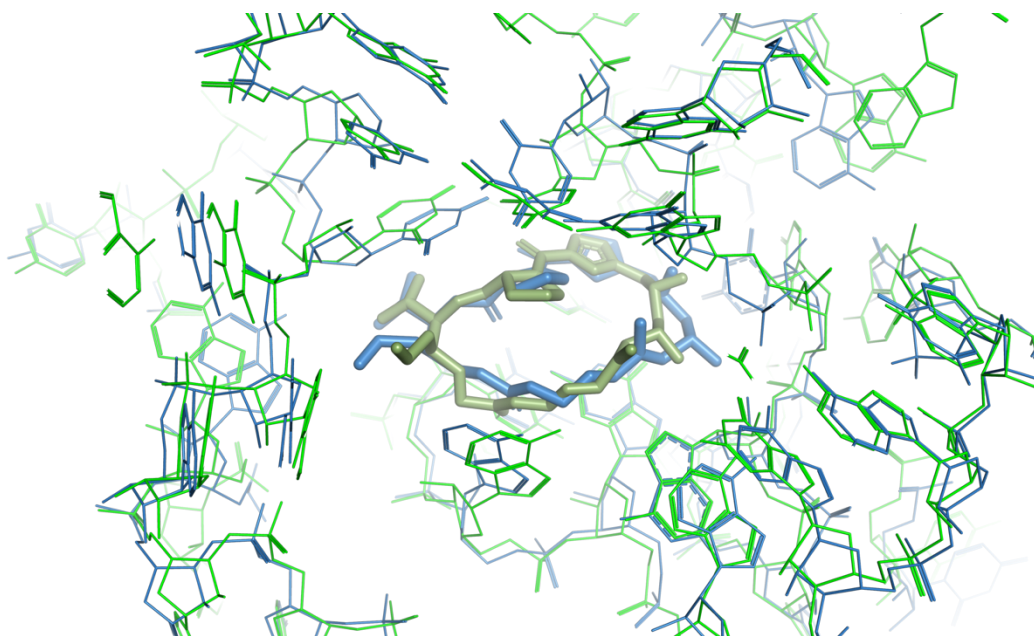


Figure 4.4: F1037 bound to the PTC in *P. falciparum* and *e. coli*

Cryo-electron microscopy structures of the PTC bound to F1037. *P. falciparum* ribosome and compound are in green. *E. coli* ribosome and compound are blue. The *E. coli* structure is from reference [16].

Table 4.1: EC50s for each compound in the various cell types.

*The EC50 for HepG2 cells with F1037 was not possible due to the nature of the curve generated at these concentrations.

Compound	<i>P. falciparum</i>	K562	Hff1	HepG2	HeLa	Hek293T
VM2	1.22uM	6.04uM	14.65uM	10.18uM	11.76uM	5.06uM
Flopristin	1.4uM	488nM	3.28uM	2.03uM	4.15uM	548nM
F224	637nM	372nM	454nM	566nM	806nM	163nM
F1037	783nM	620nM	5.4uM	N/A*	4.06uM	506nM

Chapter 4 References

1. World Malaria Report 2019. <https://www.who.int/publications-detail/world-malaria-report-2019> (2019).
2. Schlitzer, M. Malaria chemotherapeutics part I: History of antimalarial drug development, currently used therapeutics, and drugs in clinical development. *Chem. Med. Chem.* **2**, 944–986 (2007).
3. Dondorp, A. M. et al. Artemisinin resistance in *Plasmodium falciparum* malaria. *N. Engl. J. Med.* **361**, 455–467 (2009).
4. Fairhurst, R. M. & Dondorp, A. M. Artemisinin-Resistant *Plasmodium falciparum* Malaria. *Microbiol. Spectr.* **4**, (2016).
5. Hassett, M. R. & Roepe, P. D. Origin and Spread of Evolving Artemisinin-Resistant *Plasmodium falciparum* Malarial Parasites in Southeast Asia. *Am. J. Trop. Med. Hyg.* **101**, 1204–1211 (2019).
6. Mathieu, L. C. et al. Local emergence in Amazonia of *Plasmodium falciparum* k13 C580Y mutants associated with *in vitro* artemisinin resistance. *eLife* **9**, e51015 (2020).
7. Gaillard, T., Madamet, M., Tsombeng, F. F., Dormoi, J. & Pradines, B. Antibiotics in malaria therapy: which antibiotics except tetracyclines and macrolides may be used against malaria? *Malaria Journal* **15**, 556 (2016).
8. Day, L. E. Tetracycline inhibition of cell-free protein synthesis. I. Binding of tetracycline to components of the system. *J. Bacteriol.* **91**, 1917–1923 (1966).
9. Brodersen, D. E. et al. The structural basis for the action of the antibiotics tetracycline, pactamycin, and hygromycin B on the 30S ribosomal subunit. *Cell* **103**, 1143–1154 (2000).

10. Vázquez-Laslop, N. & Mankin, A. S. How Macrolide Antibiotics Work. *Trends Biochem. Sci.* **43**, 668–684 (2018).
11. Dahl, E. L. et al. Tetracyclines Specifically Target the Apicoplast of the Malaria Parasite *Plasmodium falciparum*. *Antimicrob. Agents Chemother.* **50**, 3124–3131 (2006).
12. Dahl, E. L. & Rosenthal, P. J. Multiple antibiotics exert delayed effects against the *Plasmodium falciparum* apicoplast. *Antimicrob. Agents Chemother.* **51**, 3485–3490 (2007).
13. Ahyong, V. et al. Identification of *Plasmodium falciparum* specific translation inhibitors from the MMV Malaria Box using a high throughput *in vitro* translation screen. *Malaria Journal* **15**, 173 (2016).
14. Barthel, D., Schlitzer, M. & Pradel, G. Telithromycin and quinupristin-dalfopristin induce delayed death in *Plasmodium falciparum*. *Antimicrob. Agents Chemother.* **52**, 774–777 (2008).
15. Harms, J. M., Schlünzen, F., Fucini, P., Bartels, H. & Yonath, A. Alterations at the peptidyl transferase centre of the ribosome induced by the synergistic action of the streptogramins dalfopristin and quinupristin. *BMC Biol.* **2**, 4 (2004).
16. Li, Q. & Seiple, I. B. Modular, Scalable Synthesis of Group A Streptogramin Antibiotics. *J. Am. Chem. Soc.* **139**, 13304–13307 (2017).
17. Sheridan, C. M., Garcia, V. E., Ahyong, V. & DeRisi, J. L. The *Plasmodium falciparum* cytoplasmic translation apparatus: a promising therapeutic target not yet exploited by clinically approved anti-malarials. *Malaria Journal* **17**, 465 (2018).
18. Garcia, V. E., Liu, J. & DeRisi, J. L. Low-cost touchscreen driven programmable dual syringe pump for life science applications. *HardwareX* **4**, e00027 (2018).

Chapter 5

Comparing the role of cis-acting regulatory sequences in mediating translational efficiency for *P. falciparum* and humans

This chapter includes material in preparation included in the preprint:

Valentina E. Garcia, Rebekah Dial, and Joseph L. DeRisi. Functional characterization of 5' UTR cis-acting sequence elements that modulate translational efficiency in *P. falciparum* and humans. BioRxiv (2021): doi: <https://doi.org/10.1101/2021.09.07.459299>

Authors' Contributions

VEG and JLD conceived and designed this study. VEG performed and executed the experiments. RD maintained, harvested, and generated *in vitro* translation lysates for the K562 cells. VEG and JLD drafted and edited this manuscript. All authors read and approved the submitted manuscript.

Additional/supplemental files that are not figures can be found with the pre-print

5.1 Abstract

The eukaryotic parasite *Plasmodium falciparum* causes millions of malarial infections annually while drug resistance to common antimalarials is further confounding eradication efforts. Translation is an attractive therapeutic target that will benefit from a deeper mechanistic understanding. As the rate limiting step of translation, initiation is a primary driver of translational efficiency. It is a complex process regulated by both *cis* and *trans* acting factors, providing numerous potential targets. Relative to model organisms and humans, *P. falciparum* mRNAs feature unusual 5' untranslated regions suggesting *cis*-acting sequence complexity in this parasite may act to tune levels of protein synthesis through their effects on translational efficiency. Here, we deployed *in vitro* translation to compare the role of *cis*-acting regulatory sequences in *P. falciparum* and humans. Using parasite mRNAs with high or low translational efficiency, the presence, position, and termination status of upstream "AUG"s, in addition to the base composition of the 5' untranslated regions, were characterized. The density of upstream "AUG"s differed significantly among the most and least efficiently translated genes in *P. falciparum*, as did the average "GC" content of the 5' untranslated regions. Using exemplars from highly translated and poorly translated mRNAs, multiple putative upstream elements were interrogated for impact on translational efficiency. Upstream "AUG"s were found to repress translation to varying degrees, depending on their position and context, while combinations of upstream "AUG"s had nonadditive effects. The base composition of the 5' untranslated regions also impacted translation, but to a lesser degree. Surprisingly, the effects of *cis*-acting sequences were remarkably conserved between *P. falciparum* and humans. While translational regulation is inherently complex, this work contributes toward a more comprehensive understanding of parasite and human translational regulation by examining the impact of discrete *cis*-acting features, acting alone or in context.

5.2 Background

As the primary cause of severe malaria, *Plasmodium falciparum* remains a major global health threat. In 2018, approximately 228 million cases of malaria led to 405,000 deaths, primarily of children under the age of 5 [1]. Control and eradication of *P. falciparum* is complicated by widespread or emerging drug resistance to all common antimalarial drugs [2-4]. To circumvent drug resistance, targeted therapeutic development has the potential to generate novel antimalarials with unique mechanisms of action. Unfortunately, targeted development is hindered by an incomplete understanding of the basic molecular processes of *P. falciparum* and how they differ from human biology.

Recently, translation has emerged as a potentially druggable pathway [5-7]. While no clinically approved antimalarials target cytoplasmic translation [5], there are promising new candidates to distinct translational mechanisms. For example, there is a growing number of compounds targeting tRNA synthetases [8-9], M5717 (formerly DDD107498) is currently in human trials and inhibits eukaryotic elongation factor 2 [6, 8], and MMV008270 has been shown to selectively inhibit parasite translation through an unknown mechanism of action [10]. Currently no candidates are known to target translation initiation.

Eukaryotic translation initiation determines the rate of translation of a given mRNA, referred to as the translational efficiency (TE) [11-12]. Initiation at the proper translation start site (typically an “AUG” start codon) relies on interactions between the start codon and the local sequence context (the Kozak sequence) with the initiator Met-tRNA and other initiation factors [13-15]. TE can additionally be regulated by *cis*-acting sequence elements throughout the 5' untranslated region (5' UTR), the sequence preceding the translation start site. In particular, upstream “AUG”s (uAUGs) are commonly observed regulatory features that are divided into two

groups: those that initiate open reading frames that extend beyond the translation initiation site, and those that are terminated, meaning they form upstream open reading frames (uORFs) by having an in-frame stop site preceding the protein coding region [16-18]. These *cis*-acting regulatory elements lower TE through many potential mechanisms including by initiating translation out of frame from the downstream ORF, by adding long amino acid extensions at the N-terminus, or by sequestering ribosomes within the 5' UTRs [19-21].

A well-documented example of uAUG/uORF driven regulation is GCN4 in *Saccharomyces cerevisiae*. The 5' UTR of GCN4 contains four short uORFs that themselves are differentially translated under conditions of stress. Based on the availability of translation initiation factors, the uORFs modulate the translation rate of the primary protein coding region to fit the organisms current nutrient conditions [22-23]. While this example is deeply understood, it is not broadly generalizable, and the rules by which such sequences exert influence on TE remain challenging to describe even for the most studied of eukaryotes. For example, numerous variables have been identified in other contexts that modulate the effect of uAUGs and uORFs, including the Kozak sequence of the uAUG itself and the reading frame relative to the translational start site [19, 24].

Studies of *P. falciparum* have confirmed that it possesses the expected eukaryotic cap-binding factors required for cap-dependent translation initiation [25-26]. Additionally, gene specific studies show that uAUGs and uORFs can repress translation in *P. falciparum* and that the Kozak sequence of uAUGs along with uORF length may modulate their effect on TE [27-28]. This is particularly intriguing since *P. falciparum* has repeatedly been shown to have unusually long 5' UTRs containing many uAUGs [18, 29-30]. Together this suggests that multiple *cis*-acting factors within the 5' UTRs of *P. falciparum* could act broadly to tune TE

throughout the normal lifecycle, as opposed to regulating specific genes under extreme conditions, such as with GCN4 regulation. However, extensive ribosome profiling from our lab revealed that transcription and translation rates are highly correlated throughout the intraerythrocytic life cycle with less than 10% of the transcriptome being under significant translational control [18]. Ribosome profiling also showed that the presence of uAUGs and uORFs did not appear to correlate with TE, which is in contrast to model organisms and classic paradigms like yeast GCN4. Together this highlights that it remains difficult to predict how *cis*-acting sequences within a given 5' UTR will affect TE, especially in disparate eukaryotic species.

Here, we sought to understand the interconnected effects of 5' UTR *cis*-acting regulatory elements with respect to TE in both *P. falciparum* and human cells through a highly reductionist approach. To do so, we deployed an *in vitro* translation assay for *P. falciparum* and developed an equivalent assay for human K562 cells. Using a pair of naturally occurring *P. falciparum* 5' UTRs with differing TEs, the individual contributions of the sequence context, positionality, and termination status of uAUGs, along with the base composition of the 5' UTR to TE, were systematically dissected to understand their contributions, in isolation and in combination. Together these data present a complex portrait of interacting elements within 5' UTRs that directly influence TE, most of which are similar in both *P. falciparum* and human.

5.3 Methods

5.3.1 Identifying characteristics associated with high and low TE from the 5' UTRs of *P. falciparum*

The ribosome profiling and mRNA sequencing data from the late trophozoite stage generated by Caro and Ahyong *et. al.* 2014 [18] were filtered for an abundance above 32 reads per million, a TE greater than zero, and a predicted 5' UTR length above 175 nucleotides.

Additionally, 30 genes that are not included in the PlasmoDB-28 *P. falciparum* 3D7 gene annotations were removed. This resulted in a data set containing 2088 genes (Additional File 1). The 5' UTR sequences were determined using the PlasmoDB-28 *P. falciparum* 3D7 genome. Sequence analysis was done using Python, K.S. tests were done using the Python SciPy package, and the data for Figure 5.1, 5.2, and 5.3 was graphed using the Python Matplotlib package.

5.3.2 Cloning length variations of PF3D7_1411400 and PF3D7_1428300 5' UTRs

The first step to generating the constructs used here was to create a Puc118-NanoLuc construct without a 5' UTR (Additional File 2). Using In-fusion cloning the 5' UTR and firefly luciferase enzyme from the EBA175-Firefly plasmid used previously [5,10] were replaced with the NanoLuc Luciferase (Promega) coding sequence. The plasmid generated, called P16, consists of: Puc118 backbone with a T7 promoter proceeding the NanoLuc Luciferase protein coding sequence followed by the 3' UTR from PF_HRP2.

To create the varying length 5' UTR constructs, the 5' UTR sequences of PF3D7_1411400 and PF3D7_1428300 were amplified from *P. falciparum* W2 strain gDNA using Kapa 2G Robust DNA polymerase (Roche KK5024) with primers containing overhangs with the T7 promoter (forward primer) or NanoLuc (reverse primer). The P16 plasmid was amplified using Phusion polymerase (NEB M0530S) for the backbone (forward primer: ATGGTCTTCACACTCGAAGATTTTC, reverse primer: CCTATAGTGAGTCGTATTAGAATTTCG). The inserts and backbone were purified using a Zymo DNA Clean and Concentrator-5 (Zymo Research D4013). In-fusion reactions were performed per the In-fusion Cloning Kit (Takara 638918) instructions and reactions were transformed into Stellar Competent Cells (Takara 636766).

5.3.3 Cloning 5' UTR 130 nucleotide constructs

To generate the 130 nucleotide 5' UTR constructs, long oligos containing an EcoRI-HF cut site, the T7 promoter, the desired 5' UTR sequence, and a priming sequence to NanoLuc were purchased from Integrated DNA Technologies (forward primer: TGATTACGAATTCTAATACGACTCACTATAGG- desired 5' UTR - ATGGTCTTCACACTCGAAGATTTTC). The P16 plasmid was used as a template for PCR using Kapa 2G Robust with the reverse primer binding just after the BamHI-HF restriction site in Puc118 (reverse primer: CTGCAGGTCGACTCTAGA). PCR products were run on a 1% agarose gel to check the product size and purified using Zymo DNA Clean and Concentrator-5 (Zymo Research D4013). To create the cloning insert, purified PCR product was digested with EcoRI-HF and BamHI-HF at 37°C for 1.5 hours and purified again using a Zymo DNA Clean and Concentrator-5 (Zymo Research D4013). For the cloning backbone, P16 was digested with EcoRI-HF and BamHI-HF at room temperature overnight (~12 hours), run on a 1% agarose gel, and gel extracted with the Zymoclean Gel DNA Recovery Kit (Zymo Research D4008). The insert and backbone were ligated using T4 DNA ligase (NEB M0202S) at room temperature for 30 mins and heat inactivated at 65°C for 10 mins. After heat inactivation, the reaction was transformed into Stellar Competent Cells (Takara 636766). All constructs were sequence verified. The sequences for all the 5' UTRs evaluated can be found in Additional File 3.

5.3.4 Generating reporter RNA for *in vitro* translation

All mRNA generating plasmids were digested with PvuII-HF (NEB R[Δ4]151L) and ApaLI-HF (NEB R0507L) at 37°C for 3 hours. After digestion, templates were run on a 1% agarose gel to confirm cutting and the reactions were purified with Zymo DNA Clean and Concentrator-5 (Zymo Research D4013). 1 μg of linearized template was used in a 100 μL T7

RNA Polymerase (purified in house) reaction that was incubated at 37°C for three hours. After T7 reactions were complete, 15uL TurboDNase (ThermoFisher Scientific AM2238) was added, and reactions were incubated at 37°C for 15 minutes. The RNA was then purified using a Zymo RNA Clean and Concentrator-25 Kit (Zymo Research R1017). Eluted RNA was measured using the Qubit RNA HS Assay Kit (Thermo Fisher Scientific Q32852) then capped following the protocol for the Vaccinia Capping System (NEB M2080S) and purified one last time using Zymo RNA Clean and Concentrator-5 (Zymo Research R1013). Capped RNA concentrations were measured using the Qubit RNA HS Assay Kit (Thermo Fisher Scientific Q32852). Final RNA was diluted to 0.25pmoles/ul for use in the *in vitro* translation assays.

For the comparing capped versus uncapped mRNA, uncapped RNA was incubated for 5 minutes at 65°C to match the treatment of capped RNAs. The same RNA that was used in the vaccinia capping reaction was directly compared to the post-cap RNA.

5.3.5 Generating *P. falciparum* *in vitro* translation lysates

P. falciparum W2 strain (MRA-157) from MR4 was grown in human erythrocytes at 2% hematocrit in RPMIc medium (RPMI 1640 media supplemented with 0.25% Albumax II (GIBCOLife Technologies), 2 g/L sodium bicarbonate, 0.1 mM hypoxanthine, 25 mM HEPES (pH 7.4), and 50µg/L gentamicin), at 37°C, 5%O₂, and 5%CO₂. Cultures were maintained at 2-5% parasitemia.

In depth step-by-step protocols for lysate generation have been previously published[5]. In summary, cultures were synchronized twice using 5% sorbitol six hours apart. Once cultures recovered to 10% parasitemia, they were used to seed two 500mL hyperflasks (Corning 10031). When cultures reached the late trophozoite stage at 10–20% parasitemia, the cultures were centrifuged for 5 min at 1500g at room temperature with no break, the supernatant was removed,

and 0.025–0.05% final saponin (exact amount determined by optimization of each batch of saponin) in Buffer A (20 mM HEPES pH8.0, 2mM Mg(OAc)₂, 120mM KOAc) was added. Saponin lysed cultures were centrifuged at 4°C at 10,000g for 10 min in a Beckman Coulter J26XPI. Pellets were washed twice with buffer A with centrifuging between each wash and then were re-suspended in an equal volume to the pellet of BufferB2 (20 mM HEPES pH8.0, 100 mM KOAc, 0.75mM Mg(OAc)₂, 2mM DTT, 20% glycerol, 1X EDTA-free protease inhibitor cocktail (Roche)), flash frozen, and stored in -80°C. Frozen pellets were then thawed at 4°C and lysed by passing them through a cell homogenizer containing a 4µm-clearance ball bearing (Isobiotec, Germany) 20 times by hand or using a custom build machine³¹. The whole-cell lysate was then centrifuged at 4°C at 16,000g for 10 min and the supernatant was flash frozen and stored at -80°C. The experiments performed here used a pool of lysates from multiple different harvests that were each individually tested for a minimal activity of 10⁴ using a high expression RNA containing NanoLuc (A[WT]) and the Promega Nano-Glo Luciferase assay system (Promega N1110). Pooled lysates were then optimized for the needed amount of Mg(OAc)₂ and an optimal incubation time at 37°C, in this case 3mM final concentration Mg(OAc)₂ and 57 minutes.

5.3.6 Generating K562 *in vitro* translation lysates

K562 suspension cells were cultured in RPMI 1640 media supplemented with 10% fetal bovine serum, 10mM HEPES (pH 7.2-7.5), and 0.5mg/mL Penicillin-Streptomycin-Glutamine. Cultures were maintained by splitting to 10⁵ cells/mL and were counted using a BD Accuri.

When cells reached 10⁶ cells/mL, the cultures were centrifuged for 5 min at 1500g at room temperature and the supernatant was removed. Pellets were washed twice with buffer A with centrifuging at 1500g at 4°C between each wash. Finally, pellets were re-suspended in an equal volume of Buffer B2 and flash frozen in liquid nitrogen. Cell lysates were generated from

the frozen pellets using the same methodology as *P. falciparum* lysates, but with the cell homogenizer containing a 12 μm -clearance. Lysates that produced over 10^4 luminescence units using a high expression RNA containing NanoLuc Luciferase (A[WT]) and the Promega Nano-Glo Luciferase assay system (Promega N1110) in preliminary tests were pooled and optimized for the needed amount of $\text{Mg}(\text{OAc})_2$ and incubation time using A[WT] mRNA, in this case 1.5mM final concentration $\text{Mg}(\text{OAc})_2$ and 12 minutes.

5.3.7 *In vitro* translation protocol

In vitro translation reactions for *P. falciparum* and K562 lysates were set up identically. 3uL of buffer B2 and 2uL of 0.25pmole/uL RNA were placed into 384-well plates. A master mix of 3.5uL lysate with 0.5uL 100uM complete amino acid mix (Promega L4461) and 1uL 10x translation buffer (20mM Hepes pH 8, 75mM KoAc, 2mM DTT, 5mM ATP, 1mM GTP 200mM creatine phosphate, 2ug/ul Creatine kinase, and the pre-determined concentration for each lysate pool of $\text{Mg}(\text{OAc})_2$) was added to each well. Reactions are then incubated for the pre-determined amount of time at 37°C , then placed on ice to stop the reactions. 8uL of reaction was mixed with 8uL of Nano-Glo buffer/substrate mix following the Nano-Glo Luciferase Assay System (Promega N1110) instructions. Luminescence was measured on a Promega GloMax Plate Reader (Promega TM297) with a 6 second integration time.

5.3.8 Analysis

5.3.8.1 Experimental TEs

All experiments were performed three separate times in triplicate, for a total of 9 values per mRNA tested (except for the capped and uncapped experiment which was done 3-4 times in duplicate). For each separate experiment, new mRNA was generated and capped. For the figures, each value was normalized to the mean of the triplicates from each separate run. All raw values

and normalized values can be found in Additional File 4. The fold differences were \log_2 transformed and then used to calculate the mean and SEM. Graphs for the figures were made using a custom Python/Postscript script (Additional File 5).

5.3.8.2 Predicted activity of multiple uAUGs

The percent repression of each uAUG individually was calculated by determining the percent of R[$\Delta 1:\Delta 2:\Delta 3:\Delta 4$] (the “maximum signal”). For the predictions, the percent repression of each uAUG in the model were multiplied together.

5.3.8.3 Predicted Secondary Structures

To evaluate for secondary structure, the ΔG of 30 nucleotide stretches of the 5' UTR tiled with a 5 nucleotide separation was generated using RNAfold [32]. The predicted ΔG were then plotted using GraphPad Prism Software.

5.4 Results

*5.4.1 Identifying putative cis-acting elements within the 5' UTRs of *P. falciparum* that differ between genes with high and low TE*

To identify putative *cis*-acting sequences that regulate TE in *P. falciparum*, the ribosome profiling and mRNA sequencing data generated by Caro and Ahyong *et. al.* [18] was re-analyzed by comparing the 5' UTR sequences of genes in the bottom 10% and top 10% of TEs during the late trophozoite stage (Figure 5.1A). Features within the 5' UTRs were quantified, and the distributions from each set were compared. While the distributions of 5' UTR length were not statistically distinct (K.S. test $p=0.10$ Figure 5.2A), the distributions of uAUG frequency differed significantly and appeared distinctly separated when normalized to 5' UTR length with lower TE genes tending to contain more uAUGs (K.S. test $p= 3.36*10^{-9}$ and $p=1.1*10^{-21}$ respectively)

(Figure 5.1B and 5.2B) . This trend appeared to be most distinct closest to the protein coding region (Figure 5.1C).

Additionally, the distributions of GC content statistically differed between 5' UTRs with low and high TE (K.S. test $p=2.24 \times 10^{-5}$) (Figure 5.1D). The positional effect followed a similar trend with repressed genes on average having a higher GC content, especially near the translational start site (Figure 5.1E). Together, this retrospective bioinformatic analysis suggested that these two features should be further investigated for their role in influencing TE with particular attention placed on the sequence region proximal to the translation start site.

5.4.2 Evaluating P. falciparum and human K562 in vitro translation assays for measuring the effect of 5' UTRs on TE

To investigate the role of *cis*-acting elements within 5' UTRs, an *in vitro* translation assay previously developed for identifying translation inhibitors against *P. falciparum* [5, 10] was adapted using both *P. falciparum* W2 and *H. sapiens* K562 cellular extracts. To validate and optimize the platform for this purpose, two mRNAs transcribed in late trophozoites with significantly different TEs were identified, PF3D7_1411400 (a plastid replication-repair enzyme) representing a translationally repressed mRNA from the bottom 10% of TEs and PF3D7_1428300 (a proliferation-associated protein) representing a high translation mRNA from the top 10% of TEs. These two genes were chosen for their relatively similar 5' UTR lengths and other properties (Figure 5.3 A and B). The full length 5' UTRs of both genes (Figure 5.2A) were cloned into a reporter construct driving expression of a luciferase enzyme and were evaluated for their effect on TE.

The 5' UTR of PF3D7_1411400 is 730 nucleotides long, contains 15 uAUGs (13 form uORFs), and is 11.0% GC (Figure 5.3 B). Using the data of Caro *et. al.*[18], the RNA abundance

was measured to be 63.66 reads per million and the $\log_2(\text{TE})$ was -1.94. The 5' UTR of PF3D7_1428300 is 775 nucleotides long, contains 10 uAUGs (all of which form uORFs), and is 9.3% GC (Figure 5.3 B). The abundance for the RNA was measured to be 522.93 reads per million and the $\log_2(\text{TE})$ was 1.75. Thus, the TE of the active gene is 12.2-fold higher than that of the repressed gene by ribosome profiling. In the *P. falciparum* *in vitro* translation assay, which effectively removes any influence from differential expression levels, the signal produced by the activating 5' UTR was 24.5-fold higher than the signal from the repressive 5' UTR (Figure 5.3 B). In the K562 *in vitro* translation assay, the 5' UTR from the active gene also out-performed that of the repressed gene by 5.3-fold (Figure 5.3 C). Both *in vitro* translation assays recapitulated the difference in TE that was observed *in vivo*, albeit with different absolute magnitudes.

As noted above, the 5' UTR analysis of the ribosome profiling data suggested that differences between high and low TE 5' UTRs appeared to be exaggerated closer to the translation start site. To investigate this while reducing the search space for *cis*-acting elements, each of the 5' UTRs was progressively trimmed from the 5' end (Figure 5.3 C). In *P. falciparum* lysates, shortening the activating 5' UTR to 549 nucleotides increased translation 4.2-fold, and reducing the UTR to 130 nucleotides further increased translation 1.9-fold, for a 7.9-fold total increase. Reducing the repressive 5' UTR to 339 nucleotides similarly increased translation 3.15-fold, but further reduction to 130 nucleotides resulted in no additional increases in *P. falciparum*. Similarly, in human K562 lysates, trimming of the 5' UTRs resulted in an overall increase in translation for both 5' UTRs and increased the TE differential between the two (Figure 5.3 B).

While trimming both 5' UTRs increased their respective translation, the differential between the activating and repressive UTRs was magnified. At 130 nucleotides, the activating 5'

UTR outperformed the repressive 5' UTR by 64-fold (Figure 5.3 B), which had the added benefit of increasing the dynamic range between constructs. Hence forth, the minimal 130 nucleotide sequences were used as the platform for further dissection of *cis*-acting sequences and all subsequent 5' UTRs evaluated were 130 nucleotides. The activating 130 nucleotide 5' UTR derived from PF3D7_1428300 is denoted as A[WT] and the repressive 130 nucleotide 5' UTR from PF3D7_1411400 is denoted as R[WT]. Reflective of the distinct distributions in uAUG abundance and GC abundance, R[WT] is 16.9% GC and contains four uAUGs, numbered 1-4 based on distance from the translation start site. uAUGs 1 and 2 do not form uORFs and are in the +1-frame relative to the reporter gene starting at -13 and -22 nucleotides, while uAUGs 3 and 4 both form uORFs at -66 and -101 nucleotides. A[WT] is 7.7% GC and contains no upstream "AUG"s (Figure 5.3 D).

All the RNAs used herein were capped using Vaccinia Capping Enzyme (NEB M2080S). To verify that both lysates were sensitive to capping, capped and uncapped versions of the full length 5' UTRs and the 130 nucleotide 5' UTRs were compared (Figure 5.4). Both lysates were sensitive to capping, with capped RNAs generally generating more luminescence (up to a 21.7-fold increase in *P. falciparum* and 7.1 in K562 with full length 1429300), especially in *P. falciparum* lysates. Additionally, in K562 lysates, uncapped RNAs with the full length 5' UTRs generated a more variable signal than capped RNAs. To promote scanning initiation, increase luminescence signal, and reduce noise, all further experiments in this study utilized capped RNA.

5.4.3 Measurement of both independent and combined effects of uAUGs on translational repression

The combined effect of the four uAUGs in R[WT] was first evaluated by mutating all four to "AUC", denoted R[Δ 1 Δ 2 Δ 3 Δ 4]. Conversion of all four alleviated repression by over

1000% in *P. falciparum*, and 337% in human lysates (Figure 5.5 A). If each uAUG equally contributed toward repression, the expected result of maintaining any single uAUG would be a consistent relief from repression relative to R[WT]. However, individually maintaining each of the four uAUGs yielded significantly different degrees of translation (Figure 5.5 B), ranging from a modest 2-fold increase with uAUG-3 alone (R[$\Delta 1\Delta 2\Delta 4$]) to a nearly 10-fold increase with uAUG-1 alone (R[$\Delta 2\Delta 3\Delta 4$]), indicating unequal contributions towards the overall level of repression. For K562 extracts, the results were similar, although uAUG-2 alone (R[$\Delta 1\Delta 3\Delta 4$]) was the most repressive of the set, being even more so than the wild-type construct. Since uAUG-4 forms a uORF whose stop site overlaps with uAUG-3 and was eliminated by making uAUG-3 into “AUC”, uAUG-4 with a restored uORF was also evaluated (R [$\Delta 1\Delta 2\Delta 3$ -uORF restored]). With the uORF restored, uAUG-4 confers minimal or no translational repression. These data demonstrate that each of the individual uAUGs in isolation possess differing repressive activities with respect to translation.

To further evaluate the repressive effects of uAUGs in a novel context, the four uAUGs from R[WT] were placed into A[WT] at the matching positions (Figure 5.6). As expected, in *P. falciparum*, when all four uAUGs were present A[+1:+2:+3:+4], translation was repressed, 2.9-fold. Additionally, each uAUG individually repressed translation between 1.5-fold and 2.9-fold when the other positions were mutated to “AUC (Figure 5.6). The results in K562 followed the same trends as *P. falciparum*.

To explore potential interactions between uAUGs, pairwise combinations of the uAUGs in R[WT] were evaluated (Figure 5.5 C). If uAUGs possess independent repressive potentials that do not affect each other, the repression by any two uAUGs would be the product of their respective potentials. For example, the two furthest uAUGs, uAUG-1 and uAUG-4, yielded 37%

and 73% of the maximum translation of the derepressed construct R[$\Delta 1\Delta 2\Delta 3\Delta 4$] in *P. falciparum* lysates. Thus, if acting independently, the predicted yield for a 5' UTR containing both uAUGs would equal $0.37 * 0.73$, or 27%, of the maximum signal. The measured signal for this combination (R[$\Delta 2\Delta 3$]) was extremely close to the predicted value, 28.6%, suggesting that these two elements act independently and proportionately on translation. Evaluation of the remaining pairs of uAUGs revealed some notable combinations that likely highlight interacting pairs (Figure 5.7). Of note, the predicted combination of uAUG-3 and uAUG-4 (R[$\Delta 1\Delta 2$]) in *P. falciparum* underestimates the measured amount of translation (11% predicted versus 19% measured), suggesting an interaction between uAUG-4 and uAUG-3, which, as noted previously, marks the end of the uORF formed by uAUG-4. For K562 lysates, constructs containing uAUG-2 differ most from their predicted values, indicating this element may be uniquely sensitive to the presence of the other uAUGs.

Having examined all pair-wise combinations of the four uAUGs, each three-way combination was then evaluated (Figure 5.5 D). Unlike the broad range of differing repressive activities observed for individual and pairwise uAUGs, trios of uAUGs all repressed translation to a similar or greater degree than R[WT]. Together these data indicated that uAUGs in isolation independently confer varying levels of repression; however, multiple uAUGs may combine to produce a concerted effect that was not predicted by their individual contributions.

5.4.4 Investigating the effect of position and termination status on uAUG repression

Each of the uAUGs in R[WT] is distinct with respect to their Kozak context, their position relative to the translation start site, and their termination status. Previous work describing the Kozak context for *P. falciparum* suggests a string of adenosine bases preceding the start site is most commonly observed[28,33]. To assess the effects of uAUG positionality

while maintaining a common Kozak, a cassette comprised of the -3 to +9 sequence from uAUG-3 was individually placed at five equally spaced positions within R[$\Delta 1\Delta 2\Delta 3\Delta 4$] beginning at -14 nucleotides from the reporter protein coding region (Figure 5.8). All cassettes were inserted in the +2 frame such that if translation initiated at these sites, no reporter should be translated in-frame. Two versions of the cassette were created, one maintaining the termination with a stop codon at the end of the cassette and one without (Figure 5.8A). For the five constructs containing a non-terminating uAUG, all potential stop sites proceeding the protein coding region in-frame with the 5' most cassette were eliminated and the effect of these mutations alone in the presence of uAUG-3 (R[$\Delta 1\Delta 2\Delta 4$]*) were evaluated (Figure 5.9).

Except for the -122 position, where the uAUG is 11 nucleotides from the 5' cap, all cassette placements resulted in repression comparable to R[$\Delta 1\Delta 2\Delta 4$] (Figure 5.8 B). Of note, the cassettes placed nearest to the 5' cap had little effect on translation in either *P. falciparum* or K562 lysates (1.2-fold and 1.3-fold repression respectively). For *P. falciparum*, unlike the relative consistency of repression produced by uORF placement, the uAUG equivalent yielded a trend in repression. As the uAUG moved closer to the translation start site the repressive strength increased until maximum repression was achieved when the cassette was placed -41 nucleotides from the translation start site (Figure 5.8 B). In comparison, K562 lysates also yielded peak repression at the -41 position, but the pattern of repression induced by both the uORF and uAUG cassettes were more similar to each other and the trend observed for uAUG cassettes in *P. falciparum*.

Experiments with the same cassettes positioned in-frame to the translation start site, at -15, -42, -69, -96, and -123, were also evaluated (Figure 5.10). In this instance, position similarly appears to regulate the effect of uAUGs. However, at the position closest to the 5' cap, with the

cassette at -123, the cassette was as repressive as closer to the translation start site in both lysates. This could signify that at the 5' end there are additional variables determining if an uAUG represses translation. These experiments indicate that in both *P. falciparum* and K562 lysates, the position of uAUGs contributes in part to downstream repression, however, termination status may also impact this effect, at least in the case of *P. falciparum*.

To further examine the difference between in-frame and out of frame start sites, all the upstream start sites from the full length 5' UTRs of *P. falciparum* were separated by termination status, then frame and plotted by position (Figure 5.11). All non-terminated uAUGs occur within 350 nucleotides of the protein coding region. Interestingly, in-frame non-terminated upstream start sites were less prevalent than out-of-frame upstream start sites (Figure 5.11 A) whereas for uORFs there did not appear to be a bias in frame prevalence. Together with the *in vitro* translation data this further suggests that frame plays a role in uAUG regulation.

5.4.5 Evaluating the effect of GC content on TE

One distinguishing feature of the *P. falciparum* genome is an extreme bias in nucleotide content, especially within the intergenic regions that are ~90% AT [34]. As noted in Figure 1D and 1E, there is a significant difference in the distributions of GC content between the 5' UTRs of genes with high and low TE with repressed genes exhibiting a higher GC bias. These differences are evident within A[WT] and R[WT], which possess 7.7% GC, and 16.9% GC respectively. This GC bias is intensified in the 60 nucleotides closest to the translation start with A[WT] containing only 1.7% GC and R[WT] containing 15% GC (Figure 5.12 D). To investigate the impact of GC content in the context of these two constructs, substitutions were systematically introduced into the proximal region of A[WT] to increase the GC content from 1.7% to a maximum of 30% GC (Figure 5.12 A). Substitutions were maintained between

constructs, no upstream “AUG”s were introduced, and significant secondary structures was avoided (Figure 5.13). In *P. falciparum* lysates, between 1.7% and 20% GC there was no change in TE while at 30% GC translation was repressed 1.5-fold (Figure 5.12 A). The repressive effect of the high GC content was 1.3-fold in human K562 lysates.

The converse experiment of reducing the GC content of R[WT] was also carried out. The GC content in the last 60 nucleotides of R[$\Delta 1\Delta 2\Delta 3\Delta 4$] was reduced to 5% by eliminating all GC content between 4 and 60 nucleotides from the translation start site and to 0% by removing all GC (Figure 5.12 B). A maximum translation increase of approximately 2-fold was observed relative to R[$\Delta 1\Delta 2\Delta 3\Delta 4$], indicating a modest but measurable impact in this context. These results were mirrored in K562 lysates (Figure 5.12 B). Together, the result of manipulating the GC content of the last 60 nucleotides of the 5' UTR suggests that the impact on translation to be subtle, but sensitive to the overall context.

5.4.6 Identifying additional cis-acting regulatory regions within R[WT] and A[WT]

In addition to the study of specific elements predicted to impact TE, a series of systematic sequence swaps were investigated, in which regions from both the 5' and 3' end of R[WT] and A[WT] were exchanged. Beginning with the 3' end of the 5' UTR, 20, 40, and 60 nucleotides were exchanged between R[WT] and A[WT] (Figure 5.14 A and B). In the case of A[WT], introducing more sequence from R[WT] severely impacted TE. While some of this impact was anticipated due to the introduction of uAUG-1 and uAUG-2, additional decreases in translation were observed with sequence beyond these elements (A[60nt 3' R]). Furthermore, the added impact beyond the introduction of uAUGs was observed only with *P. falciparum* lysates. For the converse experiments, exchange of sequence from A[WT] into R[WT] at the 3' end resulted in increased translation (11.7-fold). This increase in translation was in part expected due

to the elimination of uAUG-1 and uAUG-2, however the magnitude of the effect is greater than predicted from the experiments shown in Figure 5.3 C. The effect in human K562 lysates was markedly less with a maximum difference of 1.4-fold.

Sequence exchanges at the 5' end were similarly carried out using 10, 20, and 30 nucleotide swaps between A[WT] and R[Δ1:Δ2:Δ3:Δ4]. The latter construct was chosen over R[WT] to assess the impact in the absence of uAUGs. For *P. falciparum*, exchanging the first 10 nucleotides of R[Δ1:Δ2:Δ3:Δ4] into A[WT] repressed translation 2.6-fold, with a final 3.7-fold repression exchanging 30 nucleotides. (Figure 5.14 C). In contrast, exchanging the first 10 and 20 nucleotides of A[WT] into R[Δ1:Δ2:Δ3:Δ4] activated translation up to 1.9-fold while exchanging 30 nucleotides activated translation 3.5-fold. Note that the level of translation achieved in this latter construct matches the output of A[WT], demonstrating that in the absence of uAUGs, exchanging the sequence elements within the first 30 nucleotides of the 5' end of the 5' UTR was sufficient to render A[WT] and R[Δ1:Δ2:Δ3:Δ4] approximately equivalent (Figure 5.14 D).

5.5 Discussion

Among eukaryotes, *P. falciparum* presents several distinct features that bear upon translation. First, the AT-rich genome contains frequent poly-adenosine stretches that alone necessitates unique adaptations of the translational machinery to prevent ribosome stalling or frameshifting [35-36]. Additionally, there are a limited number of ribosomal RNA copies within the genome, each with stage specific expression [37-38]. The transcriptome also features unusually long 5' UTRs, the longest in late trophozoites being a remarkable 8229 nucleotides (PF3D7_1139300). Despite these features, previous studies suggest that *P. falciparum* initiates translation in a cap-dependent manner similarly to other eukaryotes [39-40].

While the central initiation factors required for cap-binding have been bioinformatically identified and many of the essential interactions have been validated, questions remain around how these factors regulate translation initiation given *P. falciparum*'s unique 5' UTR features [26,41]. Additionally, ribosome profiling has demonstrated that translation is an integral point of regulation for model eukaryotes [42,43], but for *P. falciparum* it reveals that less than 10% of transcripts are translationally regulated. Directly evaluating how these unusual mRNA features function in *P. falciparum* could reveal unique mechanisms that would be powerful therapeutic targets.

A re-analysis of ribosome profiling data highlights two important features that differ between mRNAs at the top and bottom of the TE range. As shown in Figure 1, the presence of uAUGs and GC content are significantly different between highly translated and poorly translated mRNAs, a difference that appears exacerbated by proximity to the protein coding region. To explore and dissect the role of these features, two representative 5' UTRs were chosen from the top and bottom deciles, the 5' UTRs of PF3D7_1411400 and PF3D7_1428300. The differences in TE driven by these two 5' UTRs were faithfully recapitulated using *in vitro* translation extracts generated from late trophozoites of *P. falciparum* W2 strain (Figure 5.3) and human K562 cells. Surprisingly, these differences were maintained when using only the proximal 130 nucleotides from each 5' UTR, with A[WT] derived from PF3D7_1428300 and R[WT] from PF3D7_1411400. These two 130-nucleotide 5' UTRs provided an ideal platform to evaluate the effects of uAUGs and GC content.

uAUGs have long been appreciated as translational regulatory elements, and work by Marilyn Kozak demonstrated their repressive abilities in the early 1980s [20]. However, it remains difficult to predict the individual or joint repressive activities of uAUGs from sequence

context alone, especially for non-model organisms. Additionally, it is unusually to have uAUGs so abundant throughout the transcriptome. Here, a reductionist approach was used to individually assess the repressive potential of each uAUG within R[WT] in isolation, and in combination (Figure 5.5). For many pairs, such as uAUG-1 and uAUG-4, the combined activity directly reflected a combination of each uAUG's repressive strength. For others, like uAUG-3 and uAUG-4, it was revealed that the combined effect of two uAUGs could be reduced by their interaction. Since uAUG-3 is itself the in-frame stop site for uAUG-4, it reasonable to assume that the termination of uAUG-4 may interfere with initiation events at uAUG-3. These interactions make it difficult to predict the impact of multiple uAUGs without direct measurements as performed here.

The sequence context surrounding an “AUG” is essential for determining the rate of initiation at that site [11, 44-45], however, additional elements may affect the regulatory activity of an uAUG. Here, two possible modifiers were examined in detail, namely, the position of uAUGs relative to the protein coding region, and whether it forms a uORF (Figure 5.8 and 5.10). Both the position and termination status affect translation with the most dramatic result arising when the uAUG is positioned furthest from the protein coding region, only 11 nucleotides from the 5' cap. At this distance neither the open uAUG nor the uORF repressed translation. One caveat of this study is that only one putative uORF was assessed. It is likely that the length and composition of the uORF sequence itself may modify the overall impact.

Along with uAUG frequency, bioinformatic analysis of the 5' UTR sequences from *P. falciparum* also reveals a statistically significant difference in GC content, with higher GC content corresponding to lower TE. While higher GC content could correlate with higher secondary structures, we wanted to evaluate if GC content alone could regulate translation.

Surprisingly, the results of manipulating GC content proximal to the protein coding region in the context of only these two chosen UTRs yielded corresponding changes in the predicted direction, albeit with small magnitudes when compared to the impact of uAUGs. In the active context, translation became repressed relative to A[WT] at 30% GC content within 60 nucleotides of the translational start. Within this 60-nucleotide region, only 31 (1.4%) of the 2088 5' UTRs from *P. falciparum* expressed in late trophozoites evaluated here are 30% GC or above (Figure 5.1 A). Thus, few genes would be predicted to be impacted by these shifts in GC content alone. Eliminating GC content from the last 60 nucleotides of R[Δ1:Δ2:Δ3:Δ4] resulted in modest increases in TE (Figure 5.13). In this case, of the 2088 5' UTRs 273 (13.1%) are 5% or below within this region and 16 (0.8%) are 0%.

Finally, to examine the effects of the sequences within A[WT] and R[WT]/R[Δ1:Δ2:Δ3:Δ4] on translation, segments from the 5' and 3' ends were progressively exchanged between them (Figure 5.14). Sequence exchanges at the 3' end of the 5' UTR removed or introduced uAUGs, which resulted in the expected increases or decreases in TE respectively. We note that in each case, exchanged sequence beyond the uAUGs also impacted TE in *P. falciparum*, suggesting additional context within these regions. Sequence exchanges at the 5' end were more impactful than would have been predicted. Specifically, 30 nucleotides of A[WT], when substituted into R[Δ1:Δ2:Δ3:Δ4], suggest a possible sequence with a role in regulating the rate of translation initiation.

As an essential pathway throughout the parasite's life cycle, protein synthesis is an attractive therapeutic target. However, since the mechanisms of eukaryotic translation are highly conserved, potential therapeutics must cross the challenging bar of being highly specific to *P. falciparum*. Here, *in vitro* translation was used to allow for direct comparison between *P.*

falciparum and human to identify unique effects on TE. Despite the large evolutionary distance between the two organisms, *P. falciparum* and K562 lysates yielded highly similar results in the context of the two short model UTRs used here. For developing therapeutics targeting translation initiation, avoiding host effects will be challenging, but *in vitro* translation can continue to be a valuable tool to directly measure differences between *Plasmodium* and humans [46].

Finally, this work continues the task of uncovering the complexity of 5' UTR *cis*-acting regulatory elements and their impact on TE in eukaryotes. *In vitro* translation has previously revealed the importance of the Kozak consensus sequence and uAUGs in model eukaryotes, such as *Saccharomyces cerevisiae* and mammalian cultures [21, 47-49], while higher throughput selection and machine learning techniques have been used to probe the effect of 5' UTR *cis*-acting elements in these same systems [24, 50]. However, working with non-model organisms such as *P. falciparum* poses unique challenges, such that many of these techniques cannot be readily utilized for comparative analysis. The highly reductionist approach taken here has the benefit of allowing specific and systematic hypotheses to be tested, although it is clear that higher throughput methods will be required to generalize these findings beyond these specific examples.

Conclusions

Cis-acting features within the 5' UTRs of eukaryotes regulate the TE of a given gene. While specific examples have previously been evaluated in model eukaryotes, *P. falciparum* possesses unusual 5' UTR characteristics, such as length, base content, and high uAUG prevalence, that suggest *cis*-acting upstream elements play a significant role in tuning translational efficiencies. Through extensive dissection of exemplar 5' UTRs from *P. falciparum*, we measure the individual impacts of each putative element while comparing these same

constructs in human lysates. The impact of these elements was found to be surprisingly similar in both systems. Since, unlike humans and most other studies eukaryotes, long 5' UTRs featuring multitudes of uAUGs are common in *P. falciparum*, the precise configuration of these elements may have evolved to tune translation levels in this organism where other post-transcriptional regulatory mechanisms may be absent.

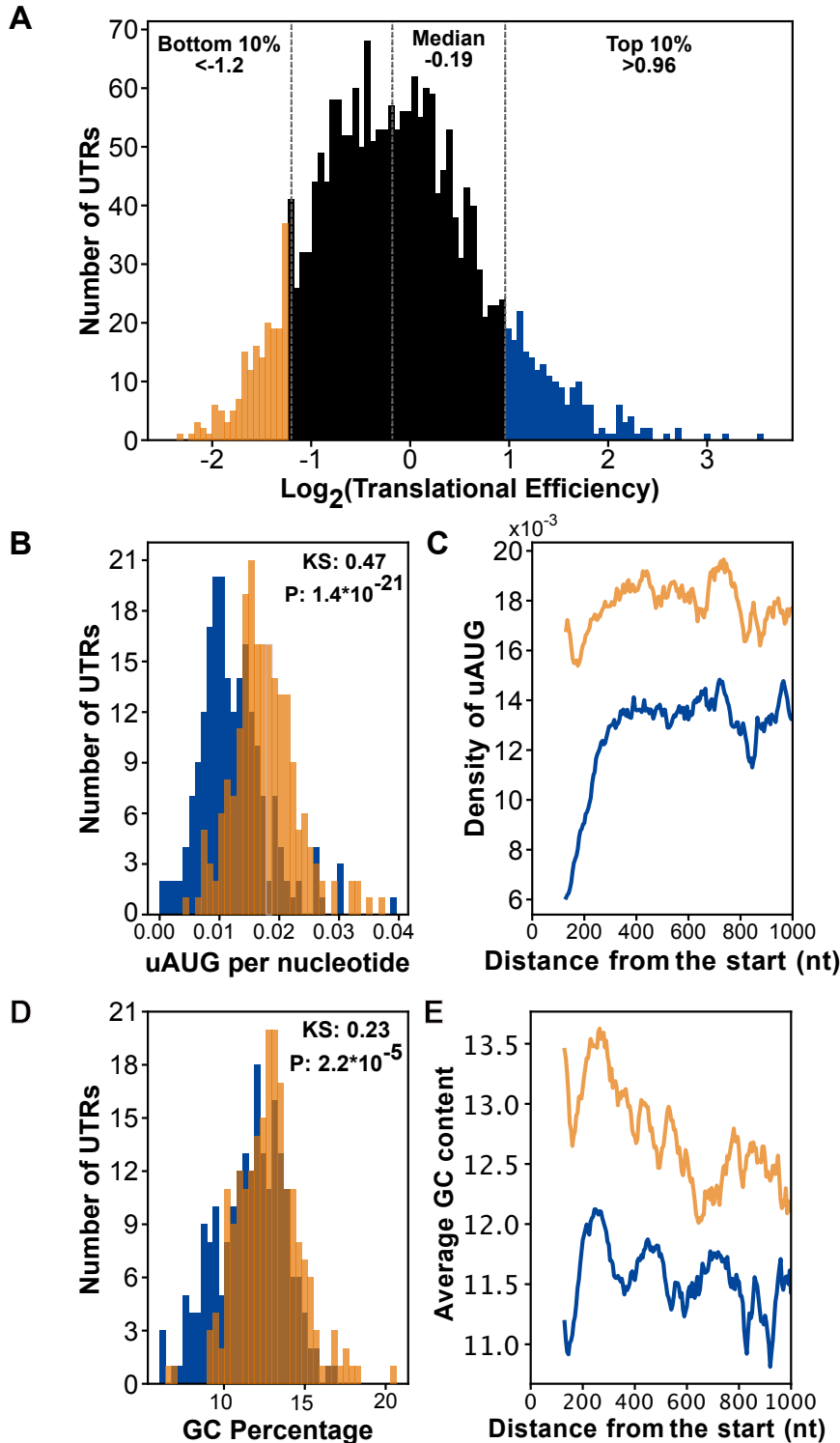


Figure 5.1 Comparison of features within the 5' UTRs of genes in the bottom 10% (n=209) and top 10% (n=209) of TEs

Comparison of features within the 5' UTRs of genes in the bottom 10% (n=209) and top 10% (n=209) of TEs in the late trophozoite stage using data from Caro and Ahyong et. al. 2014 (18).

a) A histogram of the log₂(TE)s of genes expressed in the late trophozoite stage included in

subsequent analysis. The vertical dotted lines indicate the bottom 10% (yellow) and top 10% (blue) of 5' UTRs. b) The number of uAUGs normalized to the length of the 5' UTRs in the bottom 10% (yellow) and top 10% (blue) of TEs in the late trophozoite stage. The two distributions are statistically distinct, KS test-statistic 0.47, p-value 1.4×10^{-21} . c) The average number of uAUGs in the 5' UTRs within a 130-nucleotide window sliding by 5 nucleotides up to 1000 nucleotides of the bottom 10% (yellow) and top 10% blue. d) The distribution of GC content in the bottom 10% (yellow) and top 10% (blue) of TEs in the late trophozoite stage are statistically distinct, KS test statistic comparison of the two: 0.23 p-value 2.24×10^{-5} . e) The average GC content within a 130-nucleotides sliding window moving 5 nucleotides up to 1000 nucleotides from the translation start site. Bottom 10% (yellow) and top 10% blue.

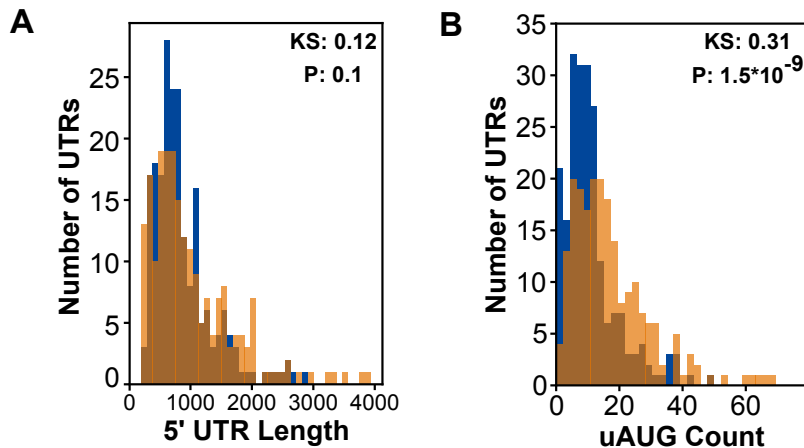


Figure 5.2 Further comparison of 5' UTR features of genes in the bottom 10% and top 10% of TEs

Further comparison of 5' UTR features of genes in the bottom 10% and top 10% of TEs in the late trophozoite stage using data from Caro and Ahyong et. al. 2014 (18) a) Distributions of the 5' UTR lengths from genes with high (blue) or low (yellow) TE. KS test statistic comparison of the two: 0.12 p-value 0.1. b) Distributions of the total number of uAUGs in the 5' UTRs from genes with high (blue) or low (yellow) TE. KS test statistic comparison of the two: 0.31 p-value 1.5×10^{-5} .

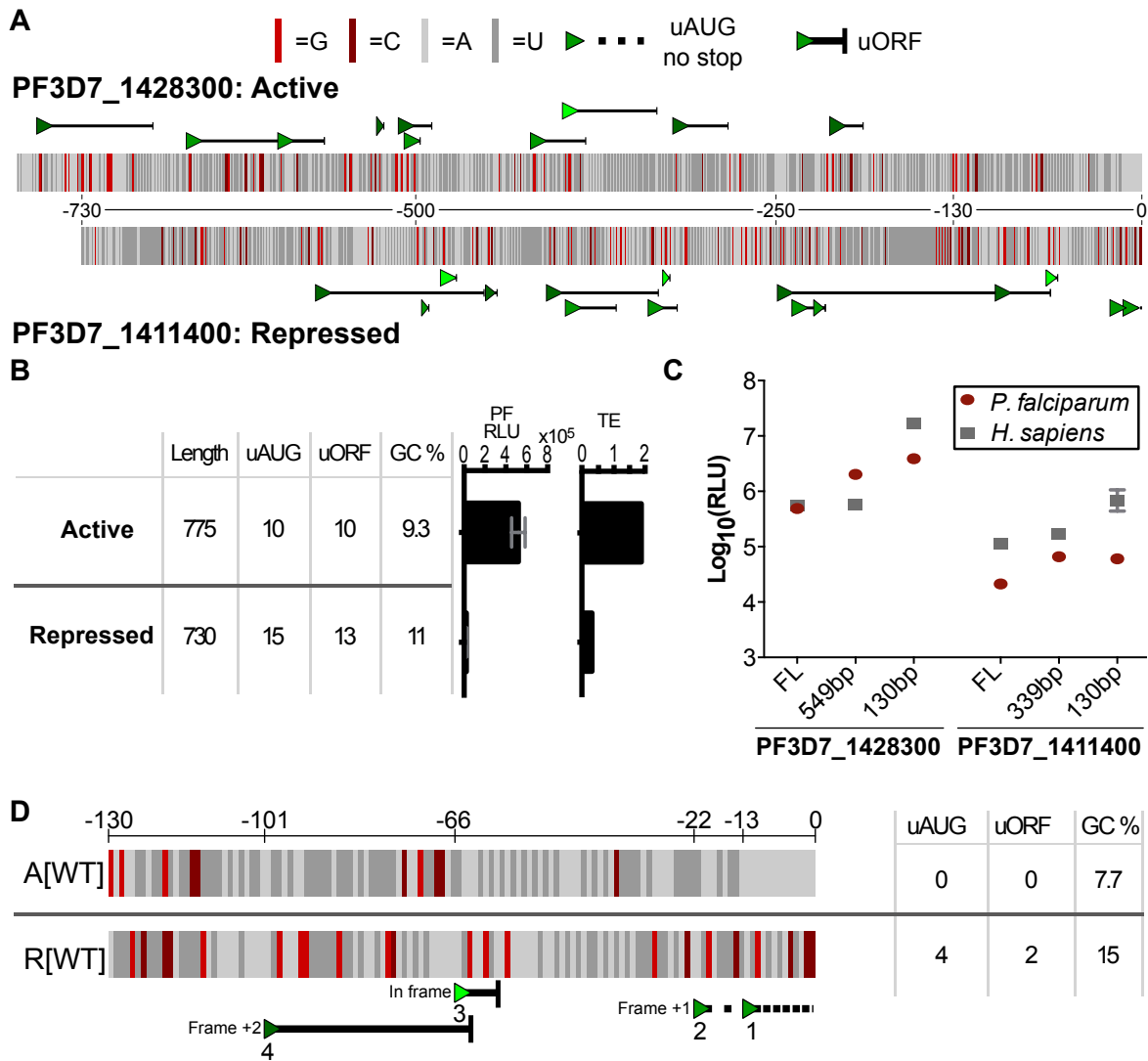


Figure 5.3 130 nucleotides of the 5' UTR from a translationally active (PF3D7_1428300) and repressed gene (PF3D7_1411400) were sufficient to drive distinct TE.

a) The diagrammed sequence of the full length 5' UTRs from active PF3D7_1428300 and repressed PF3D7_1411400. uAUGs are marked by green triangles with the different shades representing the three frames. The numbers between the two construct diagrams mark distance from the protein coding region. b) The lengths, uAUG count, uORF count, GC content, and translational efficiency (TE) for the chosen 5' UTRs and genes obtained from the previously published ribosome profiling and mRNA sequencing (18) with the raw luminescence signal (PF RLU) produced by these 5' UTRs driving NanoLuc (Promega) expression using *P. falciparum* *in vitro* translation. c) Log₁₀(luminescence) from NanoLuc produced by 5' UTRs of decreasing length *in P. falciparum* lysates (red) and K562 lysates (grey). The different lengths were generated by shorting the 5' UTRs from the 5' end. d) Sequence comparison of the 130 nucleotides closest to the protein coding region of the 5' UTRs from PF3D7_1411400 (R[WT]) and PF3D7_1428300 (A[WT]). The four uAUGs in R[WT] are labeled with the green triangles. uAUGs without in-frame stops are followed by a dotted line while uORF forming uAUGs are followed by a solid line with the stop is marked by a vertical line. The four uAUGs are labeled 1-4 based on their distance from the protein coding start site.

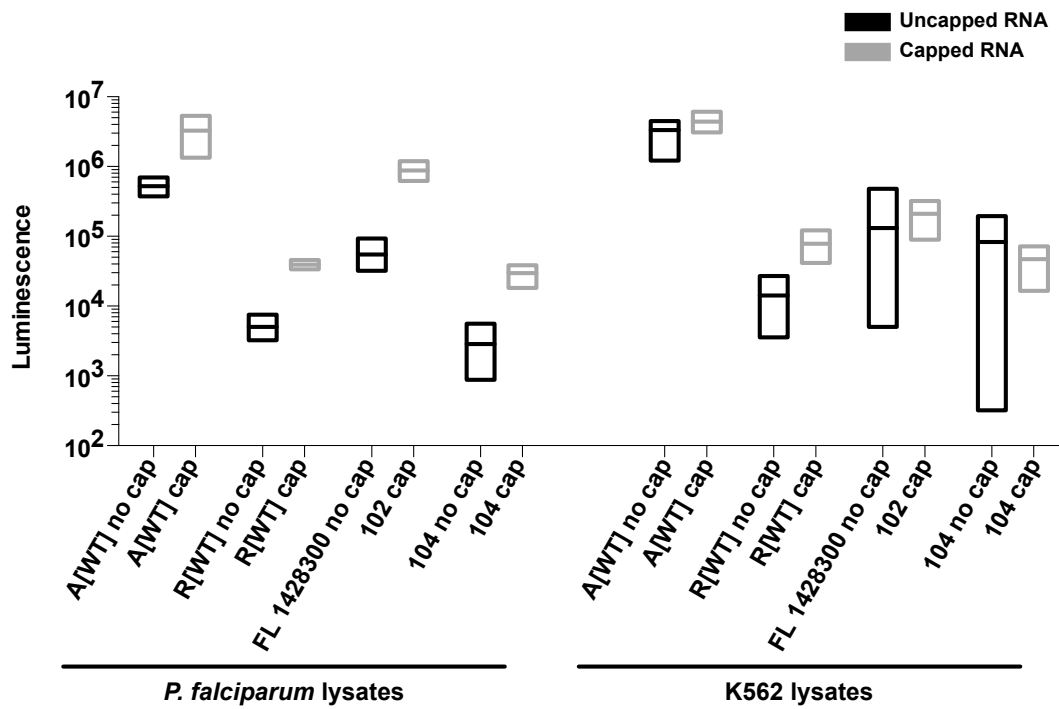


Figure 5.4 Comparison of uncapped and capped RNAs in both *in vitro* assays

The raw luminescence signal from capped and uncapped RNAs in *P. falciparum* and K562 *in vitro* translation.

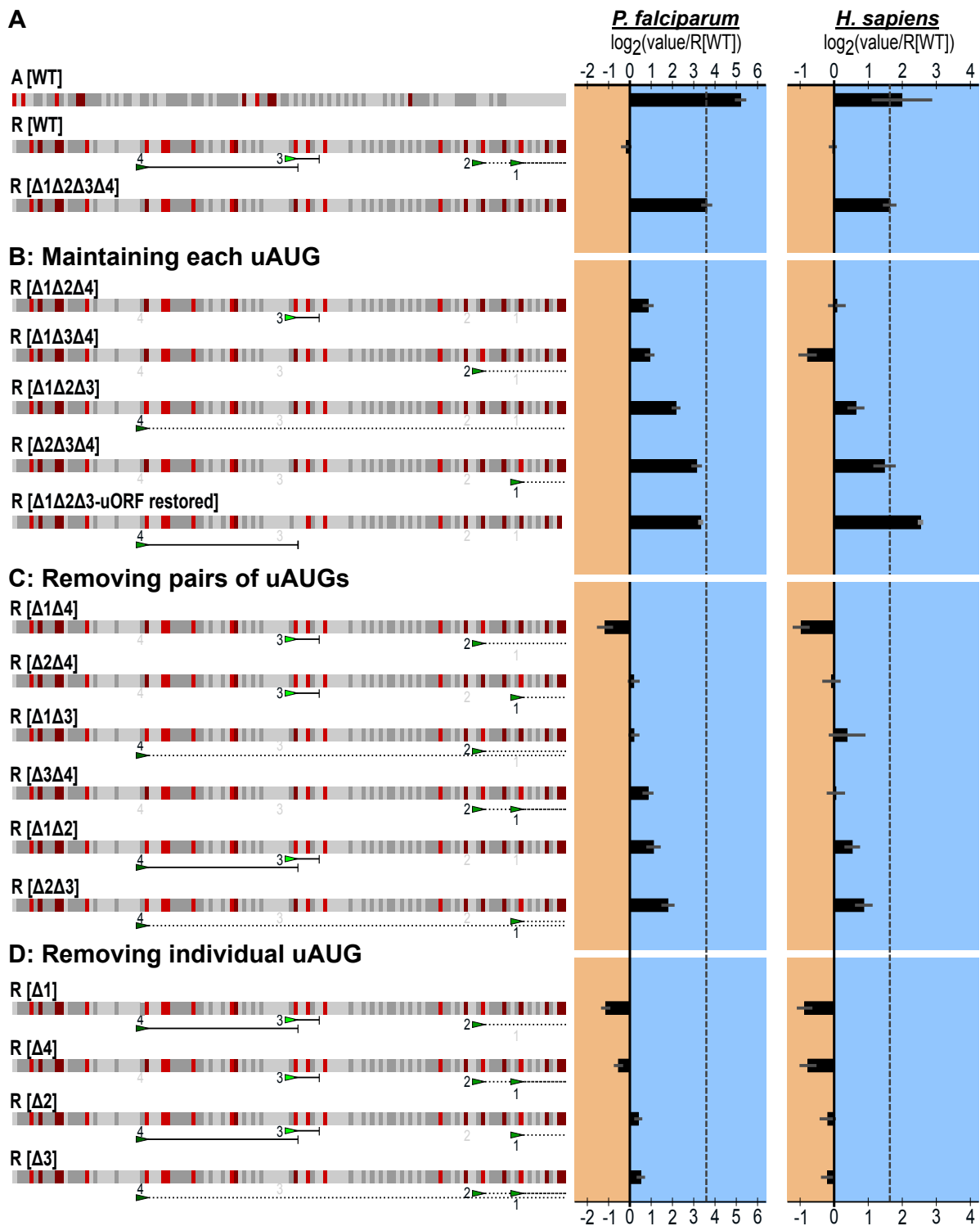


Figure 5.5 Dissecting the effects of the four uAUGs in R[WT].

uAUGs were found to have a generally repressive effect on TE that can be dependent on the presence each other. Graphed for each is the average and SEM of log₂(each experimental value normalized to experimental R[WT] mean). The dotted line marks the average log₂(R[$\Delta 1\Delta 2\Delta 3\Delta 4$] normalized to R[WT]). For each figure, to the left is a diagram of the sequences using the same annotations as Figure 2C. To the right of the diagrams are the results

for *P. falciparum* and human K562s. a) The effect of removing all four uAUGs from R[WT]. b) The effect of retaining a single uAUG. c) The effect of removing each uAUG individually. d) The effect of removing two uAUGs in combination.

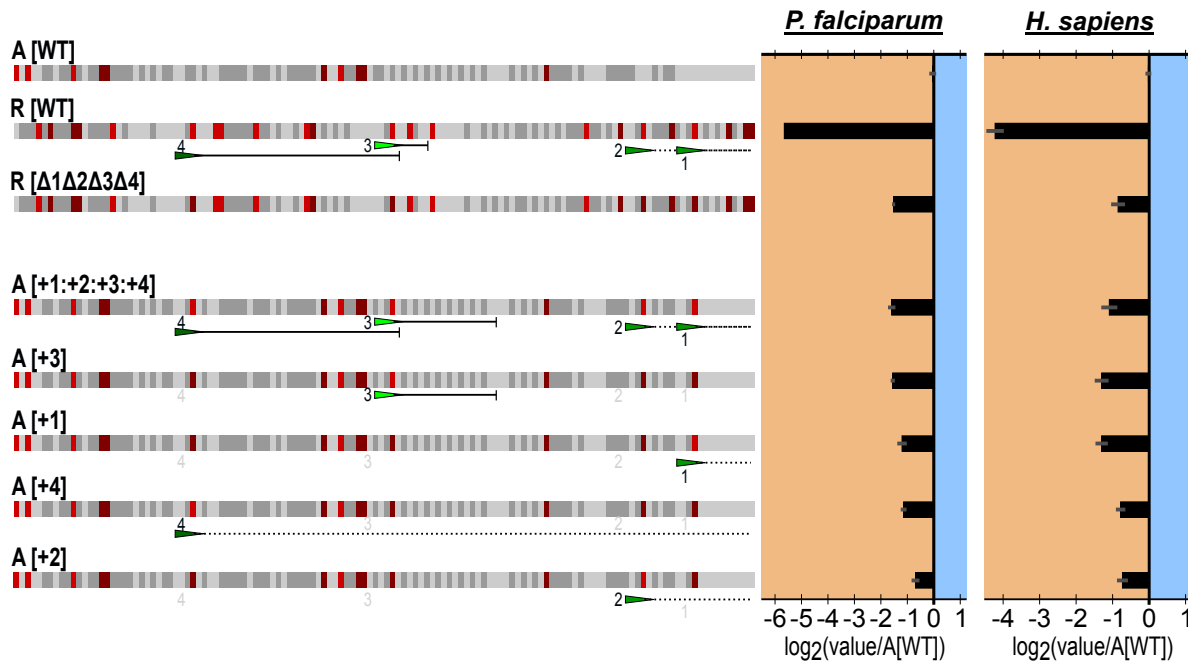


Figure 5.6 uAUGs from R[WT] exchanged into A[WT] at the same positions

The 4 uAUGs from R[WT] exchanged into A[WT] at the same positions showing that the repressive effect is conferrable to other contexts. Graphed for each is the average and SEM of log₂(each experimental value normalized to the experimental average of A[WT]).

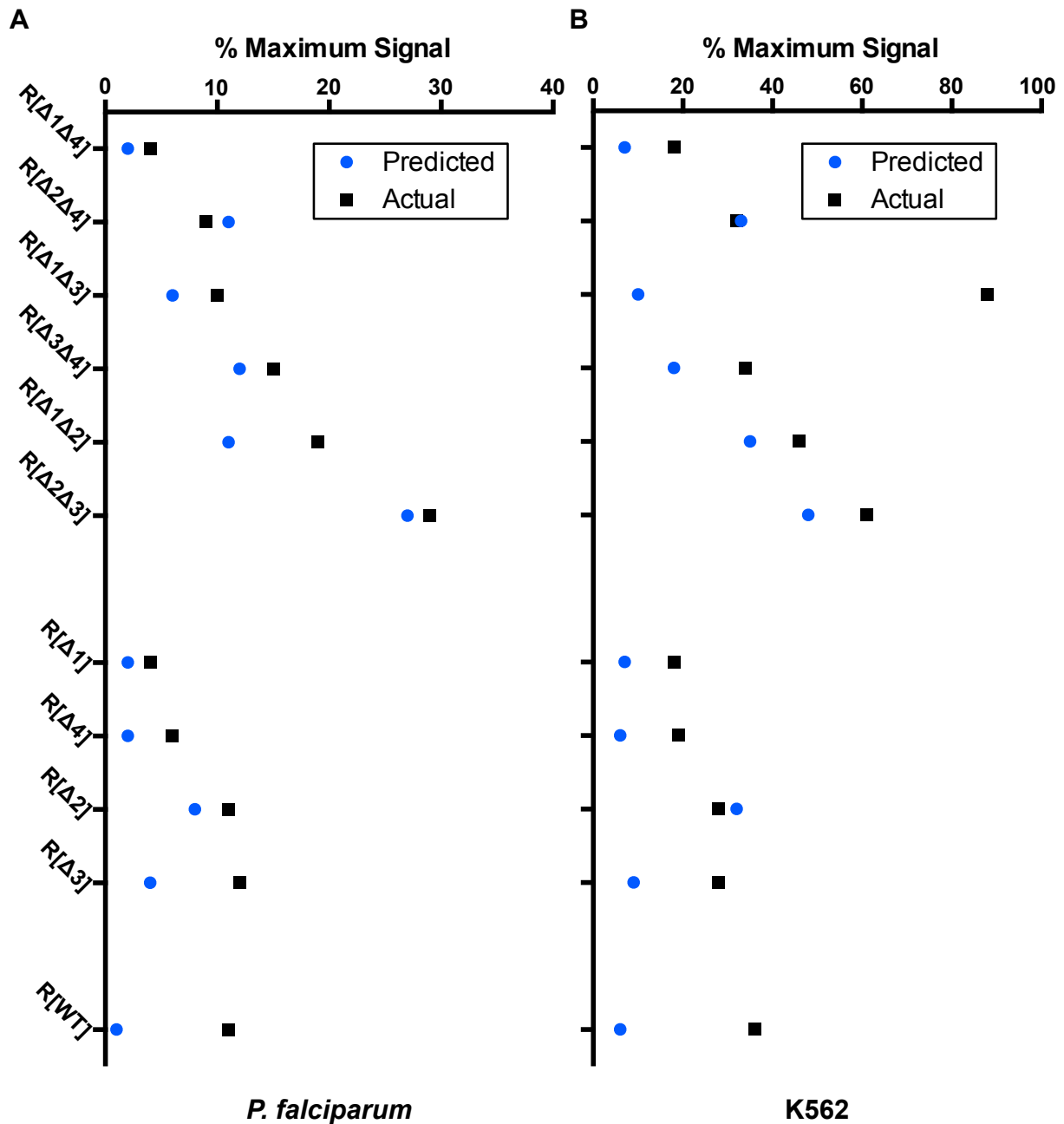


Figure 5.7 Predicted repressive effect of combinations of the uAUGs in R[WT]
 Predicted repressive effect of combinations of the uAUGs in R[WT] based on their individual activities for a) *P. falciparum* and b) K562.

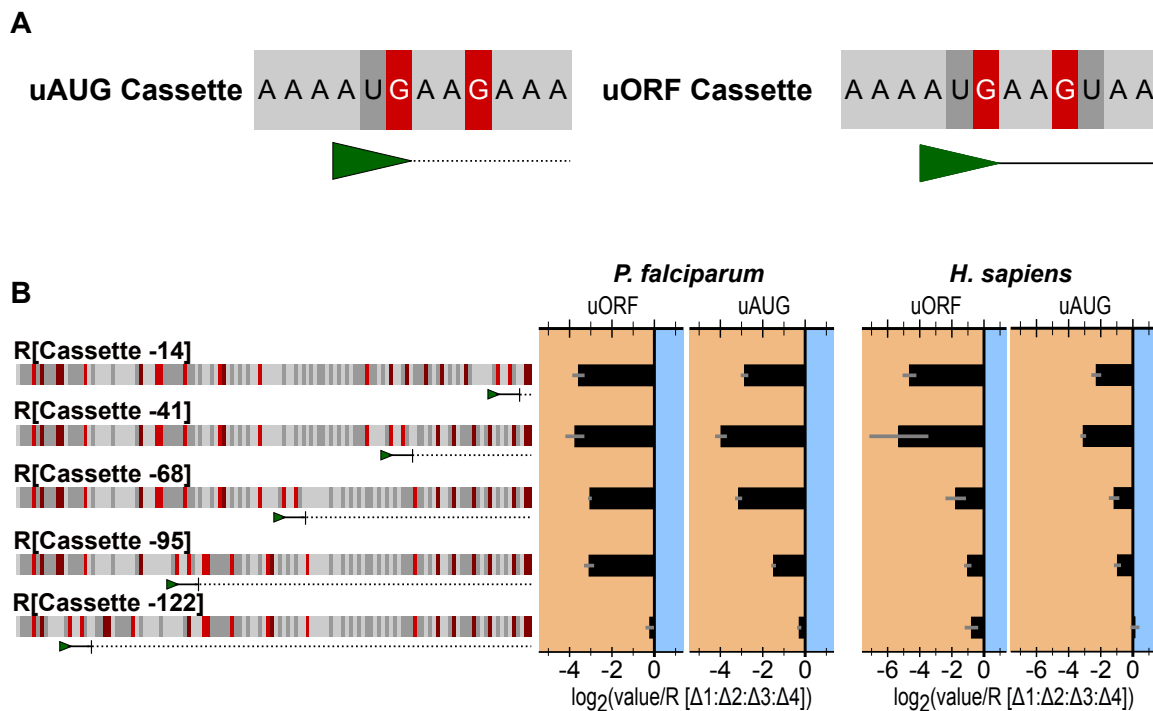


Figure 5.8 Effect of equally spaced and out of frame, non-terminated uAUGs or uORFs on TE

a) Sequence diagram of the two cassettes inserted into R[Δ1:Δ2:Δ3:Δ4] at 5 different positions. The green arrows mark the uAUGs, the solid line indicates the length of the uORF, and the dotted line marks the sequence downstream of the non-terminated uAUG. b) The sequence diagrams to the left represent the 5' UTRs containing the uORF cassette. To the right the uORF cassette and the non-terminated cassette are presented side by side. The left set is from *P. falciparum* lysates while the right is from human. Graphed for each is the average and SEM of $\log_2(\text{each experimental value/ experimental mean of R}[\Delta 1:\Delta 2:\Delta 3:\Delta 4])$.

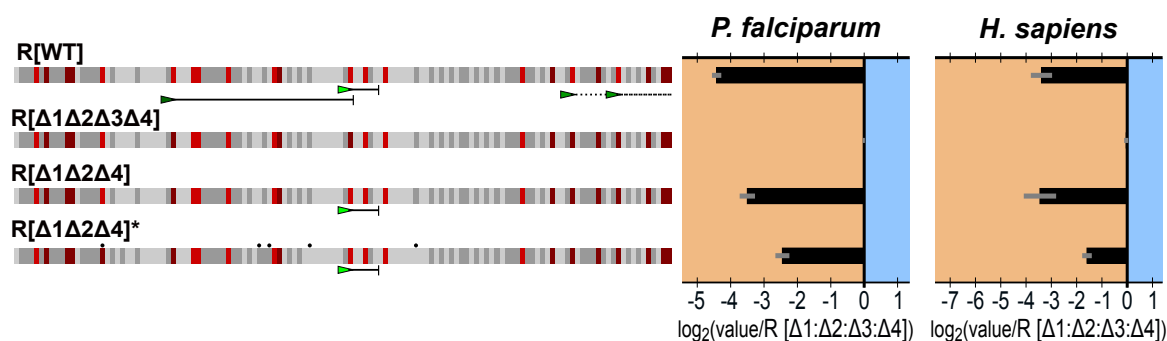


Figure 5.9 Effect of point mutations in R[Δ1:Δ2:Δ4]*

a) To eliminate all downstream stop sites for moving the out of frame non-terminated uAUG, 6-point mutations had to be added to the 5' UTR. R[Δ1:Δ2:Δ4]* was made with those point mutations to compare to R[Δ1:Δ2:Δ4]. Graphed for each is the average and SEM of $\log_2(\text{each triplicate value/ average of R}[\Delta 1:\Delta 2:\Delta 3:\Delta 4])$ experimental triplicates)

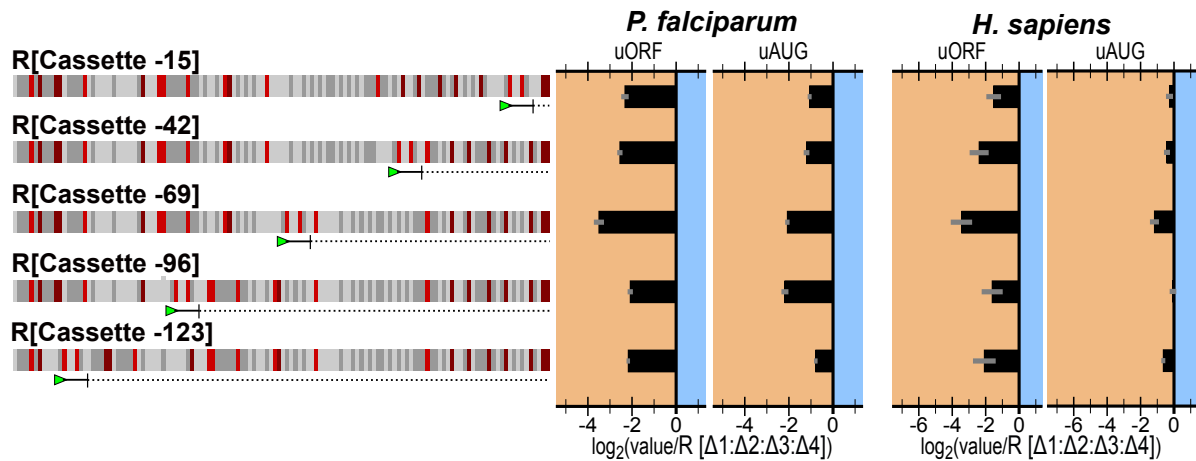


Figure 5.10 Effect of equally spaced and in-frame, non-terminated uAUGs or uORFs on TE

a) Sequence diagram of the two cassettes inserted into R[Δ1:Δ2:Δ3:Δ4] at 5 different positions. The green arrows mark the uAUGs, the solid line indicates the length of the uORF, and the dotted line marks the sequence downstream of the non-terminated uAUG. b) The sequence diagrams to the left represent the 5' UTRs containing the uORF cassette. To the right the uORF cassette and the non-terminated cassette are presented side by side. The left set is from *P. falciparum* lysates while the right is from human. Graphed for each is the average and SEM of $\log_2(\text{each experimental value/ experimental mean of R}[\Delta 1:\Delta 2:\Delta 3:\Delta 4])$.

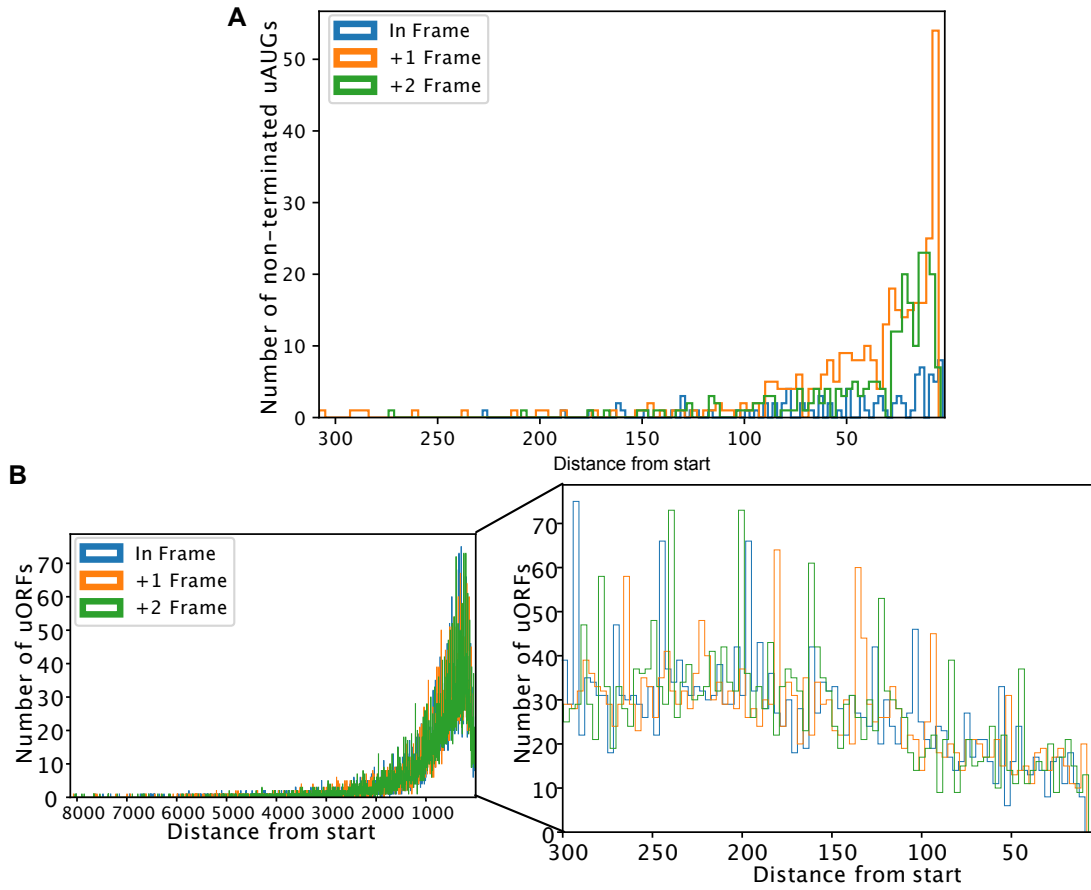


Figure 5.11 Position of all upstream start sites within the 5' UTRs from late trophozoites
 a) The position from the protein coding start site of all non-terminated uAUGs within the 5' UTRs from late trophozoites
 b) The position from the protein coding start site of all terminated uAUGs (uORFs) within the 5' UTRs from late trophozoites

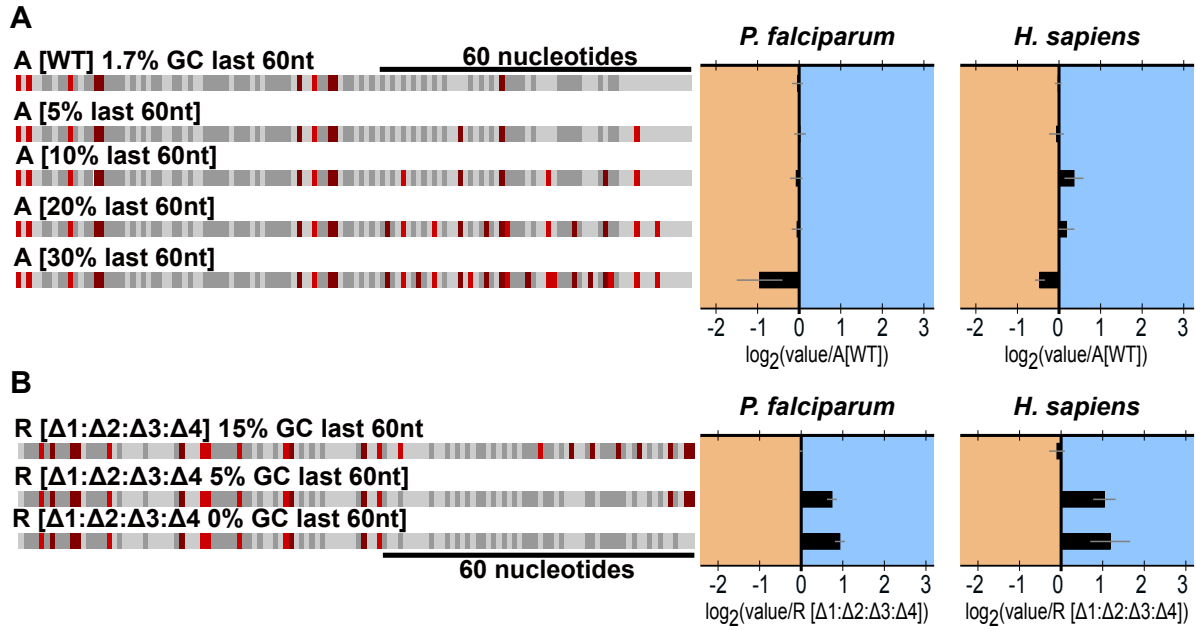


Figure 5.12 Evaluating the effect of GC content on translation

a) Increasing GC content in A[WT]. Graphed for each is the average and SEM of $\log_2(\text{each experimental value}/ \text{experimental mean of A[WT]})$. b) eliminating GC content in R[$\Delta 1:\Delta 2:\Delta 3:\Delta 4$]. Graphed for each is the average and SEM of $\log_2(\text{each experimental value}/ \text{experimental mean of R}[\Delta 1:\Delta 2:\Delta 3:\Delta 4])$

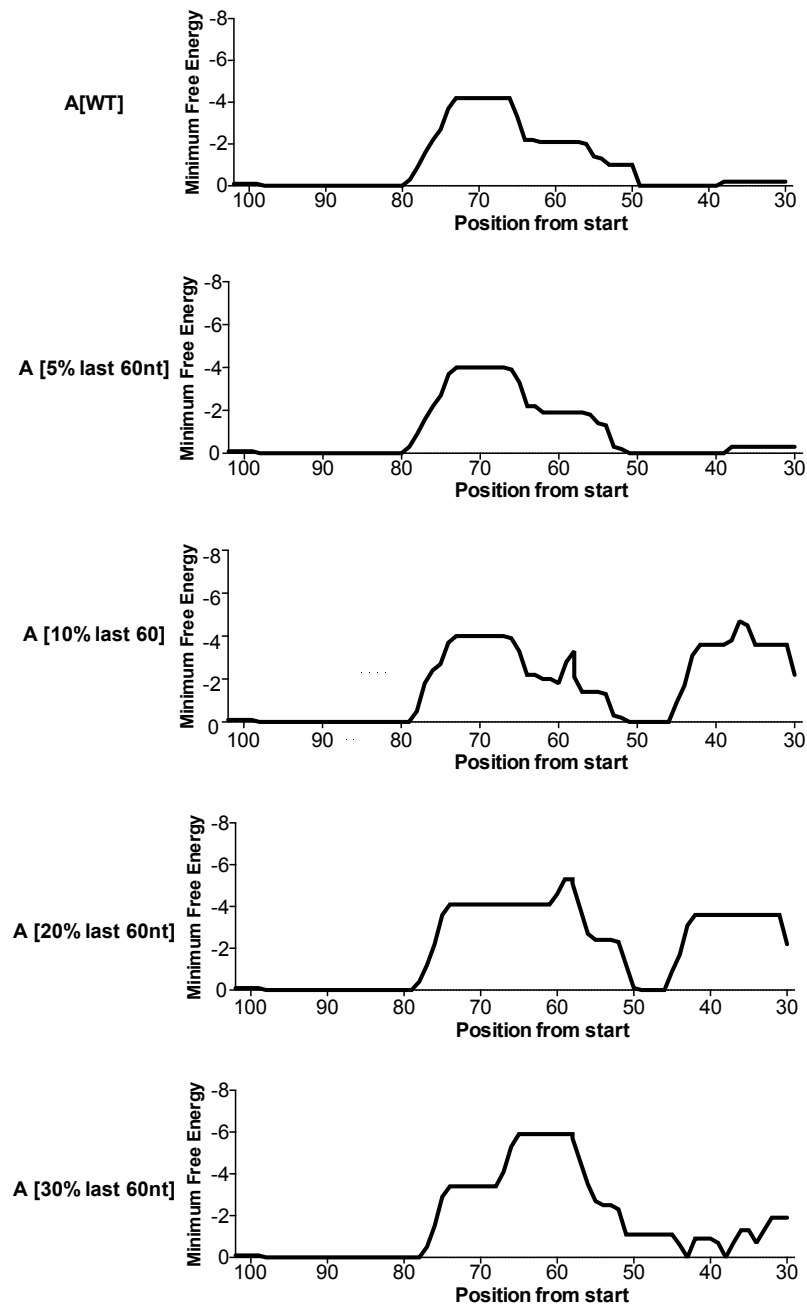


Figure 5.13 Predicted secondary structure when changing CG content

The predicted free energy of the secondary structure with in a 30-nucleotide sliding window moved by 1 nucleotide across the 5' UTRs used to evaluate the effect of GC content.

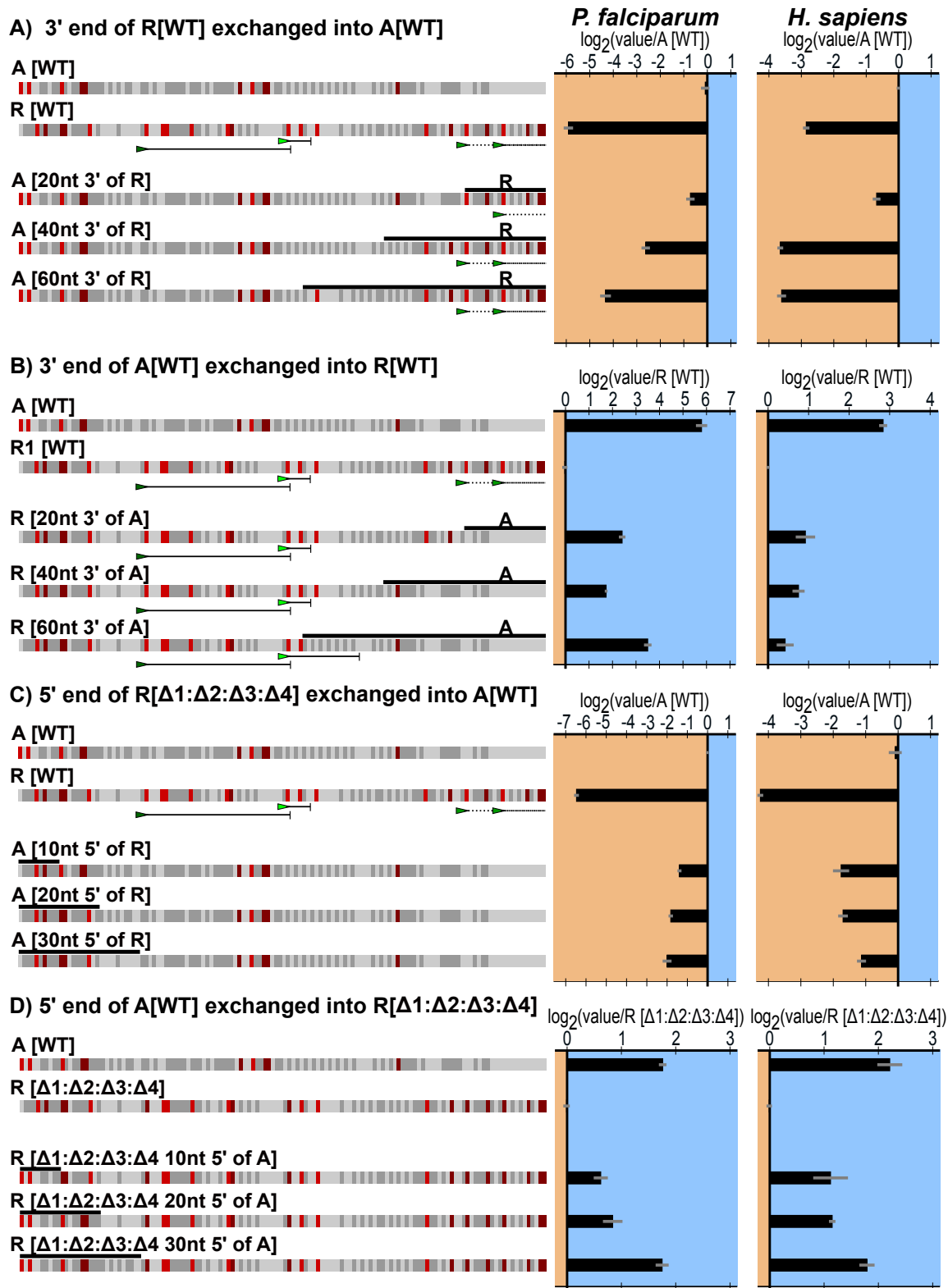


Figure 5.14 Evaluating the effects of the ends of the 5' UTRs on translation

a) Swapping the 3' end of R[WT] into A[WT] Graphed for each is the average and SEM of $\log_2(\text{each experimental value} / \text{mean experimental A[WT]})$. b) swapping the 3' end of A[WT] into R[WT]. Graphed for each is the average and SEM of $\log_2(\text{each experimental value} / \text{mean experimental R[WT]})$.

experimental R[WT]). c) swapping the 5' end of R[$\Delta 1:\Delta 2:\Delta 3:\Delta 4$] into A[WT]. Graphed for each is the average and SEM of $\log_2(\text{each experimental value} / \text{mean experimental of A[WT]})$. d) swapping the 5' end of A[WT] into R[WT]. Graphed for each is the average and SEM of $\log_2(\text{each experimental value} / \text{mean experimental R}[\Delta 1:\Delta 2:\Delta 3:\Delta 4])$.

Chapter 5 References

1. World Malaria Report 2019. <https://www.who.int/publications-detail/world-malaria-report-2019> (2019).
2. Wicht, K. J., Mok, S. & Fidock, D. A. Molecular Mechanisms of Drug Resistance in *Plasmodium falciparum* Malaria. *Annu. Rev. Microbiol.* **74**, 431–454 (2020).
3. Mathieu, L. C. et al. Local emergence in Amazonia of *Plasmodium falciparum* k13 C580Y mutants associated with *in vitro* artemisinin resistance. *eLife* **9**, e51015 (2020).
4. Imwong, M. et al. The spread of artemisinin-resistant *Plasmodium falciparum* in the Greater Mekong subregion: a molecular epidemiology observational study. *The Lancet Infectious Diseases* **17**, 491–497 (2017).
5. Sheridan, C. M., Garcia, V. E., Ahyong, V. & DeRisi, J. L. The *Plasmodium falciparum* cytoplasmic translation apparatus: a promising therapeutic target not yet exploited by clinically approved anti-malarials. *Malaria Journal* **17**, 465 (2018).
6. Baragaña, B. et al. A novel multiple-stage antimalarial agent that inhibits protein synthesis. *Nature* **522**, 315–320 (2015).
7. Saint-Léger, A., Sinadinos, C. & Ribas de Pouplana, L. The growing pipeline of natural aminoacyl-tRNA synthetase inhibitors for malaria treatment. *Bioengineered* **7**, 60–64 (2016).
8. Hoepfner, D. et al. Selective and Specific Inhibition of the *Plasmodium falciparum* Lysyl-tRNA Synthetase by the Fungal Secondary Metabolite Cladosporin. *Cell Host Microbe* **11**, 654–663 (2012).
9. Zhou, J. et al. Inhibition of *Plasmodium falciparum* Lysyl-tRNA synthetase via an anaplastic lymphoma kinase inhibitor. *Nucleic Acids Research* **48**, 11566–11576 (2020).

10. Ah Yong, V. et al. Identification of *Plasmodium falciparum* specific translation inhibitors from the MMV Malaria Box using a high throughput *in vitro* translation screen. *Malaria Journal* **15**, 173 (2016).
11. Sonenberg, N. & Hinnebusch, A. G. Regulation of Translation Initiation in Eukaryotes: Mechanisms and Biological Targets. *Cell* **136**, 731–745 (2009).
12. Aylett, C. H. S. & Ban, N. Eukaryotic aspects of translation initiation brought into focus. *Philos. Trans. R. Soc. Lond. B. Biol. Sci.* **372**, (2017).
13. Lind, C. & Åqvist, J. Principles of start codon recognition in eukaryotic translation initiation. *Nucleic Acids Res.* **44**, 8425–8432 (2016).
14. Hinnebusch, A. G. Structural Insights into the Mechanism of Scanning and Start Codon Recognition in Eukaryotic Translation Initiation. *Trends Biochem. Sci.* **42**, 589–611 (2017).
15. Thakur, A., Gaikwad, S., Vijjamarri, A. K. & Hinnebusch, A. G. eIF2 α interactions with mRNA control accurate start codon selection by the translation preinitiation complex. *Nucleic Acids Res.* **48**, 10280–10296 (2020).
16. Vilela, C. & McCarthy, J. E. G. Regulation of fungal gene expression via short open reading frames in the mRNA 5'untranslated region. *Mol. Microbiol.* **49**, 859–867 (2003).
17. Calvo, S. E., Pagliarini, D. J. & Mootha, V. K. Upstream open reading frames cause widespread reduction of protein expression and are polymorphic among humans. *Proc. Natl. Acad. Sci.* **106**, 7507–7512 (2009).
18. Caro, F., Ah Yong, V., Betegon, M. & DeRisi, J. L. Genome-wide regulatory dynamics of translation in the *Plasmodium falciparum* asexual blood stages. *eLife* **3**, e04106 (2014).

19. Zhang, H., Wang, Y. & Lu, J. Function and Evolution of Upstream ORFs in Eukaryotes. *Trends in Biochemical Sciences* **44**, 782–794 (2019).
20. Kozak, M. Selection of initiation sites by eucaryotic ribosomes: effect of inserting AUG triplets upstream from the coding sequence for preproinsulin. *Nucleic Acids Res.* **12**, 3873–3893 (1984).
21. Alghoul, F., Laure, S., Eriani, G. & Martin, F. Translation inhibitory elements from Hoxa3 and Hoxa11 mRNAs use uORFs for translation inhibition. *eLife* **10**, e66369 (2021).
22. Hinnebusch, A. G. Gene-specific translational control of the yeast GCN4 gene by phosphorylation of eukaryotic initiation factor 2. *Mol. Microbiol.* **10**, 215–223 (1993).
23. Gunišová, S., Beznosková, P., Mohammad, M. P., Vlčková, V. & Valášek, L. S. In-depth analysis of *cis*-determinants that either promote or inhibit reinitiation on GCN4 mRNA after translation of its four short uORFs. *RNA* **22**, 542–558 (2016).
24. Cuperus, J. T. et al. Deep learning of the regulatory grammar of yeast 5' untranslated regions from 500,000 random sequences. *Genome Res.* **27**, 2015–2024 (2017).
25. Shaw, P. J., Ponmee, N., Karoonuthaisiri, N., Kamchonwongpaisan, S. & Yuthavong, Y. Characterization of human malaria parasite *Plasmodium falciparum* eIF4E homologue and mRNA 5' cap status. *Mol. Biochem. Parasitol.* **155**, 146–155 (2007).
26. Tuteja, R. Identification and bioinformatics characterization of translation initiation complex eIF4F components and poly(A)-binding protein from *Plasmodium falciparum*. *Commun. Integr. Biol.* **2**, 245–260 (2009).
27. Bancells, C. & Deitsch, K. W. A molecular switch in the efficiency of translation reinitiation controls expression of var2csa, a gene implicated in pregnancy-associated malaria. *Molecular Microbiology* **90**, 472–488 (2013).

28. Kumar, M., Srinivas, V. & Patankar, S. Upstream AUGs and upstream ORFs can regulate the downstream ORF in *Plasmodium falciparum*. *Malar. J.* **14**, 512 (2015).
29. Horrocks, P., Wong, E., Russell, K. & Emes, R. D. Control of gene expression in *Plasmodium falciparum* - ten years on. *Mol. Biochem. Parasitol.* **164**, 9–25 (2009).
30. Chappell, L. et al. Refining the transcriptome of the human malaria parasite *Plasmodium falciparum* using amplification-free RNA-seq. *BMC Genomics* **21**, (2020).
31. Garcia, V. E., Liu, J. & DeRisi, J. L. Low-Cost Touchscreen Driven Programmable Dual Syringe Pump for Life Science Applications.
<http://biorxiv.org/lookup/doi/10.1101/288290> (2018)
32. Lorenz, R. et al. ViennaRNA Package 2.0. *Algorithms Mol. Biol.* **6**, 26 (2011).
33. Saul, A. & Battistutta, D. Analysis of the sequences flanking the translational start sites of *Plasmodium falciparum*. *Molecular and Biochemical Parasitology* **42**, 55–62 (1990).
34. Gardner, M. J. et al. Genome sequence of the human malaria parasite *Plasmodium falciparum*. *Nature* **419**, 498–511 (2002).
35. Erath, J., Djuranovic, S. & Djuranovic, S. P. Adaptation of Translational Machinery in Malaria Parasites to Accommodate Translation of Poly-Adenosine Stretches Throughout Its Life Cycle. *Front. Microbiol.* **0**, (2019).
36. Pavlovic Djuranovic, S. et al. *Plasmodium falciparum* translational machinery condones polyadenosine repeats. *eLife* **9**, e57799 (2020).
37. Waters, A. P., Syin, C. & McCutchan, T. F. Developmental regulation of stage-specific ribosome populations in *Plasmodium*. *Nature* **342**, 438–440 (1989).
38. Li, J. et al. Regulation and trafficking of three distinct 18 S ribosomal RNAs during development of the malaria parasite. *Journal of Molecular Biology* **269**, 203–213 (1997).

39. Kaur, C., Kumar, M. & Patankar, S. Messenger RNAs with large numbers of upstream open reading frames are translated via leaky scanning and reinitiation in the asexual stages of *Plasmodium falciparum*. *Parasitology* **147**, 1100–1113 (2020).
40. Amulic, B., Salanti, A., Lavstsen, T., Nielsen, M. A. & Deitsch, K. W. An Upstream Open Reading Frame Controls Translation of var2csa, a Gene Implicated in Placental Malaria. *PLOS Pathogens* **5**, e1000256 (2009).
41. Vembar, S. S., Droll, D. & Scherf, A. Translational regulation in blood stages of the malaria parasite *Plasmodium* spp.: systems-wide studies pave the way. *Wiley Interdiscip Rev RNA* **7**, 772–792 (2016).
42. Ingolia, N. T., Ghaemmaghami, S., Newman, J. R. S. & Weissman, J. S. Genome-Wide Analysis *in Vivo* of Translation with Nucleotide Resolution Using Ribosome Profiling. *Science* **324**, 218–223 (2009).
43. Brar, G. A. & Weissman, J. S. Ribosome profiling reveals the what, when, where, and how of protein synthesis. *Nat. Rev. Mol. Cell Biol.* **16**, 651–664 (2015).
44. Hinnebusch, A. G. & Lorsch, J. R. The Mechanism of Eukaryotic Translation Initiation: New Insights and Challenges. *Cold Spring Harb. Perspect. Biol.* **4**, a011544 (2012).
45. Maag, D., Algire, M. A. & Lorsch, J. R. Communication between Eukaryotic Translation Initiation Factors 5 and 1A within the Ribosomal Pre-initiation Complex Plays a Role in Start Site Selection. *Journal of Molecular Biology* **356**, 724–737 (2006).
46. Ahyong, V. et al. Identification of *Plasmodium falciparum* specific translation inhibitors from the MMV Malaria Box using a high throughput *in vitro* translation screen. *Malaria Journal* **15**, 173 (2016).

47. Kozak, M. Initiation of translation in prokaryotes and eukaryotes. *Gene* **234**, 187–208 (1999).
48. Kozak, M. Features in the 5' non-coding sequences of rabbit α and β -globin mRNAs that affect translational efficiency. *Journal of Molecular Biology* **235**, 95–110 (1994).
49. Kozak, M. Evaluation of the fidelity of initiation of translation in reticulocyte lysates from commercial sources. *Nucleic Acids Res.* **18**, 2828 (1990).
50. Karollus, A., Avsec, Ž. & Gagneur, J. Predicting mean ribosome load for 5'UTR of any length using deep learning. *PLOS Computational Biology* **17**, e1008982 (2021).

Chapter 6

Differential Disease Susceptibilities in Experimentally Reptarenavirus-Infected Boa

Constrictors and Ball Pythons

This chapter is a reprint of:

Mark D. Stenglein, David Sanchez-Migallon Guzman, Valentina E. Garcia, Marylee L. Layton,

Laura L. Hoon-Hanks, Scott M. Boback, M. Kevin Keel, Tracy Drazenovich, Michelle G.

Hawkins, and Joseph L. DeRisi. Differential Disease Susceptibilities in Experimentally

Reptarenavirus-Infected Boa Constrictors and Ball Pythons. *Journal of Virology*, 91, 15 (2017):

h <https://doi.org/10.1128/JVI.00451-17>.

6.0 Prelude

Malaria was the focus of this thesis and Ph.D., however, while performing the research presented here, several additional projects were performed focusing on zoonotic diseases. Many human infectious diseases originate in animals and many animal infections can be useful in understanding the pathology and potential impacts of human disease. Presented in this chapter is work done by an incredible team of scientists into the pathology of inclusion body disease, a viral infection with catastrophic effects in boid snakes. This chapter presents the usefulness of looking beyond human disease.

6.1 Abstract

Inclusion body disease (IBD) is an infectious disease originally described in captive snakes. It has traditionally been diagnosed by the presence of large eosinophilic cytoplasmic inclusions and is associated with neurological, gastrointestinal, and lymphoproliferative disorders. Previously, we identified and established a culture system for a novel lineage of arenaviruses isolated from boa constrictors diagnosed with IBD. Although ample circumstantial evidence suggested that these viruses, now known as reptarenaviruses, cause IBD, there has been no formal demonstration of disease causality since their discovery. We therefore conducted a long-term challenge experiment to test the hypothesis that reptarenaviruses cause IBD. We infected boa constrictors and ball pythons by cardiac injection of purified virus. We monitored the progression of viral growth in tissues, blood, and environmental samples. Infection produced dramatically different disease outcomes in snakes of the two species. Ball pythons infected with Golden Gate virus (GoGV) and with another reptarenavirus displayed severe neurological signs within 2 months, and viral replication was detected only in central nervous system tissues. In contrast, GoGV-infected boa constrictors remained free of clinical

signs for 2 years, despite high viral loads and the accumulation of large intracellular inclusions in multiple tissues, including the brain. Inflammation was associated with infection in ball pythons but not in boa constrictors. Thus, reptarenavirus infection produces inclusions and inclusion body disease, although inclusions per se are neither necessarily associated with nor required for disease. Although the natural distribution of reptarenaviruses has yet to be described, the different outcomes of infection may reflect differences in geographical origin.

6.2 Importance

New DNA sequencing technologies have made it easier than ever to identify the sequences of microorganisms in diseased tissues, i.e., to identify organisms that appear to cause disease, but to be certain that a candidate pathogen actually causes disease, it is necessary to provide additional evidence of causality. We have done this to demonstrate that reptarenaviruses cause inclusion body disease (IBD), a serious transmissible disease of snakes. We infected boa constrictors and ball pythons with purified reptarenavirus. Ball pythons fell ill within 2 months of infection and displayed signs of neurological disease typical of IBD. In contrast, boa constrictors remained healthy over 2 years, despite high levels of virus throughout their bodies. This difference matches previous reports that pythons are more susceptible to IBD than boas and could reflect the possibility that boas are natural hosts of these viruses in the wild.

6.3 Introduction

Inclusion body disease (IBD) has been a vexing problem in captive snake collections for several decades [1]. Classic clinical signs of IBD include neurological signs, regurgitation, and secondary bacterial infections, including stomatitis and pneumonia [2]. More recently, several cases of lymphoproliferative disorders have been associated with IBD in boa constrictors [2–5]. Different clinical outcomes have been described for

boas and pythons, with pythons reportedly experiencing a shorter, more severe, and more central nervous system (CNS)-involved disease course [1, 2, 6-7]. Passage experiments demonstrated IBD to be transmissible, but the etiological agent remained elusive, until the recent identification and isolation of arenaviruses from snakes diagnosed with IBD [1, 7–10].

Two major groups of arenaviruses (family Arenaviridae) have been identified: those that infect mammals (genus *Mammarenavirus*) and those that infect snakes (genus *Reptarenavirus*) [11–13]. Arenaviruses share a number of common characteristics, including a bisegmented single-stranded RNA genome with two genes on each of the small (S) and large (L) genome segments in an ambisense orientation [11-12]. One possibly distinguishing feature of reptarenaviruses is that simultaneous infection by multiple viruses is common in captive snakes [14–16]. Whether this is true in wild snakes is unclear, and in fact, there is no published information about the natural hosts of reptarenaviruses, although IBD has been described in a number of captive snakes of a number of species worldwide, and reptarenaviruses have been identified in snakes on multiple continents [2, 6, 8–10, 14, 17–19].

There is strong indirect evidence that reptarenaviruses cause IBD. First, reptarenavirus RNA detection and viral recovery are correlated with IBD diagnosis [8–10, 14]. Second, cytoplasmic inclusions, the historical diagnostic hallmark of IBD, contain reptarenavirus nucleoprotein (NP) [10, 14, 20-21]. Third, several independent metagenomic next-generation sequencing (NGS) studies have not identified other candidate etiological agents [8–10, 14-15]. Nevertheless, apparently healthy snakes can be infected with reptarenaviruses and even harbor inclusion bodies [22]. In fact, 5 of the

first 6 apparently healthy boa constrictors that we obtained initially for this study proved to be already infected with reptarenavirus. Clearly, infection does not always or immediately produce disease. Therefore, the purpose of this study was to determine whether reptarenavirus infection can cause IBD, as a formal demonstration of disease causality and as a step toward identification of viral and host determinants of pathogenicity, and to study the outcome of reptarenavirus infection in snakes of multiple species.

We therefore experimentally infected boa constrictors (*Boa constrictor*) and ball pythons (*Python regius*) with reptarenaviruses. We monitored infected snakes and uninfected controls. We periodically collected blood samples and tissue biopsy samples to monitor virus replication and collected environmental samples to assess possible mechanisms of transmission. Infected boa constrictors remained subclinical over 2 years, despite high and disseminated viral loads and the accumulation of inclusion bodies. In contrast, infected ball pythons exhibited severe neurological signs within 2 months after infection, with viral nucleic acid and protein being detected only in the brain.

6.4 Results

To confirm the absence of preexisting virus infection in the snakes to be used for experimental infections, blood, lung, and liver biopsy samples were collected and examined histologically and tested for reptarenavirus RNA by quantitative reverse transcription-PCR (qRT-PCR) and metagenomic NGS. Five of the first six boa constrictors that we obtained initially tested positive for viral RNA (designated boas A to F). Three additional boa constrictors from a closed collection tested negative and were used for infection studies (boas G to I). We

infected snakes G and H with 4×10^5 fluorescent focus-forming units (FFU) of Golden Gate virus (GoGV), a prototypic reptarenavirus, by intracardiac injection [8]. Virus had been purified from the supernatant of infected boa constrictor JK cells [8]. The third snake (boa I) was mock infected. Following inoculation, snakes were monitored and blood samples and liver and lung biopsy samples were periodically collected. Feces, urates, and shed skin samples were also collected to assess possible routes of virus shedding (Figure 6.1).

Similar to the boa constrictors, four ball pythons were obtained and confirmed to be negative for preexisting virus infection (pythons J to M). One ball python (python L) was infected with 4×10^5 FFU of GoGV, and a second one (python M) was coinfecting with 2×10^5 FFU of GoGV and 2×10^5 FFU of a reptarenavirus isolated from a boa constrictor that had exhibited stomatitis and anorexia and had been euthanized and diagnosed postmortem with IBD (snake 37 in the study described in reference 14). Our rationale for coinfecting python M was 2-fold: to assess the pathogenic potential of genetically diverse reptarenaviruses (the S segments of the two viruses share 74% pairwise nucleotide identity) and to conduct a preliminary investigation of multiple reptarenavirus infection, which is surprisingly common in captive snakes [14-15]. Feces, urates, and shed skin samples were collected.

None of the boa constrictors developed clinical signs during the 2-year experiment. All snakes behaved normally and gained weight equivalently. The three boa constrictors were euthanized at the end of the study period, 24 months postinoculation. Complete postmortem examinations were performed, and tissues were collected from all major organs for pathological examination and virus detection.

In contrast, ball pythons exhibited severe clinical signs within 2 months of infection. At 65 days postinfection, python M developed an acute onset of neurological signs characteristic of

IBD, including lethargy, abnormal posture, and failure to recover from dorsal recumbency (Figure 6.1, inset; see also Video S1 in the supplemental material). This snake was immediately euthanized. Three days later (68 days postinfection), python L was observed to have focal dermatitis of unknown etiology on its right side. Further evaluation revealed that the snake had paralysis of the caudal 80% of its body and did not respond to hypodermic needle insertions in that area. It was unclear whether the dermatitis was related to infection. The snake was immediately euthanized. The control ball pythons did not display any clinical signs and were euthanized at day 68 as well. Complete postmortem examinations of the ball pythons were performed, but no antemortem biopsy samples were collected because of rapid disease onset.

We used qRT-PCR to measure viral RNA levels in tissues. Despite the absence of clinical signs in the boa constrictors, high-level systemic virus replication was evident. Viral RNA was detectable in blood samples throughout infection at concentrations that ranged from 10³ to 10¹⁰ genome equivalents per ml of blood (Figure 6.2 A). Viral RNA was detected in antemortem liver biopsy samples and in all tissues assayed postmortem: liver, lung, tonsil, spleen, kidney, colon, trachea, and brain (Figure 6.2 B and C). The levels of viral RNA varied but reached concentrations exceeding 100-fold the copy number of the glyceraldehyde-3-phosphate dehydrogenase (GAPDH) control mRNA. Viral RNA was also detected in feces, urates, and skin shed from boa constrictors collected throughout the 2-year infection (Figure 6.3). Attempts to isolate virus from these environmental samples were unsuccessful, perhaps because the samples may not have been processed or stored in a manner that preserved infectivity. These results show that boa constrictors support high reptarenavirus loads in the absence of clinical signs and shed detectable viral RNA in feces, urates, and skin.

In ball pythons, viral RNA was detected only in the central nervous system of both infected snakes but not in other tissues tested (blood, colon, liver, lung, and kidney; Figure 6.4A). Segments of genotypes S2 and L2 were detected in the brain of snake L (Figure 6.4B). Segments of genotypes S6 and L3 were detected by qRT-PCR in the brain of snake M, which had been coinfecting with GoGV (S2/L2) and snake 37 virus (genotype S6/L3/L21) (Figure 6.4C). We created shotgun NGS libraries from total RNA extracted from the brains of the two infected ball pythons to confirm the absence of other organisms that could be responsible for neurological signs and did not identify other candidate pathogen sequences. Viral RNA was not detected in feces, urates, or shed skin collected from the ball pythons.

We used fluorescence microscopy with an antibody raised against a peptide from GoGV NP to visualize viral protein in tissues. In tissues from infected boa constrictors at necropsy, we observed large cytoplasmic NP-positive inclusions in every tissue examined: heart, intestinal, liver, kidney, and brain (Figure 6.5 and 6.6). Viral inclusions were also apparent in the liver biopsy samples taken from both infected boas at 16 weeks and 32 weeks postinfection but were not evident in tissue samples collected preinfection (Figure 6.5).

In infected ball pythons, we did not detect NP-staining inclusions in any tissues except for brain (Figure 6.6 and 6.7). Anti-NP antibody staining was present in brain cells of ball python L, but in contrast to the inclusions found in boa constrictor tissues, including brain, the staining appeared to be diffusely cytoplasmic (compare Figure 6.6 B and C). For the brain of python M, anti-NP staining was observed, but the fixed slices from python M were not of sufficient quality for staining by DAPI (4',6-diamidino-2-phenylindole), limiting our ability to characterize infection in this specimen. Anti-NP staining was absent from all other ball python necropsy tissues, including heart, kidney, intestinal, and liver (Figure 6.7).

Gross and histopathological examinations were performed on euthanized snakes. In both infected and control boa constrictors, gross lesions were mild or considered incidental. The most notable histological change in boa constrictors was the presence of large eosinophilic inclusions in tissues throughout the body, and in some tissues the majority of cells were affected. Most (boa H) to virtually all (boa G) neurons in the brain and spinal cord had sharply demarcated inclusions (Figure 6.8). Inclusions were most dense in the retina, neurons, bile duct epithelium, ductuli efferentes, exocrine pancreas, stomach, and kidney. Inclusion bodies were common in lymphocytes of all tissues in infected boa H but not in boa G. Inclusions were also noted in peripheral ganglia, the optic nerve, seminiferous tubules, oviductal glands, adrenal glands, harderian glands, small intestine, respiratory epithelium, pulmonary smooth muscle, cardiomyocytes, hepatocytes, and multiple vessels. Inclusions were absent in the uninfected boa constrictor. Despite the abundant inclusions, little inflammation was observed, and that which was observed was not considered related to infection.

Pathological examinations of ball pythons revealed a picture markedly different from that in boas, characterized by central nervous system inflammation and a general lack of obvious inclusions. No gross lesions were detected in python M. Regionally extensive dermatitis, the cause and significance of which were unknown, was found in python L. The most significant histopathologic findings were inflammatory changes in the brain, spinal cord, and ganglia of both infected ball pythons (Figure 6.9). Infected pythons had mild to moderate lymphocytic encephalitis; lymphocytic ganglioneuritis; and lymphocytic, histiocytic, and granulocytic meningomyelitis. Neuronal necrosis and neuronophagia were also present (Figure 6.9). At the site of the dermatitis observed on infected python L, multiple variably sized foci of necrosis with heterophilic infiltrates were observed. Other histological changes included moderate

lymphocytolysis in multiple lymphoid organs and minimal lymphocytic biliary dochitis (python M). In infected ball pythons, the presence of inclusion bodies was equivocal, with possible viral inclusions being observed in neurons and rare bile ducts of infected python M (Figure 6.10). In both pythons, multiple types of epithelial cells had eosinophilic granular material within the cytoplasm. Although these granules were suggestive of inclusions, the material was generally more lightly stained and indistinct compared to typical inclusions of IBD. In control snakes (snakes J and K), no significant gross or microscopic lesions were observed.

6.5 Discussion

Reptarenaviruses were first identified in cases of IBD, and substantial but indirect evidence suggested that reptarenavirus infection causes disease [8–10, 14-15]. While infection of both boa constrictors and ball pythons resulted in the presence of detectable viral replication, we noted a stark contrast between the outcomes in the two types of snakes. During 2 years of infection, boa constrictors maintained high levels of viremia (10^3 to 10^{10} viral copies per ml of blood) and accumulated widespread intracytoplasmic inclusions. Despite the high viral load and numerous inclusion bodies, boas did not display overt clinical signs by the time that they were euthanized, and there was a notable absence of inflammation. In contrast, infection of ball pythons produced dramatic clinical signs over the course of only 60 days. In pythons, inclusions were extremely rare, virus was detected only in the CNS, and pronounced inflammation was observed. These findings are by and large concordant with those of two IBD transmission experiments in Burmese pythons and boa constrictors that were conducted prior to the identification of reptarenaviruses [1, 7]. Additional studies will be required to untangle the factors underlying this species-specific clinical outcome. It is also likely that not all snakes (even of the same species) respond identically to infection, and additional studies using larger numbers

of infected snakes could reveal variability in clinical outcomes that our study, with its relatively small numbers, missed.

It is not clear whether the infected boa constrictors would have eventually progressed to disease and, if so, over what time period. There are many examples of viruses that produce disease only after a long chronic period. For instance, HIV-1 infection typically progresses to AIDS only after years of a mainly subclinical infection. It is possible that a longer chronic phase, secondary infection, stress, or other triggers are necessary for IBD progression in boa constrictors and other less susceptible snakes. Nevertheless, reptarenavirus infection in ball pythons produced neurological signs typical of those associated with IBD, and these viruses remain the leading candidate etiological agent for IBD in all snakes.

One possible explanation for the chronic subclinical infection in boa constrictors is that they are a reservoir host for reptarenaviruses in the wild [23]. Boa constrictors (family Boidae) are native to the Americas, and ball pythons (family Pythonidae) are found in Africa. It is possible that reptarenaviruses have coevolved with and adapted to their natural reptile hosts in the Americas, as is the case for the New World lineage of mammal-infecting arenaviruses [11-12, 24]. Additional sampling of wild snakes will address this possibility.

It is possible that reptarenavirus genotype influences clinical outcome. Indeed, a large number of genetically diverse reptarenaviruses have been described, and it is possible that some reptarenaviruses would produce disease outcomes different from those observed here. For instance, a reptarenavirus not studied here might cause disease in boa constrictors but not ball pythons. It would therefore be imprudent to extrapolate from these results to all reptarenaviruses. Nevertheless, prior studies have observed a strong connection between snake species and the IBD clinical course, whereas no connection between reptarenavirus genotype and clinical

outcome has been noted to date [1-2, 7, 9, 14-15]. In addition, in our experiment, ball pythons infected with different reptarenavirus genotypes exhibited similar clinical signs: both python L infected with GoGV and python M infected with GoGV and snake 37 virus displayed severe neurological signs. We identified a subset of the inoculated genome segment genotypes in python M's brain (S6/L3), indicating that the genotype combinations S2/L2 and S6/L3 produced similar disease.

One of our motivations for coinfecting python M with GoGV and snake 37 virus was to begin to investigate the phenomenon of multiple reptarenavirus infection [14-15]. This phenomenon is surprisingly common in captive snakes and is characterized by intrahost virus populations composed of multiple distinct viral genotypes and by an imbalance between the numbers of S and L segment genotypes in a single infection. For instance, the snake 37 virus inoculum was composed of 3 genetically distinct reptarenavirus segments: S6, L3, and L21 (the GoGV genome is simply S2 and L2). This virus was isolated from an infected boa constrictor, and the 3 segments replicate as an ensemble in culture [14]. In our survey of reptarenavirus diversity, S6 was by far the most prevalent S segment genotype, both at a population level and in individual snakes, suggesting that it may be outcompeting the S segments of other genotypes (14). That S6 was the only S genotype detected in the brain of coinfecting ball python M supports this suggestion, but larger studies will be necessary for a more conclusive investigation of this intriguing phenomenon.

Despite the name IBD, the connection between inclusions and disease is clearly not straightforward. It is now well established that reptarenavirus infection produces the inclusions associated with IBD [8, 10, 22]. However, inclusions do not necessarily indicate disease and disease does not require inclusions. Inclusions can be found in apparently healthy snakes, and in

infected ball pythons, viral nucleoprotein was cytoplasmic but was not found in inclusion bodies. We speculate that inclusion bodies may accumulate slowly, and given the rapid disease onset in ball pythons, inclusions may not have had enough time to form. Indeed, the granular appearance of cytoplasmic anti-NP staining in python tissues is reminiscent of the staining pattern observed in boa JK cells shortly after infection [8]. Thus, reptarenavirus infection produces inclusions and inclusion body disease, but inclusions per se are not pathognomonic for IBD, despite assertions to that effect [16]. This study has implications for the control of IBD in captive snake populations.

Our data suggest that large quantities of virus may be shed in feces, urates, and skin. Thus, infected boas could be actively transmitting virus during a chronic and subclinical period, confounding disease control and quarantine measures. It would be prudent to separate boa constrictors and pythons until the boa constrictors have been confirmed by molecular methods to be free of reptarenaviruses, which have now been unambiguously linked to disease in ball pythons.

6.6 Materials and Methods

6.6.1 Ethics statement

This study, including protocols for the care, handling, and infection of animals, was approved by the University of California, Davis, Institutional Animal Care and Use Committee (IACUC protocol 17450).

6.6.2 Preparation of virus stocks

Virus stocks for inoculation were prepared by infecting boa constrictor JK cells with low-passage-number stocks of Golden Gate virus (GoGV) [8] or snake 37 virus, the virus population isolated from snake 37 [14]. Ten-centimeter-diameter dishes of infected JK cells were cultured as

described previously [8]. Supernatant was collected at 4, 7, 10, and 13 days post infection and stored at -80°C. Viral RNA was purified from the supernatant using a Zymo Research viral RNA kit and screened for viral RNA levels by qRT-PCR as described below. Supernatants with the highest viral RNA levels were pooled and clarified by centrifugation at 930 g for 5 min at room temperature. Clarified supernatants were filtered through a 0.22-µm-pore-size filter and underlaid with a 30% sucrose cushion in a centrifuge bottle (catalog number 355618; Beckman Coulter). Viruses were concentrated by ultracentrifugation at 140,000 g in a Thermo Fisher Scientific F50L-8x39 rotor for 2 hours at 4°C. The supernatant was decanted, and the pellet was resuspended in 1 to 2 ml phosphate-buffered saline (PBS). Aliquots were stored at -80°C and titrated using a fluorescent focus assay as described previously [25].

6.6.3 Snake husbandry and monitoring

Three adult boa constrictors (*Boa constrictor*; one male control, one male infected, one female infected) and four adult ball pythons (*Python regius*; two female controls, one female infected, one male infected) were used for this study. Control and infected snakes were housed in separate buildings and were handled independently, and each animal had its own tank and supplies. Following procurement, the snakes were allowed to acclimate to their housing for 3 weeks prior to the start of the study. Whole blood was collected for overall health assessment and for arenavirus RNA by qRT-PCR prior to inclusion in the study. During the acclimation and study periods, the snakes were monitored twice daily for overall health. Animals that exhibited any abnormal neurological signs (star gazing, head tilt, tongue flicking), gastrointestinal signs (regurgitation, diarrhea, constipation), or respiratory clinical signs, that repeatedly declined food, or that exhibited steady body weight loss were to be euthanized.

6.6.4 Liver and lung biopsy samples

After the acclimation period, liver and lung biopsy samples were collected while the snakes were under isoflurane anesthesia. The snakes were again anesthetized, and surgical lung and liver biopsy samples were collected at 4 and 8 months postinoculation. Biopsy samples were examined histopathologically and for reptarenavirus RNA by qRT-PCR and metagenomic NGS. Snake inoculation and blood sample collection. Several weeks after the initial biopsy samples were collected, mock or experimental infections were administered by intracardiac injection of the viral inoculum in 200 l PBS while the snakes were under general anesthesia (the anesthetic protocol was identical to that described above for collection of biopsy samples). We chose this route of infection because the natural routes of reptarenavirus transmission in the wild remain unknown and because prior studies have shown that reptarenaviruses replicate in blood cells [20]. Thereafter, every 14 days for the 1st 3 months, 0.3- to 0.5-ml whole-blood samples were collected via cardiocentesis with manual restraint, using a 25-gauge needle on a 1- or 3-ml syringe. A minimum of 3 blood smears were made, and the remaining blood was collected in lithium-heparin tubes and stored at -80°C until testing. At 2 months, 3 months, and 18 months, an additional 0.25-ml whole-blood sample was collected into a K2 EDTA tube for a complete blood count (and biochemistry panel at 18 months). After 3 months, blood was collected monthly for 9 months and then every 3 months during the second year of the study.

6.6.5 Euthanasia and postmortem examination

The snakes were euthanized using 100 mg/kg of body weight pentobarbital, administered by the intracardiac route, while the snakes were under isoflurane anesthesia either after the exhibition of clinical signs or at the end of the study. A full postmortem examination was performed.

Sections of brain, spinal cord, trachea, lung, liver, kidney, spleen, pancreas, adrenal glands, gonads, heart, tonsil, and complete gastrointestinal tract were collected and placed in 10% buffered formalin, fixed, processed as 5- μ m sections, and stained with hematoxylin and eosin (H&E). A second identical set of tissues was immediately flash frozen in liquid nitrogen and stored at -80°C.

6.6.6 Immunofluorescence staining and imaging

Paraffin-mounted slides were deparaffinized with the following series of 3-min washes: mixed xylenes (2 times), 50% mixed xylenes to 50% ethanol, 100% ethanol (2 times), 95% ethanol, 70% ethanol, 50% ethanol, and deionized water (2 times). Antigen retrieval by a 30-min incubation at 99°C in EDTA buffer (1 mM EDTA with 0.05% Tween 20) followed. The slides were then rinsed three times with deionized water and washed in 50 mM Tris, pH 7.6, 150 mM NaCl (Tris-buffered saline [TBS]) containing 0.025% Tween 20 for 5 min (2 times). Permeabilization was done in PBS with 0.1% Triton X-100 for 5 min, followed by 5-min washes in TBS with 0.05% Tween 20 (TBS-T) (4 times). After the slides were washed, they were blocked in blocking buffer (5% donkey serum, 1% bovine serum albumin [BSA] in TBS) for 20 min and incubated overnight at 4°C in antinucleoprotein primary antibody [8] at a 1:1,000 dilution in TBS with 1% BSA, followed by washing in TBS-T for 5 min (4 times). Donkey anti-rabbit immunoglobulin conjugated with Alexa Fluor 488 (catalog number A-21206; Thermo Fisher Scientific) secondary antibody was then applied at a 1:400 solution in TBS with 1% BSA for 30 min at room temperature in the dark. Finally, the slides were washed in TBS-T (4 times) and mounted using Prolong antifade mounting reagent with DAPI (catalog number P36931; Thermo Fisher Scientific). Imaging was performed on a Zeiss Axio Scan microscope using a 20 lens or on a Nikon Ti microscope with a Andor Zyla 4.2 scientific grade complementary metal-

oxide semiconductor (sCMOS) spinning-disk camera with a 100 lens. Image processing was done using the Zeiss software Zen Microscopy and ImageJ software [26].

6.6.7 RNA extraction

RNA was extracted from solid tissue samples, feces, urates, and shed skin samples as previously described [14]. Purified and DNase-treated RNA samples were resuspended in 50 μ l of RNase- and DNase-free water and quantified fluorometrically. To extract RNA from blood, 250 μ l of whole blood was added to a 2-ml tube containing 1 ball bearing and 1 ml of TRIzol reagent (Invitrogen) and homogenized using a TissueLyser tissue disrupter (Qiagen) for 2 to 3 min at 30 Hz. Homogenized samples were mixed with 200 μ l of chloroform, and the mixture was incubated at room temperature for 2 min and centrifuged for 10 min at 12,000 g at 4°C. The aqueous phase was mixed with 450 μ l cold isopropanol, and the mixture was incubated at 4°C for 1 h. Samples were centrifuged for 10 min at 12,000 g at 4°C, and the supernatant was decanted. Precipitated RNA was washed with 1 ml of 75% ethanol and incubated for 10 min at 4°C. RNA was pelleted by centrifugation for 10 min at 12,000 g at 4°C. Ethanol was removed and the pellet was allowed to air dry before it was resuspended in 80 μ l of RNase- and DNase-free water. Samples were treated with 20 units of DNase I (NEB) and incubated at 37°C for 30 min. To the DNase-treated samples, 100 μ l of a phenol-chloroform-isoamyl alcohol mixture (125:24:1, pH 4.3) was added, and the mixture was incubated at room temperature for 15 min and then centrifuged for 3 min at 12,000 g at 4°C. The aqueous phase was transferred to a new 1.5-ml tube, and RNA was precipitated using a GlycoBlue coprecipitant protocol (Ambion) with a prolonged incubation step of 30 min. Samples were DNase treated twice, followed by phenol chloroform extraction and coprecipitation with GlycoBlue coprecipitant.

6.6.7 Illumina sequencing and data analysis

Sequencing libraries were prepared from RNA and analyzed as previously described [14]. qRT-PCR. RNA (500 ng) was added to 1 l of 250 M random hexamer oligonucleotide, and the mixture was incubated at 65°C for 5 min. Master mix was added to final concentrations of 1 reaction buffer, 5 mM dithiothreitol, 1.25 mM (each) deoxynucleoside triphosphates (dNTPs), and 0.5 l of SuperScript III reverse transcriptase (Life Technologies). The reaction mixtures were incubated for 5 min at 25°C, then for 30 to 60 min at 42°C, and then for 15 min at 70°C. cDNA was diluted to 100 l (1:10) in water. Each quantitative PCR (qPCR) mixture contained 5 l diluted cDNA, 1 Hot FirePol mix Plus (Solis Biodyne), and 0.5 M each primer. qPCRs were run on a Roche LightCycler 480 instrument with thermocycling conditions of 15 min at 95°C and 40 cycles of 10 s at 95°C, 12 s at 60°C, and 12 s at 72°C. Viral RNA levels were calculated using linearized plasmid standard curves. The primers (primer sequences) used for qPCR were MDS-558 (TTGATCTTCAGTCAGGACTTTACG) and MDS-559 (RACCTTGGTTCCACTGCTG) for S6; MDS-530 (ATGAGTGAGYCGACCTCCATAG) and MDS-531 (CRAGTGCCAATGATGTAAGAGAA) for L3; MDS-538 (CCTCCATTGGCCTAACAACT) and MDS-539 (CAAGAGCAAGAGAGGTCAGAGAG) for L21; MDS-554 (CGGTGAATCCTAGTGAGGAG) and MDS-555 (CTACCTTGGACCCACTGGAA) for S2; MDS532 (CGRCTCCACCGCCATT) and MDS-533 (GAGTGCTAGTGARGAAAGAGATCC) for L2; MDS-785 (TGTCACAATGATGACCCTCAA) and MDS-786 (GGGCCAGTGATGAGAGAGAC) for L13; and MDS-921 (AATATCTGCCCCATCAGCTG) and MDS-923 (GTTTTCCAAGAGCGTGATCC) for GAPDH. In some instances, Sanger sequencing was used to verify the qRT-PCR products.

6.6.8 Accession number(s)

Sequencing data have been deposited in the Sequence Read Archive under BioProject accession number PRJNA383000.

6.7 Supplemental Materials

Supplemental material for this article may be found at <https://doi.org/10.1128/JVI.00451-17>.

6.7 Acknowledgements

This study was funded by support from the Howard Hughes Medical Institute; the Solomon Reptile Research Fund; the School of Veterinary Medicine, University of California, Davis; and Colorado State University. V.E.G. was supported by NIH T32 training grant 2T32GM007810-37. The funders had no role in study design, data collection and interpretation, or the decision to submit the work for publication. We thank Drury Reavill, Joseph Allison, Jessica Lund, Eric Chow, and the Center for Advanced Technology at the University of California, San Francisco, for assistance with next-generation sequencing.

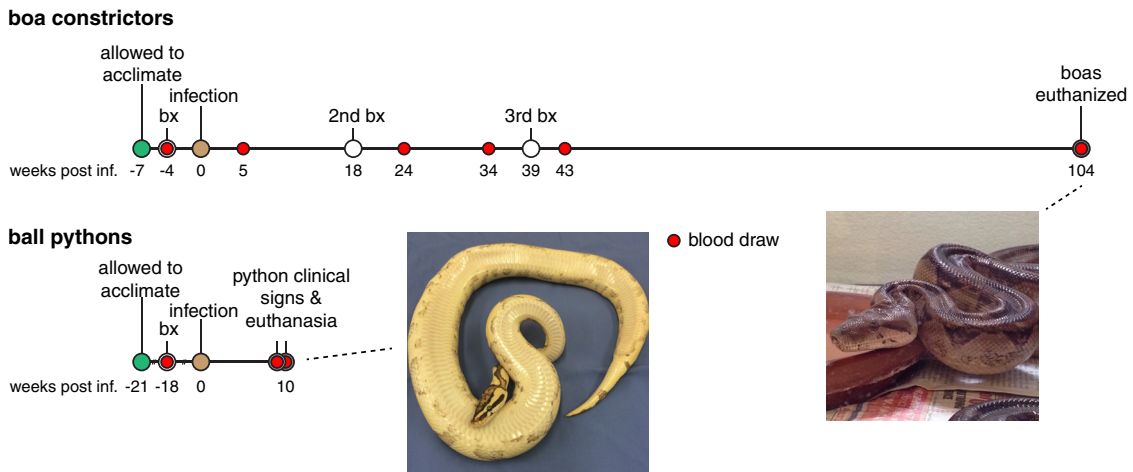


Figure 6.1 Timeline of experimental reptarenavirus infection of boa constrictors and ball pythons

The times of collection of the pre- and post-infection biopsy samples (bx) and blood samples tested are indicated. weeks post inf., weeks post-infection. (Insets) Images of a representative infected boa constrictor and representative infected ball python at the end of their respective study periods.

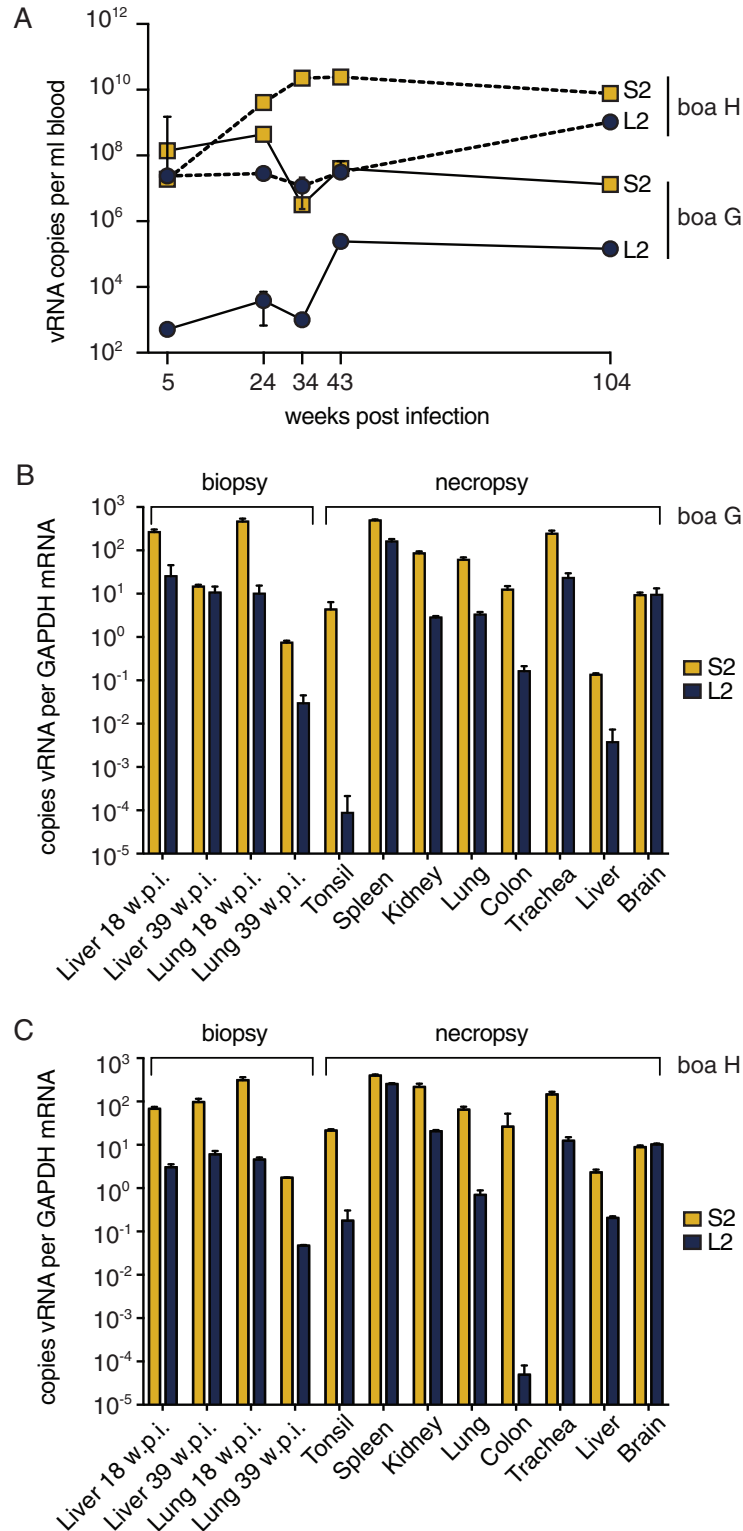


Figure 6.2 Viral RNA load in reptarenavirus infected boa constrictor tissues by qRT-PCR
 Boa constrictors had persistently high viral loads in all tissues. Viral RNA (vRNA) levels were quantified by qRT-PCR. (A) Blood viral RNA levels. (B and C) Tissue viral RNA levels for snake G (B) and snake H (C). Samples from the uninfected boa constrictor were negative. w.p.i., weeks postinfection; S2 and L2, viral genome segment genotypes.

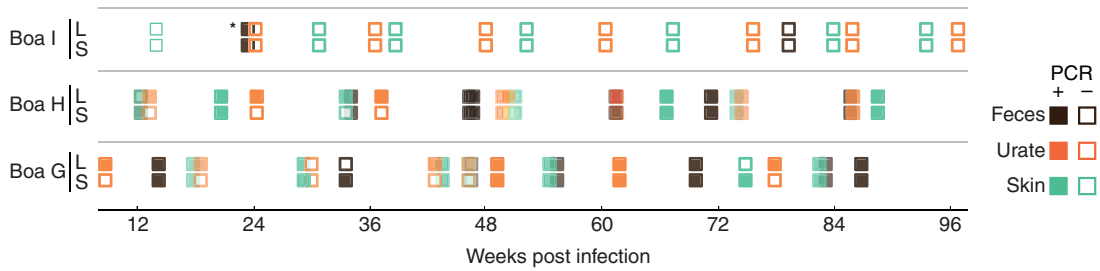


Figure 6.3 Viral load by qRT-PCR in the feces, urates, and shed skin of infected boa constrictors Viral RNA is detectable in feces, urates, and shed skin from infected boa constrictors. Viral RNA was detected by qRT-PCR. Viral RNA was not detected in any fecal, urate, or skin sample collected from ball pythons. *, the positive result for this fecal sample from the control snake may have resulted from sample mislabeling; no other sample from this control animal ever tested positive.

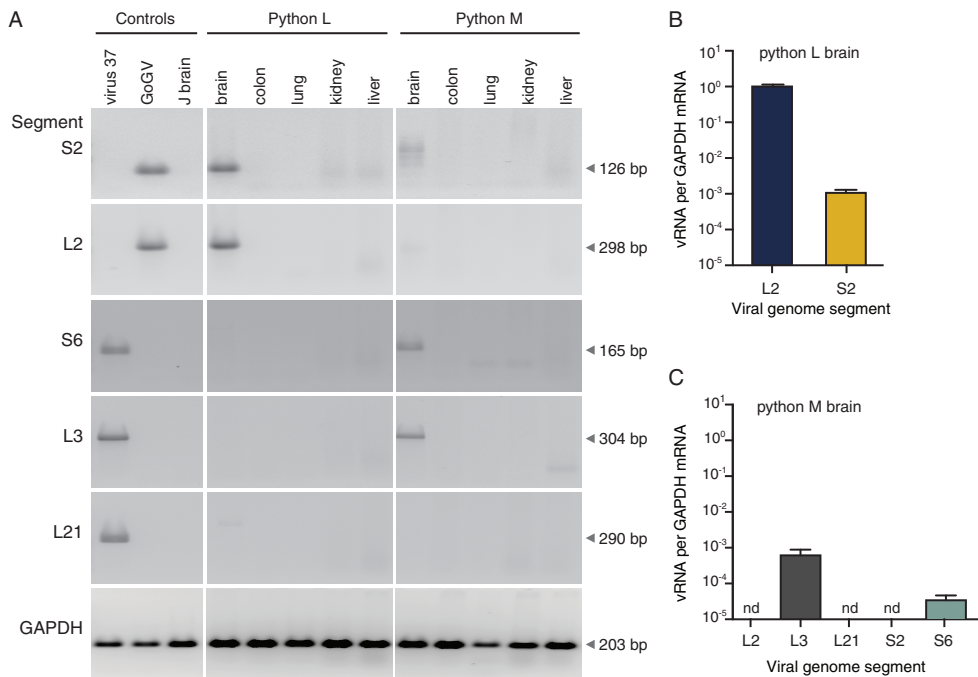


Figure 6.4 Viral RNA load in ball python tissues by qRT-PCR Viral RNA was detectable in infected ball python brains. Viral and cellular RNA levels were quantified by qRT-PCR. (A) Reptarenavirus RNA was detected in brain but not other tissues. (B and C) Viral RNA levels were normalized to the levels of GAPDH mRNA in ball python L (B) and M (C) brains. Samples from uninfected snakes were negative. Controls were the virus 37 inoculum (virus 37), the GoGV inoculum (GoGV), and uninfected python J brain (J brain). nd, not detected.

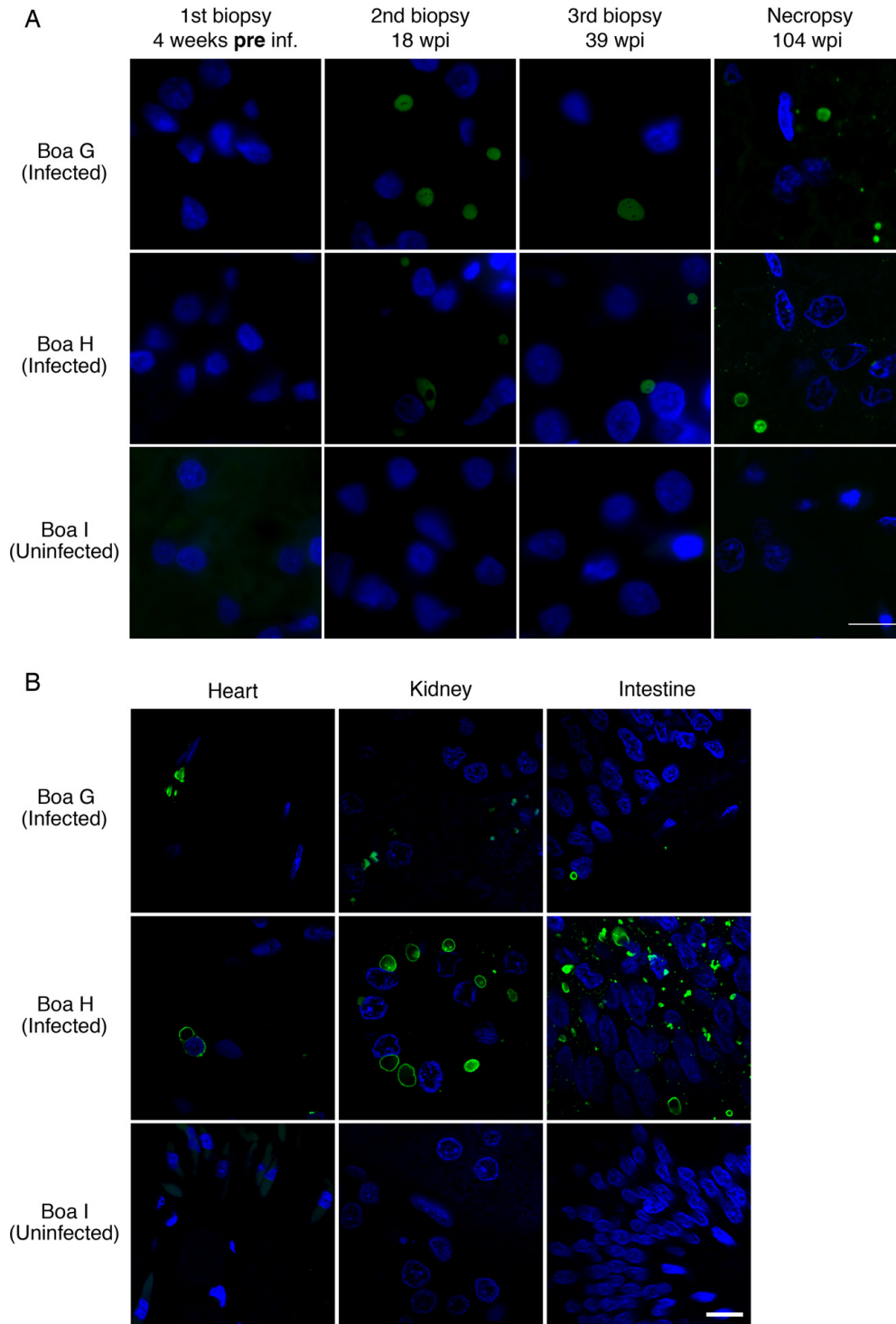


Figure 6.5 Viral inclusions in boa constrictor tissues identified with anti-NP antibody
 Reptarenavirus nucleoprotein-positive inclusions were detected in tissues of infected boa constrictors throughout infection. (A) Biopsy and necropsy liver sections from infected and uninfected boa constrictors were stained with anti-NP antibody (green) and DAPI (blue). (B) Necropsy heart, kidney, and intestine sections were stained as described in the legend to panel A. Bars = 10 μ m.

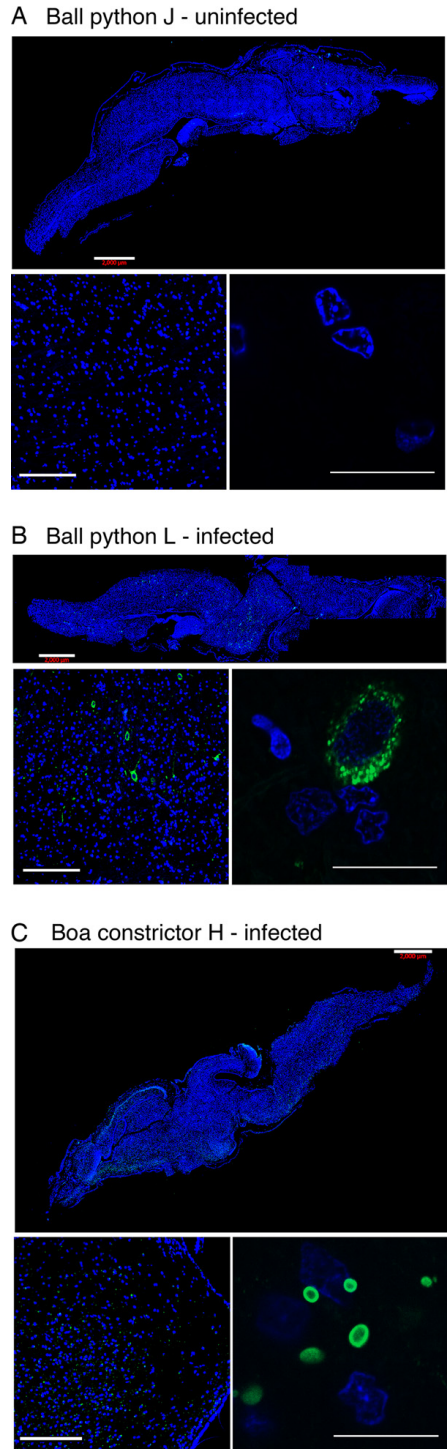


Figure 6.6 Viral nucleoprotein in ball python brain tissue identified with anti-NP antibody
 Reptarenavirus nucleoprotein detected in the brains of infected snakes. Brain sections were stained with anti-NP antibody (green) and with DAPI (blue). Sections were obtained from uninfected ball pythons J (A), infected ball python L (B), and infected boa constrictor H (C). The top, lower left, and lower right panels display increasingly zoomed images of the same sections, in which the bars are 2,000, 200, and 20 μm , respectively. Contrast speckled cytoplasmic staining in infected ball python cells (B) with inclusions in infected boa constrictor cells (C).

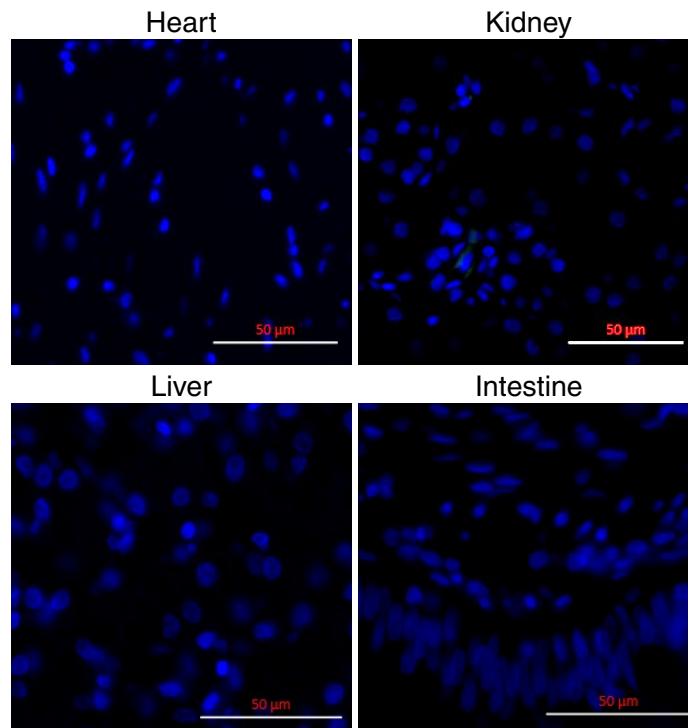


Figure 6.7 Absence of viral nucleoprotein in non-brain ball python tissues

Reptarenavirus nucleoprotein was not detected in non-CNS tissues of infected ball pythons. Necropsy tissues from infected ball python L were stained with anti-NP antibody (green) and DAPI (blue). These images are representative of negative staining of all non-CNS tissues from all ball pythons. Bars = 50 μ m.

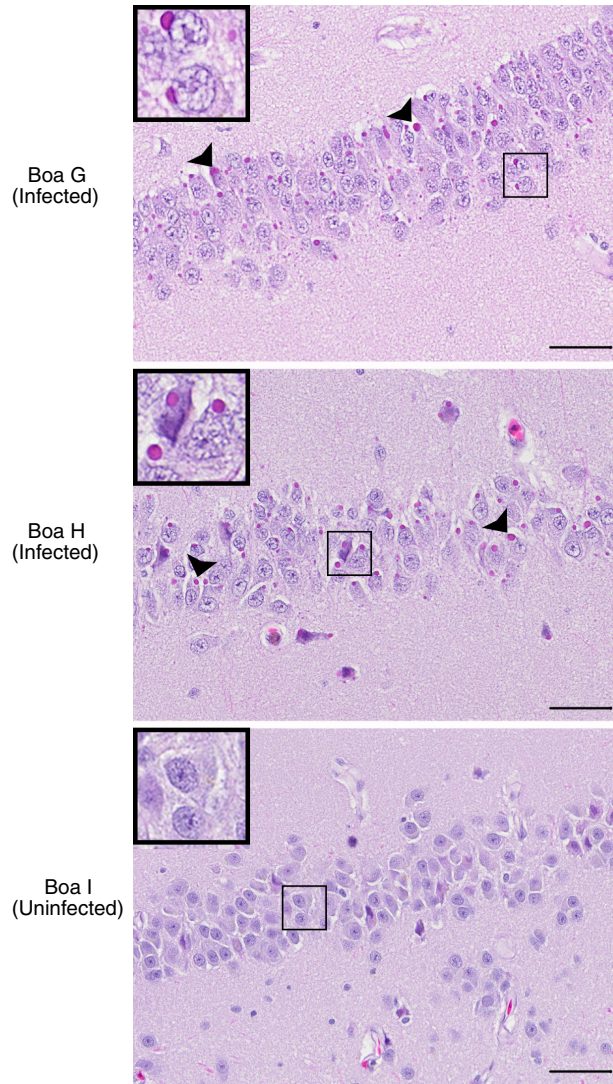


Figure 6.8 Protein inclusions in boa constrictors visualized with H&E staining

Inclusions were evident in infected boa constrictor brains. Images of hematoxylin and eosin (H&E)-stained brain sections from the indicated boa constrictors are shown. Infected boa constrictors (boas G and H) had numerous, brightly eosinophilic, cytoplasmic viral inclusion bodies (arrowheads) within neuronal cell bodies and glial cells of the brain. Similar inclusions were found within cells of nearly every organ examined. No inflammation was associated with the inclusions. The uninfected boa constrictor (boa I) did not have inclusions. (Insets) Magnified views of the boxed regions. Bars = 50 µm.

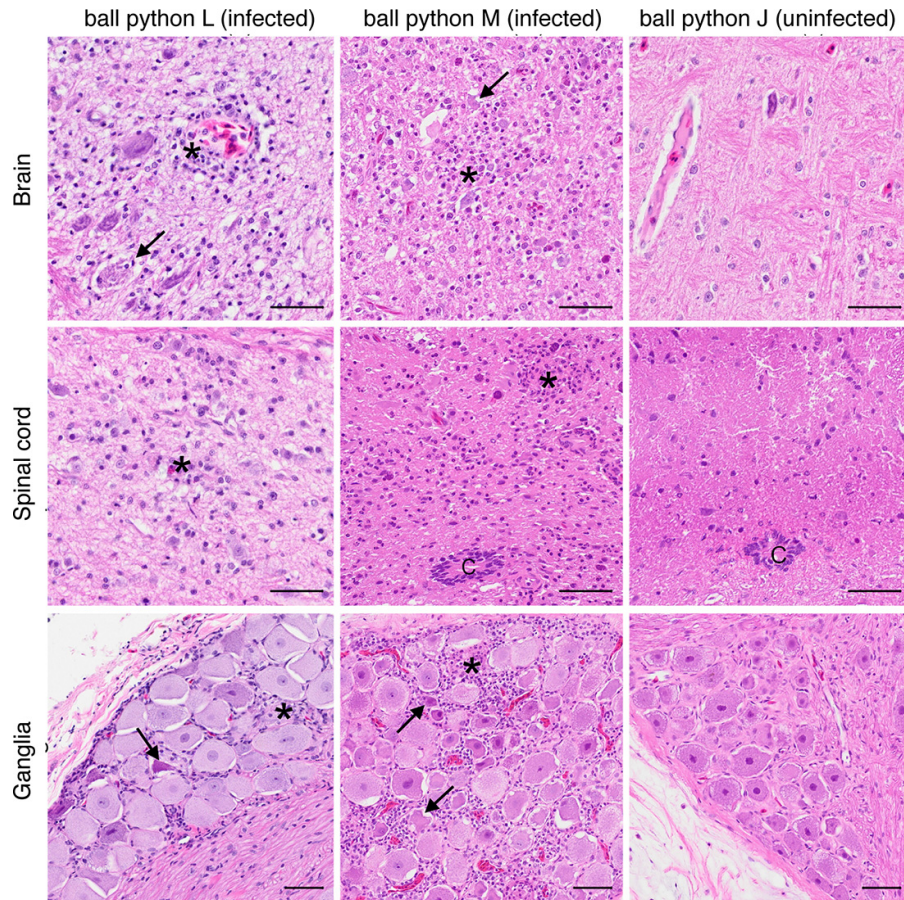


Figure 6.9 Inflammation identified in ball python central nervous system by H&E staining
 Inflammation in infected ball python central nervous system tissues. Arenavirus-infected pythons (pythons L and M) had moderate lymphocytic, histiocytic, and granulocytic inflammation (asterisks) within the brain, spinal cord, and ganglia. Necrotic neurons were occasionally seen (arrows). No inflammation was detected in the uninfected pythons. C, central canal. H&E-stained tissue section. Bars = 50 μ m.

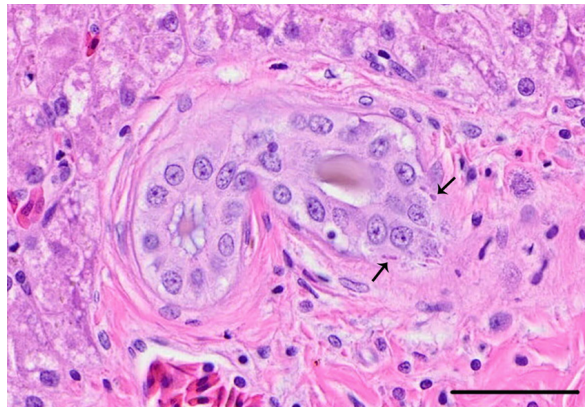


Figure 6.10 Small eosinophilic cytoplasmic inclusions in ball python bile duct

Bile duct inclusions in ball python M. Small eosinophilic cytoplasmic inclusions (arrows) were seen in rare bile duct epithelial cells of the infected ball python M. H&E-stained tissue section. Bar = 50 μ m.

Chapter 6 References

1. Schumacher J, Jacobson E, Homer B, Gaskin J. Inclusion body disease in boid snakes. *J Zoo Wildl. Med.* **25**, 511–524 (1994).
2. Chang L-W, Jacobson ER. Inclusion body disease, a worldwide infectious disease of boid snakes: a review. *J. Exot. Pet Med.* **19**, 216 –225 (2010).
3. Schilliger L, Selleri P, Frye FL. Lymphoblastic lymphoma and leukemic blood profile in a red-tail boa (*Boa constrictor constrictor*) with concurrent inclusion body disease. *J. Vet. Diagn. Invest.* **23**, 159 –162 (2011).
4. Summa NM, Sanchez-Migallon Guzman D, Hawkins M, Grosset C, Chen V, Goldsmith D, Keel K, Woolard K, Young A, Bucy D, Steffey M. Tracheal and colonic resection and anastomosis in a boa constrictor (*Boa constrictor*) with T-cell lymphoma. *J. Herpetol. Med. Surg.* **25**, 87–99 (2015).
5. Schilliger L, Rossfelder A, Bonwitt J, Di Girolamo N, Rival F, Gandar F, Selleri P, Nicolier A. Antemortem diagnosis of multicentric lymphoblastic lymphoma, lymphoid leukemia, and inclusion body disease in a boa constrictor (*Boa constrictor imperator*). *J. Herpetol. Med. Surg.* **24**, 11–19 (2014).
6. Jacobson ER. Infectious diseases and pathology of reptiles: color atlas and text. CRC/Taylor & Francis, Boca Raton, FL (2007).
7. Wozniak E, McBride J, DeNardo D, Tarara R, Wong V, Osburn B. Isolation and characterization of an antigenically distinct 68-kd protein from nonviral intracytoplasmic inclusions in *Boa constrictors* chronically infected with the inclusion body disease virus (IBDV: Retroviridae). *Vet. Pathol.* **37**, 449 – 459 (2000).

8. Stenglein MD, Sanders C, Kistler AL, Ruby JG, Franco JY, Reavill DR, Dunker F, Derisi JL. Identification, characterization, and *in vitro* culture of highly divergent arenaviruses from boa constrictors and annulated tree boas: candidate etiological agents for snake inclusion body disease. *mBio*, **3**, e00180-12 (2012).
9. Bodewes R, Kik MJL, Raj VS, Schapendonk CME, Haagmans BL, Smits SL, Osterhaus ADME. Detection of novel divergent arenaviruses in boid snakes with inclusion body disease in The Netherlands. *J. Gen. Virol.* **94**, 1206–1210 (2013).
10. Hetzel U, Sironen T, Laurinmäki P, Liljeroos L, Patjas A, Henttonen H, Vaheri A, Artelt A, Kipar A, Butcher SJ, Vapalahti O, Hepojoki J. Isolation, identification, and characterization of novel arenaviruses, the etiological agents of boid inclusion body disease. *J. Virol.* **87**: 10918–10935 (2013).
11. Radoshitzky SR, Bào Y, Buchmeier MJ, Charrel RN, Clawson AN, Clegg CS, DeRisi JL, Emonet S, Gonzalez J-P, Kuhn JH, Lukashevich IS, Peters CJ, Romanowski V, Salvato MS, Stenglein MD, de la Torre JC. Past, present, and future of arenavirus taxonomy. *Arch. Virol.* **160**, 1851–1874 (2015).
12. Buchmeier MJ, de la Torre JC, Peters CJ. Arenaviridae, p 1283–1303. In Knipe DM, Howley PM, Cohen JI, Griffin DE, Lamb RA, Martin MA, Racaniello VR, Roizman B (ed), *Fields virology*, 6th ed. *Lippincott Williams & Wilkins*, Philadelphia, PA (2013).
13. Salvato MS, Clegg JCS, Buchmeier MJ, Charrel RN, Gonzalez JP, Lukashevich IS, Peters CJ, Romanowski V. Arenaviridae, p 715–723. *In Virus taxonomy. Classification and nomenclature of viruses. Ninth report of the International Committee on Taxonomy of Viruses.* *Elsevier Academic Press*, San Diego, CA.

14. Stenglein MD, Jacobson ER, Chang L-W, Sanders C, Hawkins MG, Guzman DS-M, Drazenovich T, Dunker F, Kamaka EK, Fisher D, Reavill DR, Meola LF, Levens G, DeRisi JL. Widespread recombination, reassortment, and transmission of unbalanced compound viral genotypes in natural arenavirus infections. *PLoS Pathog.* **11**, e1004900 (2015).
15. Hepojoki J, Salmenperä P, Sironen T, Hetzel U, Korzyukov Y, Kipar A, Vapalahti O. Arenavirus coinfections are common in snakes with boid inclusion body disease. *J. Virol.* **89**, 8657– 8660 (2015).
16. Keller S, Hetzel U, Sironen T, Korzyukov Y, Vapalahti O, Kipar A, Hepojoki J. Co-infecting reptarenaviruses can be vertically transmitted in boa constrictor. *PLoS Pathog.* **13**, e1006179 (2017).
17. Aqrabi T, Stöhr AC, Knauf-Witzens T, Krenzel A, Heckers KO, Marschang RE. Identification of snake arenaviruses in live boas and pythons in a zoo in Germany. *Tierarztl Prax Ausg K Klientiere Heimtiere* **43**, 239 –247 (2015).
18. Hellebuyck T, Pasmans F, Ducatelle R, Saey V, Martel A. Detection of arenavirus in a peripheral odontogenic fibromyxoma in a red tail boa (*Boa constrictor constrictor*) with inclusion body disease. *J. Vet Diagn. Invest.* **27**, 245–248 (2015).
19. Abba Y, Hassim H, Hamzah H, Ibrahim OE, Ilyasu Y, Bande F, Mohd Lila MA, Noordin MM. *In vitro* isolation and molecular identification of reptarenavirus in Malaysia. *Virus Genes* **52**, 640 – 650 (2016).
20. Chang L-W, Fu A, Wozniak E, Chow M, Duke DG, Green L, Kelley K, Hernandez JA, Jacobson ER. Immunohistochemical detection of a unique protein within cells of snakes

- having inclusion body disease, a world-wide disease seen in members of the families Boidae and Pythonidae. *PLoS One* **8**, e82916 (2013).
21. Hepojoki J, Kipar A, Korzyukov Y, Bell-Sakyl L, Vapalahti O, Hetzel U. Replication of boid inclusion body disease-associated arenaviruses is temperature sensitive in both boid and mammalian cells. *J. Virol.* **89**, 1119–1128 (2015).
 22. Chang L, Fu D, Stenglein MD, Hernandez JA, DeRisi JL, Jacobson ER. Detection and prevalence of boid inclusion body disease in collections of boas and pythons using immunological assays. *Vet J.* **218**, 13–18 (2016).
 23. Mandl JN, Ahmed R, Barreiro LB, Daszak P, Epstein JH, Virgin HW, Feinberg MB. Reservoir host immune responses to emerging zoonotic viruses. *Cell* **160**, 20–35 (2015).
 24. Charrel RN, de Lamballerie X, Emonet S. Phylogeny of the genus Arenavirus. *Curr Opin Microbiol.* **11**, 362–368 (2008).
 25. Koellhoffer JF, Dai Z, Malashkevich VN, Stenglein MD, Liu Y, Toro R, Harrison SJ, Chandran K, DeRisi JL, Almo SC, Lai JR. Structural characterization of the glycoprotein GP2 core domain from the CAS virus, a novel arenavirus-like species. *J. Mol. Biol.* **426**, 1452–1468 (2014).
 26. Schneider CA, Rasband WS, Eliceiri KW. NIH Image to ImageJ: 25 years of image analysis. *Nat. Methods* **9**, 671–675 (2012).

Publishing Agreement

It is the policy of the University to encourage open access and broad distribution of all theses, dissertations, and manuscripts. The Graduate Division will facilitate the distribution of UCSF theses, dissertations, and manuscripts to the UCSF Library for open access and distribution. UCSF will make such theses, dissertations, and manuscripts accessible to the public and will take reasonable steps to preserve these works in perpetuity.

I hereby grant the non-exclusive, perpetual right to The Regents of the University of California to reproduce, publicly display, distribute, preserve, and publish copies of my thesis, dissertation, or manuscript in any form or media, now existing or later derived, including access online for teaching, research, and public service purposes.

DocuSigned by:

Valentina Garcia

77B650B567AF444...

Author Signature

10/20/2021

Date